Sources de particules avec des lasers de haute intensité: un outil pour les diagnostics plasma et une source innovante pour les applications.

Sven Fritzler

Contents

List of Figures

List of Tables

Chapter 1

Introduction

1.1 Scientific Context of Particle Production with High Intensity Lasers

Elementary particles like electrons, protons and neutrons are since their discovery of great interest and relevance in various domains and as their intrinsic parameters are well understood, their implementation is even today of great actuality. Here, e.g., an energetic proton beam bombarding matter resulted in the discovery of the top quark, a constituent of hadrons [1], whereas the collision of two energetic electron and positron beams proved experimentally the existence of the gluon, which describes in quantum chromodynamics the transmission of the strong force between two quarks [2]. Scattering of neutrons by an ordered magnetic structure commonly reveals information on the creation of magnons, hence, visualizes quantized spin waves [3]. Even though these experiments can be tremendously copious, they are all based on electron, proton and neutron sources.

Implementing such particle sources their basic parameters like luminosity, bunch length, source size, as well as quality in terms of angular divergence and emittance are of great importance. A higher luminosity, i.e., particle flux per unit area and time can obviously be preferential for the number of experimental events. Shorter particle bunches permit to investigate studies with higher temporal resolution, and in case they are used for radiography, a small, point-like source could be desirable to enhance the resolution.

Today, the most efficient electron sources are guns of photo-injectors, where lasers with energies of some tens of μJ and pulse durations of some ps irradiate cathodes. This liberates electrons, which are subsequently preaccelerated in radio frequency cavities operating with electric fields of around 50 MV/m. So far, this can yield bunch charges of 10 nC with durations of typically 5 ps. Implementing additional magnetic chicanes can shorten these electron bunches to about 1 ps [4]. Interestingly, the laser focal waist on these cathodes is typically of the order of 100 μm, thus, the electron source size can be approximated to be of the same order of magnitude. It is clear that these benefits are due to the small focal spot as well as short pulse length of the lasers used for these conventional accelerators.

However, these lasers are not intended to accelerate electrons to high energies even though it is known that laser electric fields can be well beyond those of radio frequency cavities. With the advent of the Chirped Pulse Amplification (CPA) [5], high power, sub-ps laser pulses became available. Focusing such lasers down to focal waists of some μm and intensities beyond 10^{18} W/cm^2, intrinsic electric fields of the order of TV/m can be obtained. These laser electric fields, though, are transverse oscillating fields which are not suitable for acceleration of free particles. Nevertheless, at such high intensities these lasers can create quasi-instantaneously plasmas on targets they are focused onto, i.e., they generate a medium consistent of free ions as well as electrons. Inside this plasma, the transverse electric laser fields can be turned into longitudinal plasma electron oscillations, known as plasma waves, which are indeed suitable for electron acceleration. Additionally, due to the high laser intensity, strong quasi-static electric fields can be induced, which can accelerate ions [6].

These principles were recently shown in numerous "proof of principle" experiments. Here, the interaction of high-intensity lasers with a plasma resulted in the generation of energetic electron [7] and ion [8] beams, which was found to be due to the induced electric [9] and magnetic fields [10] during this interaction, which can be beyond some TV/m and several hundred MG, respectively. Hence, in contrast to photo-injectors, high-intensity lasers combine the generation and acceleration of particles.

Importantly, this approach has several unique factors : (*i*) The particle bunches originate from small laser focal volumes; (*ii*) they are evoked by sub-ps laser pulses which suggest short particle bunch lengths of the same order of magnitude; (*iii*) due to the induced high electric field gradients the acceleration distance to high energies can be significantly cut down.

So far, much of these experimentation has involved large-scale, "single-shot" lasers. However, due to their inherently large costs and low repetition rates it is unlikely that such laser systems will favor applications of these unique particle sources. Thus, the extension of these studies to smaller, but higher repetition rate lasers, maintaining the same focused intensities is required. This will elucidate whether or not this approach to simultaneously generate and accelerate particles is indeed valuable for applications.

However, not only the pure characterization of these particle sources is of interest. As the schematic indicates

Laser	+	**Plasma**	→	**Interaction**	→	**Particles**
Energy, Pulse Length Focal Waist		Density, Scaling Length				Yield, Energy, Angular Divergence
Known			↔	*Unknown*	↔	*Measured*

the initial laser and plasma parameters are known and as the resulting particles can be precisely measured the determination of laser produced particle sources permits to draw conclusions on the interaction itself. Hence, it can be seen as a diagnostic for laser plasma interactions.

In this context particularly neutron generation by the fusion of low energy ions can reveal ion dynamics, yields and heating processes in plasmas. Hence, with this method it is possible to experimentally characterize even those ions, which are not sufficiently energetic to escape the plasma.

1.2 Objectives of Thesis

This PhD dissertation is an experimental study on particle generation with high-intensity lasers. Within the scope of this work several experiments were performed in France at Laboratoire d'Optique Appliquée and in England at Rutherford Appleton Laboratory, whose aims were to :

1. Generate electrons, protons as well as neutrons by laser plasma interactions in continuation of previously conducted work;
2. Characterize these particle sources by means of energy, yield, emission profile, angular divergence and emittance;
3. Decipher the mechanisms occurring during these interactions;
4. Propose and possibly realize applications in comparison to conventional particle sources.

1.3 Thesis Outline

This manuscript is divided into four parts, whereas the first is dedicated to theoretical basics of particle generation and acceleration mechanisms during relativistic laser plasma interactions. The additional three parts cover experimental studies on neutron, electron as well as proton generation :

- **Part I** will present the scientific context of this thesis, i.e., basic laser and plasma characteristics will be introduced as well as physical processes of interest during the interaction of a relativistic high-intensity laser with an underdense / overdense plasma.
  For the underdense regime the generation of relativistic electron plasma waves will be summarized, which can result in the self-modulated laser wakefield scheme in an energetic electron beam. Furthermore, ion acceleration by the known Coulomb

explosion will be described. For the overdense regime the laser plasma interaction will be briefly considered in the context of proton beam generation.

- **Part II** will introduce methodological basics of neutron generation by $D(d,n)^3He$ reactions since this can reveal information about ion kinetics and possible ion heating mechanisms in plasmas.
  Subsequently the set-up for this experiment, pursued in the underdense regime, will be described in detail. The experimental results will be discussed for the gas jet interaction as well as for the beam target model since it was deduced that plasma ions are heated during this interaction to fusion temperatures of about 1 keV.

- **Part III** describes the generation of an electron beam with an energy of up to 200 MeV in a new regime termed "Forced Laser Wakefield." Here, the presented experimental results were for the first time fully explained and even extended by the numerical modelling of this interaction in terms of energy, yield, angular divergence, emittance as well as bunch length of this electron beam.
  Applications of this electron beam for accelerator physics and the generation of secondary X-rays via the channelling effect and Thomson scattering will be assessed theoretically. The utilization of such an electron beam for current quests in ultra fast radiation chemistry will be demonstrated experimentally.

- **Part IV** will delineate a 10 MeV proton beam generation using foil targets and a 10 Hz laser. Again the kinematic simulation of this experiment is in agreement with the experimental results by means of yield and angular divergence.
  Calculating the production of medical isotopes with this proton beam indicated that this approach can indeed be competitive with contemporary accelerators, providing kHz repetition rates of the laser used. An example that such a proton beam can probe laser plasma interactions will be presented, which demonstrates its superiority in terms of spatial and temporal resolution compared to conventional sources.

Finally, a summary of the observed results will be given and suggestions will be made, how these studies can and should be extended in the very near future. Some interesting, ambitious and particularly important perspectives will conclude this manuscript.

Part I

Theoretical Basics

Chapter 2

Particle Acceleration Mechanisms

By way of introduction, a brief review on essential laser and plasma parameters will be given. Their interaction will subsequently be presented for overdense and underdense plasmas, as well as for this manuscript essential particle generation and acceleration mechanisms.

2.1 Elementary Definitions

In the following, basic laser characteristics like intensity and ponderomotive force will be considered. As for high-intensity lasers the potential of their electric field exceeds by far the ionization threshold of matter, plasmas can be instantaneously created by the pedestal of these laser pulses. Therefore, relevant plasma generation mechanisms will be revealed and basic plasma characteristics subsequently discussed.

2.1.1 Laser Parameters

Lasers emit monochromatic and coherent electromagnetic radiation, whose propagation is described by the Maxwell equations [11]. Today, they do cover a wide range of wavelengths as well as applications [12], which is why in the following only short pulse lasers with a pulse length below 1 ps will be regarded, since in the manuscript presented here, the experiments were performed on such laser systems.

2.1.1.1 Laser Intensity

The electric as well as magnetic field of these lasers are assumed to have a Gaussian profile, which can be decoupled spatially and temporally. Since these fields are perpendicular to each other, their vector product gives both the direction and the quantity of energy flow. Its mean value is the intensity, I, which is in a focal spot given by

$$I(r,t) = I_L \exp\left(-2\left(\frac{r}{w_0}\right)^2\right) \exp\left(-4\ln 2\left(\frac{t}{\tau_0}\right)^2\right), \tag{2.1}$$

where τ_0 is the full width at half maximum (FWHM) of the pulse length and w_0 the waist of the focal spot, which is the laser beam diameter at e^{-1} of its amplitude. Integrating $I(r,t)$ over space and time, reveals the maximum laser amplitude, I_L, to be

$$I_L \simeq 0.6\,\frac{E_L}{w_0^2\,\tau_0}, \tag{2.2}$$

where E_L is the laser pulse energy. Clearly, focusing a 1 J laser with a 30 fs FWHM pulse length onto a 18 μm spot containing 50% of the laser energy results in an intensity of about 3×10^{18} W/cm^2.

Importantly, the envelope and therefore the intensity of such a focused laser pulse changes with distance along the laser propagation axis, z, as

$$w(z) = w_0\,\sqrt{1+\left(\frac{z}{z_R}\right)^2}, \tag{2.3}$$

where z_R is the Rayleigh length, which is given as a function of the laser wavelength, λ_L, by

$$z_R = \frac{\pi\,w_0^2}{\lambda_L}. \tag{2.4}$$

This Rayleigh length is thus the distance over which the laser intensity decreases by a factor of 2 relative to the intensity in the focal spot. Assuming that a laser with a wavelength of 820 nm is focused down to a focal waist of 4 μm, z_R is about 61 μm.

Relativistic Laser Intensity

Today, intensities well in excess of 10^{18} W/cm^2 are commonly available at many laboratories worldwide. Since the associated electric field of such a laser pulse is given in (V/m) by

$$E = 2.7 \times 10^{12}\,\sqrt{I_{18}}, \tag{2.5}$$

where I_{18} is the laser intensity in (10^{18} W/cm^2), their impact on matter has obviously to be considered. Therefore, it is convenient to define a normalized vector potential, a_0, which corresponds to the normalized, classical, velocity of free electrons, $v_\perp/c$, oscillating in a linearly polarized electric laser field by

$$\begin{aligned} a_0 = v_\perp/c &= \sqrt{\frac{1}{2\pi^2\epsilon_0}\,\frac{e^2}{m_e^2c^5}\,\lambda_L^2\,I_L} \\ &= 0.85\,\lambda_L\,(\mu\mathrm{m})\,\sqrt{I_{18}}. \end{aligned} \tag{2.6}$$

Here, $-e$ and m_e are the charge and the mass of an electron, ϵ_0 the permittivity of free space and c the speed of light in vacuum. Consequently, for $a_0 > 1$ electrons will be relativistic and the component of the Lorentz force induced by the laser, $\vec{v}_\perp \times \vec{B}$, has to be taken into account since electrons can acquire an additional longitudinal movement from this force.

2.1.1.2 Ponderomotive Force

As free electrons quiver in the electric field of such laser pulses they are subjected to a variation of the laser intensity. This can be expressed in the non-relativistic case with the fluid equation of motion within an electromagnetic field by

$$\frac{\partial \vec{v}}{\partial t} + (\vec{v} \cdot \nabla)\, \vec{v} = -\frac{e}{m_e} \left(\vec{E} + \vec{v} \times \vec{B} \right), \tag{2.7}$$

where $\vec{v}$ is the electron velocity vector. This equation can be developed to second order to the ponderomotive force, $\vec{F_p}$, given as

$$\vec{F_p} = -\frac{e^2}{4 m_e \omega_L^2} \nabla(E^2) = -\frac{e^2}{2 c \epsilon_0 m_e \omega_L^2} \nabla I, \tag{2.8}$$

by time averaging the electric laser field, when ω_L describes the laser period [13]. As it is indicated in Fig. 2.1 electrons are pushed by this force along the intensity gradient, i.e., away from the focal spot of the laser, where the intensity is the greatest. Furthermore, as mentioned above, the inclusion of the Lorentz force distorts the oscillation of the electrons and can drive electrons along the direction of propagation of the laser. An analytical solution for the relativistic case is given in [14].

Figure 2.1: Scheme of the laser ponderomotive force. Due to the transverse oscillation of electrons in the electric laser field they get accelerated perpendicularly towards the laser axis. Additionally, they can get pushed along the laser propagation axis for sufficiently short laser pulses.

Self-explanatory, it is possible to ascertain the laser a ponderomotive potential, Φ_p, which is

$$\Phi_p = \frac{e^2 E^2}{4 m_e \omega_L^2}. \tag{2.9}$$

For a laser intensity beyond 10^{17} W/cm^2 this ponderomotive potential exceeds 6 keV, which is by far stronger than the binding energy between an electron and a nucleus. It is thus Φ_p that can induce the generation of a plasma in a target such a laser is focused onto. It is clear that not the maximum laser intensity is required for this ionization but that the pedestal of the laser pulse is sufficient.

2.1.2 Plasma Parameters

A plasma is an electrically conducting collection of free, positively and negatively charged particles as well as neutral atoms and molecules. The permanent and unsorted motion of these particles defines a temperature of this many-body system and corresponds to their kinetic energy, which can be beyond the ionization energy of matter.

2.1.2.1 Plasma Creation

At laser intensities beyond 10^{17} W/cm^2 atomic electrons can be rapidly ionized by the sole influence of the electric field of the laser. Hence, a plasma is created. Many theoretical approaches tried to predict this plasma creation, whereas one of the simplest was derived by Keldysh, which used perturbation theory of a simple atom [15]. However, it makes no allowance for the internal structure of the atom and is thus only really applicable for hydrogen and helium, but it can be approximated for high as well as low laser intensities. Here, the Keldysh parameter, γ_K, which is defined as the square root of the ratio of the ionization potential, ε_i, to twice the ponderomotive potential distinguishes between different ionization regimes

$$\gamma_K = \sqrt{\frac{\varepsilon_i}{2\,\Phi_p}}. \tag{2.10}$$

Multi Photon Ionization

The case $\gamma_K > 1$ is considered as the multi photon ionization regime, which is the process where the atom passes through the absorption of single photons through multiple short lived virtual states to gain sufficient energy to become ionized. This is the dominant process when the laser intensity is relatively low and the laser frequency is high.

Tunnel Ionization

For $\gamma_K < 1$, or tunnel ionization regime, it becomes energetically preferential for atomic electrons to exist unbound but they are prevented from leaving the atom by the Coulomb barrier. This barrier is reduced by the laser electromagnetic field so that it is energetically preferable for atoms to exist ionized [16]. Since the electronic wave function can penetrate this barrier it is possible that electrons can quantum mechanically tunnel through the Coulomb barrier.

Barrier Suppression Ionization

For the extreme case $\gamma_K \ll 1$ the atomic Coulomb barrier is suppressed, liberating electrons [17]. An estimate of the required laser intensity, I_{BSI}, can be obtained by equating the ionization potential for a given ionization state to the potential experienced by an electron for a given laser intensity. This potential is a combination of the Coulomb field, which is corrected for screening effects of the inner electrons and the maximum electric field of the laser. I_{BSI} is then given in (W/cm^2) as

$$\begin{aligned} I_{BSI} &= \frac{\pi^2 \epsilon_0^3 c}{2 e^6} \frac{\varepsilon_i^4}{Z^2} \\ &= 4 \times 10^9 \frac{\varepsilon_i^4(\mathrm{e}V)}{Z^2}, \end{aligned} \tag{2.11}$$

where Z is the ionization state of the ionized atom. Table 2.1 gives some ionization energies and intensity thresholds according to this BSI model. In [18] it was shown that this ionization process is completely induced before the main laser pulse arrives.

Solid State

As mentioned earlier, γ_K is only really applicable for simple atoms. Obviously, this is not the case for solid states where complex atoms are bound into a crystal lattice,

Table 2.1: Ionization energies [22] and resulting intensity thresholds according to the BSI model for deuterium and helium.

Gas species	Potential threshold (eV)	I_{BSI} (W/cm^2)
D	13.5	1.3×10^{14}
He^+	24.6	1.4×10^{14}
He^{2+}	54.4	8.8×10^{15}

which changes the ionization potential. However, it was shown in numerical [19] as well as analytical approaches [20] that these above described ionization mechanisms are still the dominant processes for plasma generation in solid states. This agrees with experimental results, where the creation of a plasma in aluminium foils was found to occur for intensities beyond 10^{12} W/cm^2 [21].

In summary, it has been shown that plasmas are instantaneously created on gaseous and solid targets by the pedestal of commonly available laser pulses with intensities beyond 10^{18} W/cm^2. It is noted that the contrast ratio of such laser impulsions is crucial for the subsequent laser plasma interaction. This contrast ratio is defined as the ratio of the laser intensity at its maximum over the intensity in the ns time scale before the main impulsion. Obviously, a laser with a low contrast ratio is capable to significantly heat the target before the main laser pulse arrives. This can result in the generation of a preplasma and compounds the numerical modelling of the subsequent interaction.

2.1.2.2 Plasma Characteristics

A plasma is characterized by several macroscopic values such as the electron and ion temperature, T_e and T_i, the electron density, n_e, and the mean charge state, $\langle Z \rangle$. In case plasma electrons move coherently, electron plasma waves are created, which do have the following characteristics :

Plasma Frequency

If plasma electrons are displaced from their equilibrium position they will experience a restoring force from the electrostatic field created by this charge separation. For small oscillations this leads to the so-called plasma frequency, ω_p, given in (rad/s) by the expression

$$\begin{aligned} \omega_p &= \sqrt{\frac{n_e e^2}{\epsilon_0 m_e}} \\ &= 5.64 \times 10^4 \sqrt{n_e}. \end{aligned} \tag{2.12}$$

Assuming a plasma electron density of 2×10^{19} cm^{-3}, this plasma period is 25 fs. In contrast, plasma ions with mass m_i and charge Z oscillate with the period

$$\omega_{pi} = \sqrt{Z \frac{m_e}{m_i}}\, \omega_p. \tag{2.13}$$

Due to the significant mass difference between electrons and ions these waves oscillate much slower than electron plasma waves. For an electron density of 1×10^{19} cm^{-3}

in a helium plasma, ω_{pi}^{-1} is around 300 fs. Since this is about ten times below the corresponding electron plasma period, this ion oscillation is neglected during their first cycles.

Dispersion Relation

For an electromagnetic wave, $(\omega, \vec{k})$, propagating through a plasma the dispersion relation is given as

$$\omega^2 = \omega_p^2 + c^2 k^2, \tag{2.14}$$

where k is the wavenumber. As electron plasma waves are electrostatic waves, which can be described by an oscillating electron density modulation, δn_e, as

$$\delta n_e = \delta n_0 \exp[-i(\vec{k_p} \cdot \vec{r} - \omega_p t)], \tag{2.15}$$

they fulfill the dispersion relation known as the Bohm-Gross frequency

$$\omega_{pe}^2 = \omega_p^2 + 3k_p^2 v_{th}^2, \tag{2.16}$$

where $v_{th}^2 = T_e/m_e$ is the square of the thermal electron velocity. Clearly, these are these waves, which are essential for particle acceleration by laser plasma interactions as they build up the accelerating fields in a plasma.

Slower electrostatic modes, known as ion acoustic waves, can also exist in a plasma. These fulfill the dispersion relation

$$\omega_i = k_i c_s, \tag{2.17}$$

where c_s is the ion sound velocity given in (cm/s) by

$$c_s = 41.92 \times 10^6 \sqrt{\left(Z + \frac{3T_i}{T_e}\right) \frac{m_e}{m_i} T_e}, \tag{2.18}$$

when T_e is expressed in (eV).

Phase Velocity

Self-explanatory, a phase velocity, v_Φ, can be associated with high-intensity laser pulses propagating through plasmas. From the dispersion relation its square value is given by

$$v_\Phi^2 = \frac{\omega^2}{k^2} = c^2 + \frac{\omega_p^2}{k^2} = \left(\frac{c}{n}\right)^2, \tag{2.19}$$

where n is the index of refraction of a plasma

$$n = \sqrt{1 - \frac{\omega_p^2}{\omega^2}}. \tag{2.20}$$

Critical Density

Obviously, a laser can only propagate through a plasma if the laser frequency is superior the plasma frequency, $\omega_L > \omega_p$. This defines a critical electron density, n_c, in (cm^{-3}) from which an electromagnetic wave is reflected

$$\begin{aligned} n_c &= \sqrt{\frac{\epsilon_0\, m_e\, \omega_L^2}{e^2}} \\ &= \frac{1.1 \times 10^{21}}{\lambda_L^2(\mu\mathrm{m})}. \end{aligned} \tag{2.21}$$

This critical density distinguishes two different laser plasma interaction regimes. For the case $n_e < n_c$, the plasma is referred to be underdense, since the laser can propagate through it. For $n_e > n_c$, Eq. 2.14 leads to an imaginary wavenumber, k, and the electromagnetic wave decays as an evanescent wave beyond the critical surface, where n_c occurs. Such a plasma is termed overdense.

The underdense regime is experimentally realized by focusing the high-intensity laser on gas jets or thin foils, which explode when the pedestal of the laser pulse arrives. Self-explanatory, much thicker targets are used for the overdense regime. It is evident that laser plasma interactions are different in these two regimes, which is why in the following particle acceleration mechanisms for underdense and overdense plasmas will be regarded separately.

2.2 Underdense Plasma

The interaction of a high-intensity laser with an underdense plasma can stimulate plasma electrons to oscillate with high amplitudes. This leads to the generation of electric fields, which can be capable to accelerate particles to high energies. Due to the great variety of acceleration mechanisms, one will focus in the following on those, which have an important impact on the experiments presented in this manuscript. These mechanisms will first be introduced by their basic 1D physical phenomena and will subsequently be enhanced to higher orders.

2.2.1 Nonlinear Optics Phenomena

For short pulse lasers with a normalized vector potential grater than one, the theory of nonlinear plasma optics only involves electron motion since ions are, due to their higher mass, regarded to be immobile during the transit time of such laser pulses. Thus, neglecting ion motion, the number of instabilities to occur is significantly limited to forward Raman scattering [23], relativistic self-focusing [24] and relativistic self-phase modulation [25]. Each of these is usually described as a four wave process in which the incident electromagnetic wave $(\omega_L, \vec{k}_L)$ of a laser focused onto a plasma decays into two forward moving electromagnetic side-bands at frequencies $\omega_L - \omega$ (Stokes wave) and $\omega_L + \omega$ (anti-Stokes wave), where ω corresponds to modulations to the refractive index, n, which is determined by the oscillation of plasma electrons. In forward Raman scattering (FRS), $\omega = \omega_p$, which results in the generation of an electrostatic plasma wave with a phase velocity, v_Φ, close to the speed of light [26]. For this instability to occur, the condition $\omega_L \geq 2\omega_p$ must be met, or in terms of the plasma density, $n_e \leq n_c/4$, as otherwise the scattered photons would be unable to propagate through the plasma.

Naturally, any of these instabilities needs a noise-source, δn_s, to grow from. Such a density perturbation can be excited by the pedestal of the laser impulsion itself, as will be discussed in the following.

2.2.1.1 Noise-Sources

The determination of the noise-source, δn_s, shows a great dependence on the initial laser pulse shape. Here, a truncated Gaussian laser pulse with an amplitude A is usually approximated since this is the closest for a real experimental impulsion. Such a pulse profile is given by

$$A(\Xi) = a_0 \left[10 \left(\frac{\Xi}{c\tau_0} \right)^3 - 15 \left(\frac{\Xi}{c\tau_0} \right)^4 - 6 \left(\frac{\Xi}{c\tau_0} \right)^5 \right], \tag{2.22}$$

where $\Xi = ct - z$ corresponds to the position relative to the front of the pulse. A simple expression for the noise-level plasma wake for such a laser impulsion was in [27] derived to be

$$\frac{\delta n_s}{n_e} = 0.9\,\pi \frac{a_0^2}{(k_p\, c\tau_0)^q}, \tag{2.23}$$

where $q = 2$ for $k_p c\tau_0 < 10$ and $q = 2.8$ for $k_p c\tau_0 > 10$. Clearly, for a laser intensity of 5×10^{18} W/cm^2, a laser wavelength of 1μm, a pulse length of 800 fs and an electron density of 10^{19} cm^{-3} the relative plasma wake comes out to be 2.5×10^{-6}. However, for the same conditions, but a pulse length of solely 30 fs, this wake is 3.2×10^{-1}.

2.2.1.2 Modulation of Refractive Index

Each of the aforementioned instability arises when stationary modulations in the index of refraction, n, appear in the light wave's frame. Therefore, the refractive index needs to have a relativistic phase velocity, v_Φ. In an unmagnetized plasma, n is given by

$$n = \sqrt{1 - \frac{\omega_p^2}{\gamma_\perp \omega_L^2}}, \tag{2.24}$$

where $\gamma_\perp = (1 + a_0^2/2)^{1/2}$ accounts for the relativistic correction of the high-intensity laser pulse. For small modulations and weakly relativistic laser pulses this can be expanded as

$$n = \left(1 - \frac{1}{2}\frac{\omega_p^2}{\omega_L^2}\left(1 + \frac{\delta n_e}{n_e} - \frac{\langle a^2\rangle}{2} - 2\frac{\delta\omega_L}{\omega_L}\right)\right), \tag{2.25}$$

where $\langle . \rangle$ represents averaging over fast laser oscillations [28]. With this expression the laser phase velocity, v_Φ, in a plasma is determined in [29] as

$$v_\Phi = \frac{c}{n} = c\left(1 + \frac{1}{2}\frac{\omega_p^2}{\omega_L^2}\left(1 + \frac{\delta n_e}{n_e} - \frac{\langle a^2\rangle}{2} - 2\frac{\delta\omega_L}{\omega_L}\right)\right), \tag{2.26}$$

and the group velocity, v_g, as

$$v_g = cn = c\left(1 - \frac{1}{2}\frac{\omega_p^2}{\omega_L^2}\left(1 + \frac{\delta n_e}{n_e} - \frac{\langle a^2\rangle}{4} - 2\frac{\delta\omega_L}{\omega_L}\right)\right). \tag{2.27}$$

Assuming that within a local volume with some initial longitudinal extend, L, the classical action is conserved as

$$\langle a^2\rangle \omega_L w^2 L = \text{const.}, \tag{2.28}$$

it is evident that the laser's vector potential can only be modulated either by L, which results in longitudinal bunching, or by w for transverse focusing, or by ω_L, which leads to photon acceleration. The overall change in a^2 is therefore

$$\triangle\langle a^2\rangle = -\frac{\triangle L}{L}\langle a^2\rangle - 2\frac{\triangle w}{w}\langle a^2\rangle - \frac{\triangle\omega_L}{\omega_L}\langle a^2\rangle. \tag{2.29}$$

As n is supposed to be stationary in the light wave's frame, it is for the following convenient to define the so-called speed of light variables, $\psi = t - z/c$ and $\tau = t$.

2.2.1.3 Longitudinal Bunching of Laser Envelope

With Eq. 2.27 it is clear that the laser pulse in segments with a lower electron density, $\delta n_e/n_e$, has a higher group velocity. Assuming that the laser pulse length is much in excess of the plasma wavelength, this leads to an energy dispersion of the electromagnetic wave in those regions and consequently to an energy compression of the laser envelope in the regions with higher electron densities. Since this changes the laser ponderomotive force a larger plasma wave is excited and the process feeds back on itself. As a result, the laser intensity is modulated at nearly the plasma frequency, ω_p^{-1}, which is indicated in Fig. 2.2.

Formally, the change in separation between two positions of the laser envelope,

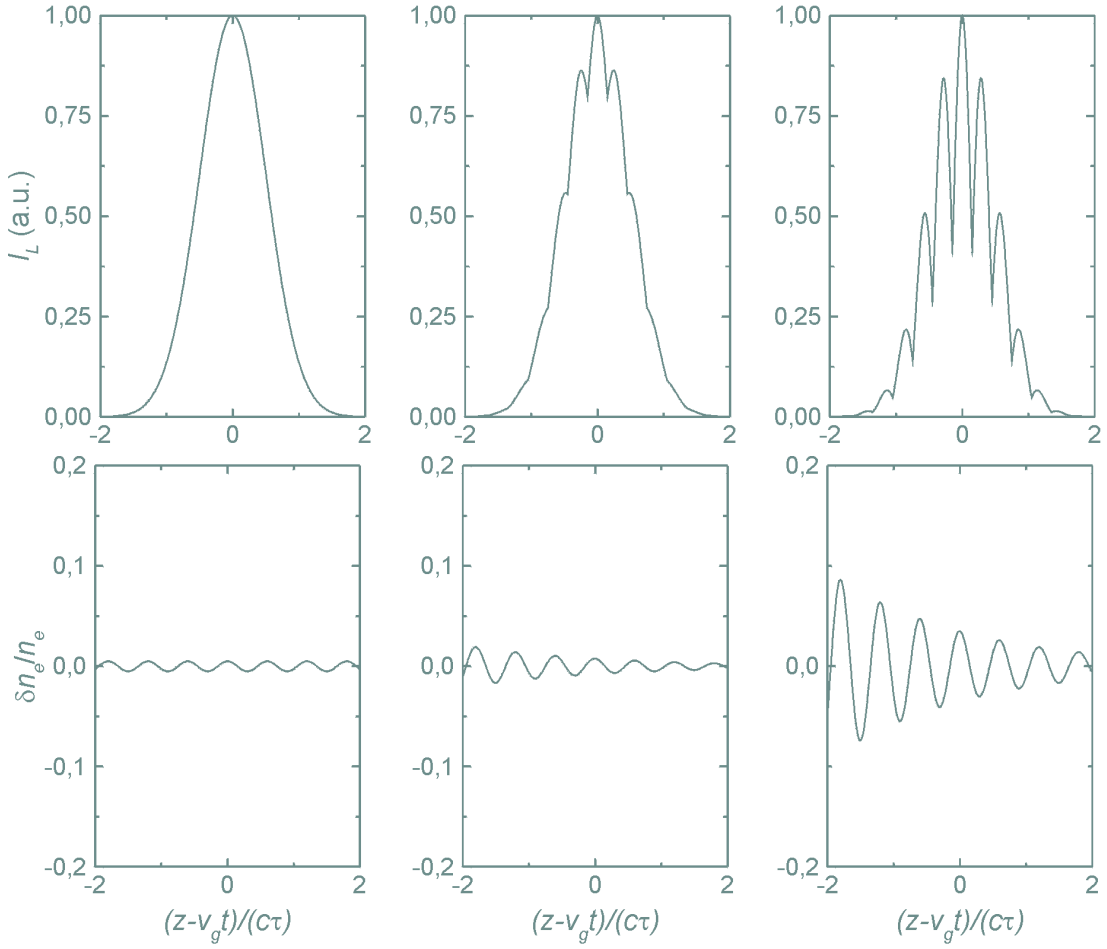

Figure 2.2: Principle of forward Raman scattering for three evolving time steps. As a high intensity laser propagates through an underdense plasma with a period of less than the laser pulse length, the amplitude of the plasma wave gets amplified and the laser beam envelope modulated at ω_p^{-1}.

which are assumed to be near to each other can then be expressed as

$$\triangle L = L\frac{\partial v_g}{\partial z}\triangle t = -\frac{L}{c}\frac{\partial v_g}{\partial \psi}\triangle t, \tag{2.30}$$

when $\triangle t$ represents a change in time while ψ is fixed. Consequently, the rate that two positions bunch towards each other due to variations to v_g is given as

$$\frac{1}{L}\frac{\partial L}{\partial \tau} = -\frac{1}{c}\frac{\partial v_g}{\partial \psi}. \tag{2.31}$$

Hence, the longitudinal bunching of the laser envelope is caused by longitudinal variations in the group velocity. Since this can induce a loop among these two effects this can result at the end in the full modulation of the laser envelope at ω_p^{-1}.

2.2.1.4 Transverse Laser Focusing

To achieve that electron plasma waves can be used to efficiently accelerate electrons they have to exist over long distances. However, with Eq. 2.3 it is clear that the intensity of a focused laser beam decreases by a factor of 2 over the Rayleigh distance, z_R. This obviously limits the distance over which the plasma wave can grow. However, this can be overcome by the transverse modulation of the refractive index [30].

As the laser focal spot has a spatial Gaussian profile, the maximum velocity of electrons oscillating in the laser beam is higher the closer they are to the center of the focus. As $\omega_p^2 \sim (\gamma_\perp m_e)^{-1}$ the index of refraction of a plasma increases the faster electrons oscillate. This increase in the refractive index where the intensity across the laser wave front is at its greatest leads to a relative retardation of the wave front and therefore to relativistic self-focusing of the laser beam.

Like it is indicated in Fig. 2.3 the outer part of this wavefront has to curve forward in order to focus the laser beam. For a time interval, $\triangle t$, the angle, θ, a wavefront bends forward is

Figure 2.3: Scheme of transverse laser focusing. In case $v_{\Phi,1} > v_{\Phi,0}$ the wavefront will bend forward to focus the laser at an angle θ.

$$\theta = -\left(\frac{v_{\Phi,0} - v_{\Phi,1}}{w}\right) \triangle t. \tag{2.32}$$

Obviously, energy flows normal to the phase front. Therefore, the transverse component of the energy velocity is $c \sin\theta$ and the energy is focused inwards with a velocity close to $c\theta$, if θ is assumed to be small. This velocity is equal to the time rate of change of the laser spot size, thus

$$\frac{\partial w}{\partial \tau} = -c\theta = c\left(\frac{v_{\Phi,0} - v_{\Phi,1}}{w}\right) \triangle t. \tag{2.33}$$

Differentiating with respect to time gives

$$\frac{\partial^2 w}{\partial \tau^2} = c\left(\frac{v_{\Phi,0} - v_{\Phi,1}}{w}\right), \tag{2.34}$$

which is the acceleration of the spot size caused by transverse variations in v_Φ. Note that if $v_{\Phi,0} > v_{\Phi,1}$ then the spot size increases, hence, defocusing occurs.

2.2.1.5 Photon Acceleration

In photon acceleration, the local frequency changes because of longitudinal variations in v_Φ. As the laser phase front moves in a time interval, $\triangle t$, a certain distance according to their phase velocity, one can write the time rate of change of the laser frequency

$$\frac{1}{\omega_L}\frac{\partial \omega_L}{\partial \tau} = \frac{1}{c}\frac{\partial v_\Phi}{\partial \psi}, \tag{2.35}$$

using the speed of light variables. Therefore, as a photon moves along in an index of refraction gradient which it views as stationary, its frequency increases if the slope is positive. This process is called photon acceleration since the waves's frequency is directly related to v_g [31].

In summary, up to now it has been shown that variations in the relativistic group and phase velocity of the refractive index in a plasma wave lead to a modulation of the laser envelope and consequently to different laser intensities. As these processes feed back on themselves the generated plasma wave is amplified. Their growth rates will be dealt with in the next section.

2.2.2 Plasma Wave Growth Rates

In this section the growth rates of the aforementioned instabilities will be discussed. It will be shown, that the interplay between the modulation of the laser envelope and relativistic self-focusing can dramatically increase the amplitude of the excited plasma wave, which can result in the generation of an electron beam.

2.2.2.1 Raman Forward Scattering

In the 1D limit, the laser intensity can only be modulated by laser focusing and photon acceleration. Hence, Eq. 2.29 simplifies to

$$\triangle\langle a^2\rangle = -\frac{\triangle L}{L}\langle a^2\rangle - \frac{\triangle\omega_L}{\omega_L}\langle a^2\rangle, \tag{2.36}$$

and evolves in time as

$$\frac{\partial\langle a^2\rangle}{\partial\tau} = -\frac{1}{L}\frac{\partial L}{\partial\tau}\langle a^2\rangle - \frac{1}{\omega_L}\frac{\partial\omega_L}{\partial\tau}\langle a^2\rangle. \tag{2.37}$$

Since in FRS the modulations to n are solely the result of modulations to δn_e, this can be rewritten by applying the above given expressions for transverse focusing and photon acceleration as

$$\frac{\partial\triangle\langle a^2\rangle}{\partial\tau} = -\frac{\omega_p^2}{\omega_L^2}\langle a^2\rangle\frac{\partial}{\partial\psi}\frac{\delta n_e}{n_e}. \tag{2.38}$$

Defining $\delta n_e/n_e = (n_1/2)\exp i(k_p z - \omega_p t) + cc$, where n_1 depends slowly with both ψ as well as τ and $a = (a_0/2)\exp i(k_L z - \omega_L t) + cc$ this results in

$$\frac{\partial\triangle\langle a^2\rangle}{\partial\tau} = ic\frac{\omega_p^2}{\omega_L^2}k_p\frac{a_0^2}{2}\frac{\delta n_e}{n_e}. \tag{2.39}$$

Consequently, in FRS the modulations to $\langle a^2\rangle$ are $\pi/2$ out of phase with the density response, $\delta n_e/n_e$.

To decipher the FRS growth rate the well known harmonic oscillator equation is used as this equation describes how modulations to $\langle a^2\rangle$ cause density perturbations [30]. With the speed of light variables this equation becomes

$$\left(\frac{\partial^2}{\partial\psi^2} + \omega_p^2\right)\frac{\delta n_e}{n_e} = \frac{\partial^2}{\partial\psi^2}\frac{\langle a^2\rangle}{2}. \tag{2.40}$$

In [28] it was shown in detail that this equation leads to the growth rate of FRS given by

$$\frac{\partial^2}{\partial\psi\partial\tau}\langle a^2\rangle_1 = \frac{k_p^2c^2}{8}\frac{\omega_p^2}{\omega_L^2}a_0^2\langle a^2\rangle_1, \tag{2.41}$$

with

$$\triangle\langle a^2\rangle = \frac{\langle a^2\rangle_1}{2}\exp\left(-i\omega_p\psi\right) + cc, \tag{2.42}$$

which leads to the asymptotic solution

$$\langle a^2\rangle_1 \sim \exp\left(\frac{a_0}{\sqrt{2}}\frac{\omega_p}{\omega_0}\omega_p\sqrt{\psi\tau}\right). \tag{2.43}$$

Clearly, for the example of the 800 fs laser pulse duration given for the noise-source the gain induced by a 1 μm laser is about 3×10^5. Analyzing $\langle a^2\rangle_1$ as a function of the normalized laser vector potential it is evident that the growth rate has a maximum at $a_0 = 1$. The reason for this is that ω_p is inversely proportional to $\sqrt{m_e}$. As the laser intensity increases, the quiver velocity of the electrons increases, the plasma frequency decreases and so does the gain.

2.2.2.2 Relativistic Self-Focusing

The evolution of a laser beam focus with a Gaussian profile was given in Eq. 2.3. Considering nearly planar wavefronts, i.e., regions near the focus, this equation can be differentiated twice to get

$$\frac{\partial^2 w}{\partial\tau^2} \approx \frac{4}{k_L^2 w_0^3}, \tag{2.44}$$

which has to be added to Eq. 2.34 since in the absence of variations in v_Φ the spot size increases due to diffraction. Hence,

$$\frac{\partial^2 w}{\partial\tau^2} = \frac{4}{k_L^2 w_0^3}\left(1 - \frac{a_0^2}{32}w_0^2\frac{\omega_p^2}{c^2}\right). \tag{2.45}$$

As self-focusing occurs if the term in brackets is negative a laser power threshold, P_c, for relativistic self-focusing to occur is given in (TW) as

$$\begin{aligned} P_c &= \frac{8\pi\,\epsilon_0\,m_e^2\,c^5}{e^2}\frac{n_c}{n_e} \\ &= 1.7\times10^{-2}\frac{n_c}{n_e}. \end{aligned} \tag{2.46}$$

This laser power threshold is for a 1 μm laser propagating through a plasma with an electron density of 10^{19} cm^{-3} about 1.9 TW.

Complete expulsion of electrons from the laser focal spot due to the laser ponderomotive force not only enhances self-focusing of the laser beam but can also serve to guide the laser over many Rayleigh lengths [32, 33]. As relativistic self-focusing changes the normalized vector potential of the laser this modifies the plasma refractive index. Consequently, multiple foci are possible as the laser propagates through the plasma [34].

In conclusion, due to the modulation of the refractive index of a relativistic plasma wave an interplay between FRS and the self-modulation of the laser beam envelope is initiated. This can resonantly drive an initial plasma wake to high amplitude. If additionally the laser power is beyond the threshold for relativistic self-focusing this plasma wave can grow over distances exceeding the diffraction limit of the laser. As a result this can lead to the generation of an energetic electron beam as will be shown in the following.

2.2.3 Wavebreaking – Electron Beam Generation

So far it has been shown that the interaction of a high-intensity laser with an underdense plasma can create electron plasma waves. In the self-modulated laser wakefield (SMLWF) regime these plasma waves are the electron source themselves once they break and accelerate background electrons. In the following the accelerating fields as well as the energy gain of these electrons will be deciphered.

2.2.3.1 Wavebreaking

Principally, an electron beam provided by an external source can be injected into an electron plasma wave as long as the electron beam energy fulfills the trapping condition mentioned below. However, in the SMLWF regime this electron plasma wave is the electron source itself [7]. Here, plasma electrons are accelerated once the amplitude of the plasma wave has exceeded a limiting value known as wavebreaking. This wavebreaking occurs because some of the plasma electrons undergo such large oscillations that the returning force due to the plasma wave is no longer large enough to make them continue their longitudinal oscillation. Instead the electrons can continue into the next wave 'bucket.' If this is the forward travelling 'bucket,' then the electron, instead of feeling a returning force, will feel a continued acceleration, so resulting in its trapping within the plasma wave. The trapped electrons continue to be accelerated until their velocity exceeds that of the plasma wave and "out-run" the wave and are dephased.

2.2.3.2 Acceleration Fields

Linear Case

Longitudinal electron plasma waves can be described as $\delta n_e/n_e = \delta \sin[k_p(z - v_\Phi t)]$, where δ is the plasma wave amplitude. From Poisson's equation it is possible to derive the amplitude of the associated longitudinal accelerating fields, E_p, by

$$\nabla \cdot \overrightarrow{E_p} = -e\frac{\delta n_e}{\epsilon_0} = -E_{p0} \sin[k_p(z - v_\Phi t)], \tag{2.47}$$

where $E_{p0} = \delta E_{max}$. For the maximum plasma wave amplitude, $\delta = 1$, this leads to

$$E_{max} = \frac{e n_e}{\epsilon_0 k_p} = \frac{m_e c \omega_p}{e}. \tag{2.48}$$

Hence, for an electron plasma density of 10^{19} cm^{-3} electric fields of the order of 300 GV/m are attainable. However, these expressions solely account for perfectly sinusoidal plasma waves.

Nonlinear Case

Since such plasma waves grow from FRS their amplitudes can increase drastically. This can result in a nonlinear behavior of these waves, from which they can loose their sinusoidal profile. This consequently changes the accelerating fields [35, 36]. In [37] it was calculated that the limit for this accelerating field, E_{WB}, is in the relativistic case

$$E_{WB} = \sqrt{2\gamma_\perp(\gamma_p - 1)} E_{max}, \tag{2.49}$$

where $\gamma_p = (1 - \beta_p)^{-1/2}$ is the relativistic Lorentz factor of the electron plasma wave, with $\beta_p = v_\Phi/c$. Hence, in this case, E_{max} can even be enhanced by a factor of 6 for an electron density of 10^{19} cm^{-3}.

Plasma Heating

So far the amplitude of electron plasma waves has been described by $\delta = \delta n_e/n_e$. Obviously, the impact of the $(1 - \delta)$ additional plasma electrons has been neglected. Their movement can be integrated to a temperature, T_e, which changes the wavebreaking threshold, E_{th}, according to [38] as

$$E_{th} = \left(\frac{m_e c^2}{3T_e}\right)^{1/4} \sqrt{\ln\left[2\sqrt{\gamma_\Phi}\left(\frac{3T_e}{m_e c^2}\right)^{1/4}\right]} E_{max}. \tag{2.50}$$

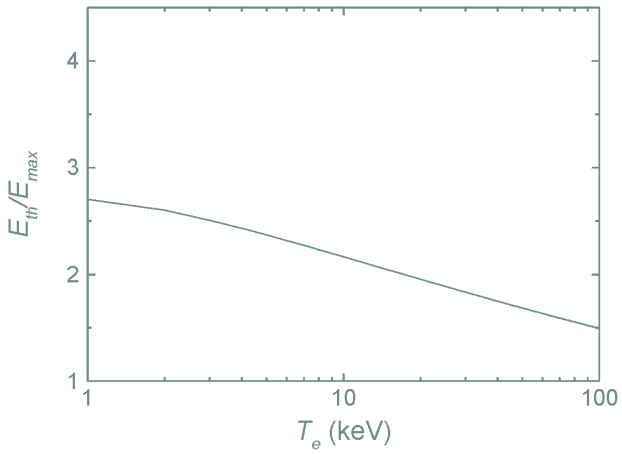

Figure 2.4: Accelerating field at wavebreaking threshold for a relativistic plasma wave with $\gamma_\Phi = 10$ as a function of ambient electron temperature.

This function is indicated in Fig. 2.4. Obviously, the hotter the ambient electron distribution the lower the accelerating field at wavebreaking.

2.2.3.3 Energy Gain

1D Approach

Due to their oscillation electron plasma waves have accelerating as well as decelerating segments like it is indicated in Fig. 2.5. Obviously, an electron is only accelerated

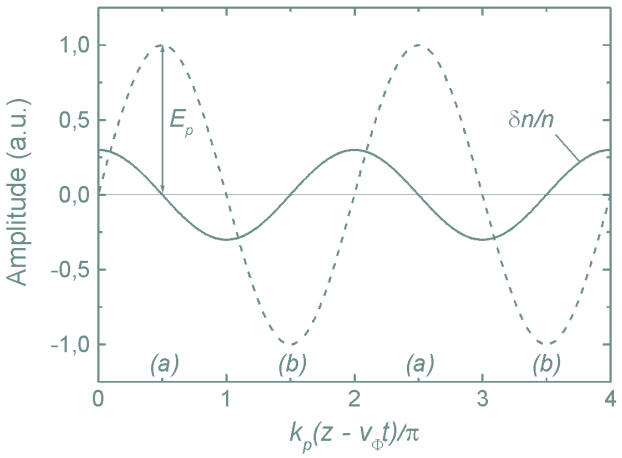

Figure 2.5: Plasma wave (solid line) in one dimension with the associated electric field (dashed line), including decelerating (a) and accelerating (b) segments.

over $k_p(L_{deph} - v_\Phi t) = \pi$, where L_{deph} is the dephasing length, which is the length over which an electron at a certain initial velocity gains half a plasma wavelength, which is the accelerating part of $\vec{E_p}$. Assuming the electron velocity to be about c this dephasing length then turns out to be

$$L_{deph} = \frac{\lambda_p}{2(1-\beta_p)} \cong \gamma_\Phi^2 \lambda_p, \tag{2.51}$$

where λ_p is the plasma wavelength and in case $\gamma_p \gg 1$ [39]. Consequently, the maximum energy, W_{max}, an electron can gain in such a plasma wave is

$$W_{max} = eE_p L_{deph} = 2\pi m_e c^2 \gamma_\Phi^2 \delta. \tag{2.52}$$

2D Approach

However, a plasma wave has a finite transverse dimension, which must be considered in a 2D approach as the focal spot of the laser, w_0, can be of the order of the plasma wavelength, λ_p. In this case the radial component of the electric plasma field either expels or attracts electrons to the center as it is indicated in Fig. 2.6. Consequently, L_{deph} turns out to be $\lambda_p/4$ in the center of mass frame of the wave, which yields in the laboratory system to

$$L_{deph}^{2D} \simeq \gamma_\Phi^2 \frac{\lambda_p}{2}. \tag{2.53}$$

Therefore the maximum energy an electron can gain in a 2D geometry is

$$W_{max}^{2D} = \pi m_e c^2 \gamma_\Phi^2 \delta. \tag{2.54}$$

2.2.3.4 Trapping Conditions

As it occurs for any acceleration process with oscillating electromagnetic waves, electrons need to have a initial kinetic energy to be trapped in such waves. Therefore, the potential of the wave in the wave frame has to be higher than the particle kinetic energy. In [40] the required injection energy of electrons, E_{inj}, was calculated to be

$$E_{inj} = \gamma_p^2 \left(\delta + \frac{1}{\gamma_p} - \beta_p \sqrt{\delta \left(\delta + \frac{2}{\gamma_p} \right)} \right) - 1. \tag{2.55}$$

In this case the electron is assumed at the minimum of the potential of the plasma wave so that it requires the minimum trapping condition and the maximum energy

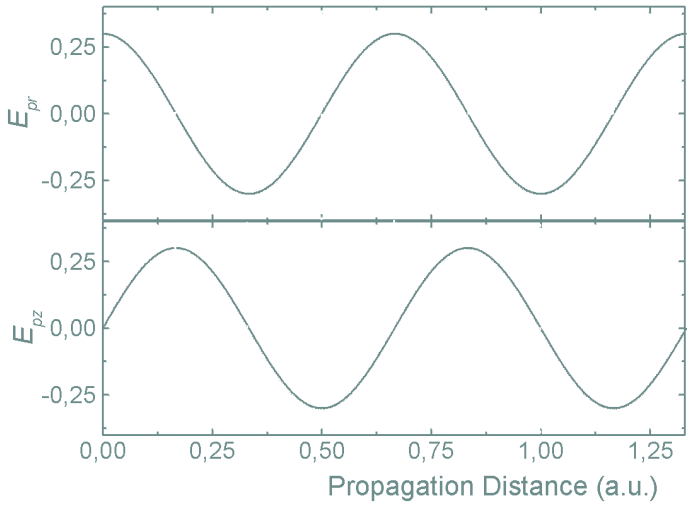

Figure 2.6: Accelerating and focusing segments for radial, E_{pr}, and longitudinal, E_{pz}, segments of a 2D plasma wave. In the wave frame L_{dep} turns out to be $\lambda_p/4$.

gain can be obtained. Analyzing Eq. 2.55 as a function of δ, it is evident that E_{inj} is negligible when the plasma wave amplitude approaches 1. Consequently any free electron is trapped independently of the plasma wave velocity.

So far, mainly the motions of electrons during the interaction of a high-intensity laser with a plasma have been regarded. Due to their much higher mass, these oscillations are in general too rapid for ions. However, if charge separation occurs over longer timescales, ions can react on the generated fields, as the mechanism of the Coulomb explosion shows.

2.2.4 Coulomb Explosion – Ion Beam Generation

The ponderomotive force, $\vec{F_p}$, was introduced in Chapter 2.1.1.2 as a function of the laser intensity gradient, which can expel electrons from the region of highest intensity. For relativistic laser intensities this ponderomotive force was in [41] shown to be

$$\vec{F_p} = \nabla(\gamma_\perp - 1)m_e c^2. \tag{2.56}$$

As it will be discussed later in Chapter 2.3.1 this ponderomotive force, $\vec{F_p}$, accelerates electrons to a Maxwellian-like energy distribution, which has an effective temperature, $T_{vB} = m_e c^2(\sqrt{1+a_0^2} - 1)$. As this induces a space charge separation ions with a mass, m_i, and charge, Z, could be accelerated to a velocity, u_i. This acceleration in the field of a linearly polarized laser beam was in [42] shown to be

$$\frac{du_i}{dt} = -\frac{Z}{m_i}\left(m_e c^2 \frac{\partial}{\partial r}\gamma_\perp + \frac{\partial}{\partial r}T_{vB}\right). \tag{2.57}$$

Influence of Laser Pulse Duration

An important aspect for this acceleration is the laser pulse duration, τ_0, compared to w_0/u_i. If $\tau_0 \ll w_0/u_i$, ions located in the laser focal spot do not have enough time to acquire the maximum possible energy, whilst for $\tau_0 \gg w_0/u_i$ these ions have already left the region of interaction long before the laser pulse terminates. Consequently, there is a minimum laser pulse duration for efficient acceleration, which is in (ps) given by

$$\tau_0 \geq \frac{0.1\, w_0}{\sqrt{\gamma_\perp - 1}}, \tag{2.58}$$

when w_0 is expressed in (μm) and the approximation $A \simeq 2Z$ is made, where A is the atomic number of the accelerated ion [43]. For this reason ion acceleration by this so-called Coulomb explosion is not feasible with laser pulse durations of some tens of fs with today's laser parameters, since the energy gain would be low. Assuming the focal waist to be about 10 μm for a normalized laser vector potential of 3, the optimum laser pulse duration should typically be about 1 ps.

Ion Energy Gain

Combining the last two equations a maximum ion energy, U_{max}, attainable from this Coulomb explosion can be derived as

$$U_{max} = Z m_e c^2 (\gamma_\perp - 1). \tag{2.59}$$

Hence, with a normalized laser vector potential of 6 delivered by a laser with a duration of 0.9 ps which is focused down to a waist of 5 μm, a maximum kinetic energy of 3.4 MeV can be obtained for He^{2+} ions [44].

In conclusion, it has been shown that the interaction of a high-intensity laser with an underdense plasma can generate large amplitude electron plasma waves due to such phenomena as FRS, self-modulation of the laser beam envelope and relativistic self-focusing. In the SMLWF regime these waves can break and accelerate background electrons on the laser beam axis. These electron plasma wave oscillations are for ions too rapid since their mass is much larger than the electron mass. However, due to the laser ponderomotive force large space charge fields can be induced in the focal spot, which are capable to accelerate ions radially to the laser axis. This Coulomb explosion

is up to now the only experimentally known ion acceleration process in the underdense regime with short pulse lasers.

It is noted, that the mechanisms for the underdense regime can also occur when such high-intensity lasers are focused onto solid targets. This is due to the technological enigma that such laser impulsions are always headed by a laser prepulse, which can be sufficient to create a preplasma in the target. As plasmas expand into vacuum [13], their electron density can drop underneath the value of the critical density before the main impulsion arrives. In this low density plasma some of the above mentioned mechanisms can occur.

2.3 Overdense Plasma

Obviously, the resonantly amplified generation of a large amplitude electron plasma wave cannot occur in a purely overdense plasma, because the laser beam is prevented from propagating, since $\omega_L < \omega_p$. However, plasma electrons can nevertheless be accelerated in the plasma skin layer by the laser ponderomotive force. This mechanism as well as the secondary and resulting processes for proton acceleration induced by this charge separation will be presented in the following sections.

2.3.1 $\vec{v} \times \vec{B}$ Heating – Electron Beam Generation

For very short and relativistic laser pulses, the ponderomotive force, $\vec{F_p}$, can become very important and the resulting acceleration will tend to push electrons in front of the laser pulse, as a kind of snow-plough effect. This was formerly explained by the influence of the Lorentz force, which is proportional to $\vec{v} \times \vec{B}$. Even though this effect can obviously also occur in the underdense regime it is in the purely overdense regime the main electron acceleration mechanism.

For a short density gradient scale length, $d > \lambda_L$, where $d^{-1} = n_e^{-1} dn_e/dz$, electrons can escape from the laser field in a single optical cycle with a kinetic energy, which is related to the ponderomotive laser potential, U_{max}. In [45] it was suggested that at laser field intensities beyond the relativistic value, $a_0 \geq 1$, such electrons are accelerated to a Boltzmann-like distribution with a temperature, which is of the same order of magnitude as the energy of electron oscillations in the laser field. This is in qualitative agreement with numerical simulations [46]. Hence, this temperature, T_{vB}, is in (MeV) given as

$$\begin{aligned} T_{vB} &= m_e c^2 \left(\sqrt{1 + a_0^2} - 1 \right) \\ &\approx 0.511 \left(\sqrt{1 + \frac{I_{18} \lambda_L^2}{1.37}} - 1 \right), \end{aligned} \tag{2.60}$$

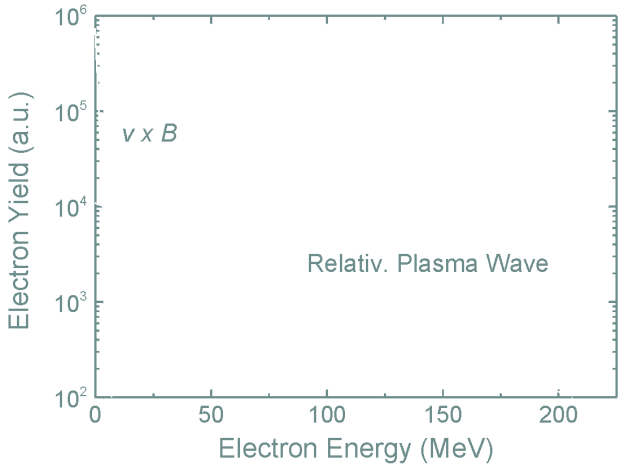

Figure 2.7: Schematic electron spectra for $\vec{v}\times\vec{B}$ electron acceleration and those induced by relativistic plasma waves.

when λ_L is expressed in (μm). Clearly, if a 1 μm laser is focused down to an intensity of 10^{19} W/cm^2 the temperature of this electron distribution is about 1 MeV.

Difference between $\vec{v}\times\vec{B}$ Heating and Acceleration by Relativistic Plasma Waves

As mentioned above, the $\vec{v}\times\vec{B}$ heating process can occur in any kind of plasma as it is simply induced by the ponderomotive laser potential. However, the maximum energy an electron can gain by this process is limited by the maximum laser intensity. Even with those being beyond 10^{19} W/cm^2, only a maximum electron energy of 3 MeV was experimentally obtained since the acceleration length is limited due to the evanescence of the laser to only one optical cycle [47]. In contrast, the electron energy gain by large-amplitude relativistic plasma waves is way more efficient, since the acceleration distance can be much longer, possibly beyond z_R, if it is favored by relativistic self-focusing [7]. As both of these processes can occur simultaneously in the underdense regime, electron spectra obtained here are the superposition of both these mechanisms. This is indicated in Fig. 2.7. In PIC simulations and experiments it was already observed that the $\vec{v}\times\vec{B}$ mechanism leads to a much higher electron yield as well as a larger angular distribution. Since the total number of accelerated electrons can even be of the order of the critical density, this can clearly exceed the low-energy electron yield attainable from wavebreaking [48].

As the laser ponderomotive force pushes electrons out of the laser focal spot this plasma region becomes positively charged shortly after the passage of the laser pulse. This space charge separation as well as the generated electron beam leads to a secondary acceleration process that acts on the remaining positive ions.

2.3.2 Electrostatic Field – Proton Beam Generation

For lucidity the subsequently presented ion acceleration mechanisms by laser plasma interactions will be restricted for protons only, since their acceleration was the aim of the experiments presented here. It is noted that the given formulas also account for any other ion, when the different mass as well as charge are corrected.

In the following, two recently published formalisms will be presented, which describe the mechanisms in which these accelerated protons have their origin

1. at the front surface of the target the laser is focused onto [49], and
2. at the target back surface [50].

The main difference between these two possibilities is that for the front surface mechanism the laser sets up a space charge field, which is induced by the $\vec{v}\times\vec{B}$ heating of electrons. In contrast, proton acceleration from the target back surface is due to the space charge field created by electrons propagating through the target and escaping into vacuum. It is emphasized that both possibilities occur in experiments.

2.3.2.1 Laser Ponderomotive Push

Following [49] it is possible to determine a relation between the laser intensity and the maximum kinetic ion energy, which they obtain at the front target surface. Additionally, the opening cone of this ion beam can also be deciphered.

Ion Energy Gain

A laser pulse incident at a sharp boundary of an overdense plasma exerts on electrons in the skin layer the ponderomotive force, $\vec{F}_p$. This force pushes electrons from their equilibrium positions into the plasma until it is balanced by the electrostatic field, E_s, which is induced due to this charge separation. This field was estimated to be

$$E_s \approx \frac{m_e c\omega_L}{2e}\,\frac{a_0^2}{\sqrt{1+\frac{a_0^2}{2}}}, \tag{2.61}$$

and it is this electrostatic field that accelerates ions into the target. The mean recession velocity of protons, v_r, was in [45] estimated from balancing the momentum flux of the ions with light pressure. In case of total back reflection of the laser beam, v_r is found to be

$$v_r = a_0 c\sqrt{\frac{m_e}{m_p}\frac{n_c}{n_{er}}}, \tag{2.62}$$

where m_p is the proton mass and n_{er} the electron density at the reflection point. If the plasma density is not sharp, but has some gradient induced by the laser prepulse, the laser beam can propagate due to relativistically induced transparency up to

$$n_r \approx n_c \sqrt{1 + \frac{a_0^2}{2}}, \tag{2.63}$$

as it was shown in [51]. At the density of n_r the laser beam starts to push ions forward, and the recession velocity is therefore the greatest here with

$$\left(\frac{v_r}{c}\right)^2 \approx \sqrt{2}\, a_0 \frac{m_e}{m_p}. \tag{2.64}$$

As the most energetic ions are bouncing in the potential well at the plasma boundary they can acquire twice the recession velocity, v_r [52]. Hence, the expected maximum energy of protons accelerated at the front surface of the target is in (MeV) given by

$$\begin{aligned} W_{max}^{front} &\approx 2 m_p v_r^2 \\ &= 2\sqrt{2}\, a_0 \times 0.511. \end{aligned} \tag{2.65}$$

Clearly, using a 250 mJ laser with a 30 fs FWHM pulse length, which is operating at 1 μm wavelength and is focused down onto a 4 μm spot can result in a maximum proton energy of about 7 MeV. Note that this maximum proton energy depends only linearly on the normalized vector potential of the laser and that no assumptions on the target were made.

Opening Cone of Proton Emission

As protons are accelerated down the gradient of the laser intensity, their angular directionality is defined by the particular pattern of the laser intensity distribution at the reflection position of the laser beam. With the assumption of a Gaussian laser beam profile the proton beam opening cone, α, is determined to be

$$\alpha = \frac{\lambda_L}{w_0}, \tag{2.66}$$

which is for a 1 μm laser focused down onto a 6 μm spot about 10°. However, in PIC simulations it was observed that this cone can be significantly increased due to filamentory instabilities of the laser beam in the preplasma [49].

Obviously, this laser ponderomotive push makes no assumptions on target properties, like material or thickness. However, this is in contradiction with experiments,

where such dependencies were observed. Hence, two different mechanisms have been proposed to explain these results. The first explanation is that protons are accelerated at the front surface and propagate through the target [8]. The second explanation is based on proton acceleration on the rear target surface [53]. In this case, electrons are heated by the laser at the front surface of the target and propagate through the solid material forming a space charge cloud in vacuum at the rear surface. This quasi-static electric field is in turn strong enough to ionize the material and accelerate protons perpendicularly to the rear surface as it will be shown in the next section.

2.3.2.2 Electrostatic Acceleration

In the following the published formalism in [50] will be presented, which correlates the maximum proton kinetic energy with the temperature of the accelerated electrons. Here it is assumed that at a time $t = 0$ the plasma occupies the half-space $z < 0$, protons are initially at rest with density $n_p = n_{p0}$ for $z < 0$ and $n_p = 0$ for $z > 0$. The boundary at $z = 0$ is supposed to be sharp.

Self-Similar Model

The electrostatic acceleration of protons is induced by the expansion of electrons into vacuum at the rear target surface. Electrons escaping a sharp boundary plasma slab with initially immobile protons are assumed to have a Boltzmann-like distribution

$$n_{em} = n_e \exp\left(\frac{e\Phi}{k_B T_e}\right), \tag{2.67}$$

where k_B is the Boltzmann constant and Φ the electrostatic potential. This electrostatic potential satisfies the Poisson equation

$$\frac{\partial^2 \Phi}{\partial z^2} = \frac{e}{\epsilon_0}(n_e - n_p). \tag{2.68}$$

In [54] a simple expression of the electrostatic field, E_b, at the boundary of the plasma to vacuum was found by integrating this Poisson equation from the plasma boundary to infinity as

$$E_b = \sqrt{\frac{2 n_e k_B T_e}{e\epsilon_0}}. \tag{2.69}$$

Assuming that electrons stay in equilibrium with Φ, proton expansion into vacuum is then described by the equations of continuity and motion

$$\left(\frac{\partial}{\partial t}+u_p\frac{\partial}{\partial z}\right)n_p = -n_p\frac{\partial u_p}{\partial z} \tag{2.70}$$

$$\left(\frac{\partial}{\partial t}+u_p\frac{\partial}{\partial z}\right)u_p = -\frac{e}{m_p}\frac{\partial \Phi}{\partial z}, \tag{2.71}$$

when u_p is the proton velocity. For $z + c_s t > 0$ a self-similar expansion can be found if quasineutrality in the expanding plasma is assumed, i.e. $n_{em} = n_p = n_e \exp(-z/c_s t - 1)$, $u_p = c_s + z/t$ and

$$E_{ss} = \frac{k_B T_e}{e c_s t} = \sqrt{\frac{n_e k_B T_e}{\epsilon_0}}\frac{1}{\omega_{pi} t}. \tag{2.72}$$

This self-similar field corresponds to a positive charge surface, $\sigma = \epsilon_o E_{ss}$, at position $z = -c_s t$ and a negative charge surface, $-\sigma$, at the plasma edge.

However, this self-similar solution holds only for $\omega_{pi} t < 1$, which is the case when the initial Debye length, $\lambda_D = \sqrt{\epsilon_0 k_B T_e / n_e e^2}$, is greater than the self-similar density scale length, $c_s t$. In case $\omega_{pi} t \gg 1$, this model predicts an infinitely increasing proton velocity for $z \to \infty$. But physically u_p is limited to a finite value.

Ion Front Modelling

In [50] a Lagrangian code was developed to solve Eq. 2.67 - 2.71 and to overcome the above mentioned difficulties. Here, in contrast, Eq. 2.68 was integrated from the actual position of the proton front to infinity, which leads to the electrostatic field

$$E_{estat} = \sqrt{\frac{2 n_e k_B T_e}{\epsilon_0}} \exp\left(\frac{e\Phi_{estat}}{2 k_B T_e}\right). \tag{2.73}$$

Subsequently, the accelerating field at the proton front, E_{pf}, can be expressed as

$$E_{pf} \simeq \sqrt{\frac{2 n_e k_B T_e}{\epsilon_0 e (1+\tau^2)}}, \tag{2.74}$$

where $\tau = \omega_{pi} t / \sqrt{2e}$. Self-explanatory it is possible to determine from this equation a proton velocity, v_{pf}, by integration of $dv_{pf}/dt = eE_{pf}/m_p$. Its solution has the asymptotic limit

$$v_{pf} \simeq 2 c_s \ln(2\tau) = c_s[2\ln(\omega_{pi} t) + \ln 2 - 1]. \tag{2.75}$$

Interestingly, this expression delivers a cut-off energy, E_{pf}^{max}, for accelerated protons for the case $\omega_{pi} t \gg 1$, which is given by

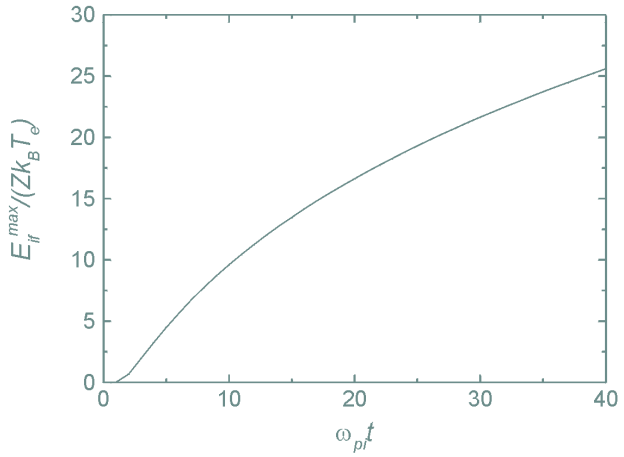

Figure 2.8: Proton cut-off energy from plasma expansion into vacuum.

$$E_{pf}^{max} \simeq 2Zk_BT_e[\ln(2\tau)]^2, \tag{2.76}$$

and shown in Fig. 2.8. Obviously, the proton energy increases the higher T_e and τ.

Note that the aforementioned models are simplified since several possible impacts were neglected : Non-Maxwellian electron distributions [55], 2D as well as 3D effects [56], magnetic field effects [49], etc.. As their contributions compound the processes no simple and intuitive expressions can be given. Nevertheless, their impact is usually implemented in numerical PIC code models.

2.3.2.3 Experimental Controversies

It is noted that there are some controversies about the origin of the high energy protons. Results obtained from experiments in [8, 57] provide evidence that the observed protons were generated and accelerated in the front surface of the plasma, which is conflicting with experiments that indicate proton acceleration from the rear surface [53, 58]. Additionally, there is also a disagreement on the hot electron penetration in solid targets. In [59] the penetration depth of hot electrons differed significantly from [60], which might explain the controversies in proton generation and acceleration. However both aforementioned situations seem to be simultaneously possible whereas the modelling of such interactions is compounded by some important aspects : First, it is difficult to precisely correlate the temperature of an electron beam propagating through a target with the initial laser intensity. Second, from an experimental point of view the exact laser parameters, particularly the contrast ratio are not known for every single laser pulse. Obviously this changes the properties of the solid target and modifies the penetration of the generated electron beam. As such laser parameters are different for any laser system, apparently different results will be obtained.

Part II

Neutrons as a Diagnostic for Plasma Ion Temperature

Chapter 3

Methodological Basics

In this chapter essential parameters for neutron generation by the interaction of a high-intensity laser with a deuterium gas jet will be discussed. Starting with a brief review on the implications of neutron generation and previously conducted work, it will be shown that measuring the $D(d,n)^3He$ fusion neutron energy as a function of the angular emission can reveal information on the underlying deuteron spectra and directionality. Therefore the differences in neutron generation by $D(d,n)^3He$ reactions between the beam target model and a thermonuclear source will be regarded in detail. As a result this method can diagnose ion heating processes occurring during relativistic laser plasma interactions.

3.1 Implications of Fusion Neutron Generation

As was shown in the previous chapter, relativistic laser plasma interactions can create free ions. In the case that they escape the plasma, their measurement is straightforward and can simply be done with external particle detectors. But in order to have a deeper insight into the entire energy transfer occurring during such interactions, those ions remaining inside the plasma need to be experimentally characterized as well. To do so, one capitalizes on their nuclear reactions as a diagnostic, particularly on the generation of free neutrons.

These neutrons can be produced by nuclear fusion reactions of light particles, such as deuterium or tritium ions. Interestingly, fusion reactions are not limited by an energy threshold and the energy transfer to neutrons is on the order of some MeV as this is determined by the mass difference of all reactants. Since the cross sections and kinematics of such fusion reactions are well understood [22], the characterization of the yield and the spectra of these neutrons allows do draw conclusions on the initial ions. Consequently, fusion neutron spectra can be used to visualize low energy ion kinematics inside plasmas.

Such an implication of neutrons, whose basic parameters and general energy discrimination are given in Table 3.1, has also several other important advantages. As a function of their energy, neutrons interact with matter by absorption or scattering, whereas for low neutron energies in the eV range the cross section for absorption is

Table 3.1: Basic neutron parameters and energy discrimination.

Mass	m_n	939.57			($\mathrm{MeV/c^2}$)
Half-life	$T_{1/2}$	10.2			(min)
Charge	q	$< 4 \cdot 10^{-22}$			(e)
Thermal	T_n	1	meV	-	500 meV
Epithermal	T_n	500	meV	-	500 keV
Fast	T_n	$>$ 500	keV		

predominant. For higher energies absorption becomes negligible, whilst the probability for neutron scattering increases [61]. As neutrons are electrically neutral particles, this scattering is solely a function of the mass and the density of their partners and fast neutrons can traverse dense matter without severe deflection. This is of particular importance when they propagate through plasmas, where huge electric and magnetic fields can be evoked. Due to their neutrality, neutrons are not severely influenced by this medium as any charged particle would be.

Distinction between fusion neutrons and those generated by other processes is possible due to their differing spectra. It is known, that free neutrons can also be generated by fission, when energetic electrons or γ-rays deliver an energy beyond the neutron spallation energy, S_n, to a nucleus to induce $(e, e'n)$ and (γ, n) reactions. Here, the kinetic energy of the expelled neutron is simply the difference between the energy of the incident electron or γ-ray, S_n and the energy of the remaining nucleus. In contrast, the emission spectrum of fusion neutrons is centered at its nuclear energy release value with a shift according to the net center of mass motion of the initial ions.

3.2 Previous Work and Motivation

The main fusion reaction that has been studied is $\mathrm{D}(d, n)^3\mathrm{He}$ due to its relatively high cross section and the availability of deuterium at solid and near-solid densities in the form of deuterated plastics and clusters. In the following, only this reaction will be considered since in the manuscript presented here, the experiment was performed with a deuterium gas target.

In [62] a 200 mJ, 160 fs Ti:Sa laser was focused to a peak intensity of 10^{18} $\mathrm{W/cm^2}$ onto a solid, deuterated polyethylene target. Due to the prepulse of the laser a preplasma was formed ahead of the main impulsion. The neutron emission was measured perpendicularly to the target normal, where a maximum yield of 140 neutrons per

shot was found once the laser was focused slightly in front of the original solid surface. No neutrons were detected without this prepulse, indicating that fusion neutrons were generated by the Coulomb explosion radially expelled deuterons as the laser beam propagated through the underdense plasma.
Neutron emission from thick, deuterated plastic targets without an extensive preplasma has been reported in [63], where 1.3 ps Nd:Glass laser pulses were focused to intensities approaching 10^{19} W/cm^2. The isotropic yield of 10^7 neutrons was concluded to only be possible due to the interaction of a deuteron beam, which was generated by this interaction and which entered the target with an energy of up to 100 keV.
Neutron angular distribution measurements are presented in [64] where a 400 fs, 0.529 μm wavelength laser pulse was also focused onto thick deuterated targets with peak intensities of $(2-3.5)\times 10^{19}$ W/cm^2. Up to 10^7 neutrons were detected with an anisotropic emission profile, which suggested deuteron beams entering the target with energies of at least 550 keV.
Neutrons produced by interactions of a 100 mJ, 32 fs Ti:Sa laser with large deuterium clusters has been observed in [65]. The production of over 10^4 neutrons per shot was determined, as well as a one order of magnitude increase in neutron yield, when the laser intensity was increased by a factor of three. In [66] a 800 mJ, 35 fs Ti:Sa laser was focused to intensities of several 10^{17} W/cm^2 onto deuterated methane clusters. Ions expelled by the Coulomb explosion were measured with a Thompson parabola and it was understood that the generation of up to 10^4 neutrons per shot does not only occur in the hot plasma core, but also in the cold outer regions by collision processes.

Obviously, D$(d,n)^3$He fusion neutrons have been studied over a wide range of intensities and for targets at solid or near-solid densities. It was shown that a precise characterization of the emitted neutrons can give insight into ion heating mechanisms. In contrast, the study of ion dynamics in the interaction of intense lasers with underdense plasmas has received less attention, even though such interactions can produce energetic deuterons by two processes :

1. Coulomb explosion.

2. Possible thermonuclear ion heating within in the plasma core.

Therefore it is the aim of the here presented experiment to quantify these possibilities with D$(d,n)^3$He reactions occurring during the interaction of a high-intensity laser with an underdense plasma in a deuterium gas jet.

3.3 D$(d,n)^3$He Reaction

The D$(d,n)^3$He reaction has a nuclear energy release, Q, of 3.27 MeV in the center of mass system. Due to the conservation of energy, this energy is divided inversely proportional to the masses of the emitted neutron and the generated ^{3}He nucleus. Thus, the neutron gains 2.45 MeV and the helium nucleus 0.82 MeV.

The kinematics and the cross sections of this reaction will in the following be presented in the laboratory as well as the center of mass system. In the laboratory system at least one deuteron is assumed to be stationary. This allows to define a geometry and represents the case when a beam of deuterons propagates through a deuterated target. In contrast, Maxwellian ion distributions are usually found for thermonuclear sources in a plasma. Here it is convenient to perform these calculations in the center of mass system by regarding single ion velocity distributions as a whole and as a function of their temperature.

3.3.1 Kinematics

3.3.1.1 Beam Target Model

The geometry for the D$(d,n)^3$He reaction in the laboratory system is defined in Fig. 3.1. Here it is indicated that the neutron can be emitted with discrete energies at different angles, α, which is simply due to the conservation of energy and momentum. In the non relativistic case the total energy of this reaction is conserved as

$$T_{tot} = T_d + Q = m_d \frac{v_d^2}{2} + Q = m_n \frac{v_n^2}{2} + m_{He} \frac{v_{He}^2}{2}, \tag{3.1}$$

where m_d, v_d, m_{He} and v_{He} are the masses and velocities of the incident deuteron and the ^{3}He nucleus respectively. The conservation of momentum of this reaction is

$$\overrightarrow{p}_n + \overrightarrow{p}_{He} = \overrightarrow{p}_d. \tag{3.2}$$

With these two equations it can be shown [61] that the neutron energy varies with the angle of neutron emission relative to the direction of the incident deuteron as

Figure 3.1: Definition of geometry for D$(d,n)^3$He reaction in the laboratory system, where one deuteron energy, T_D, is zero. The angle of the neutron emission, α, is determined by the conservation of momentum.

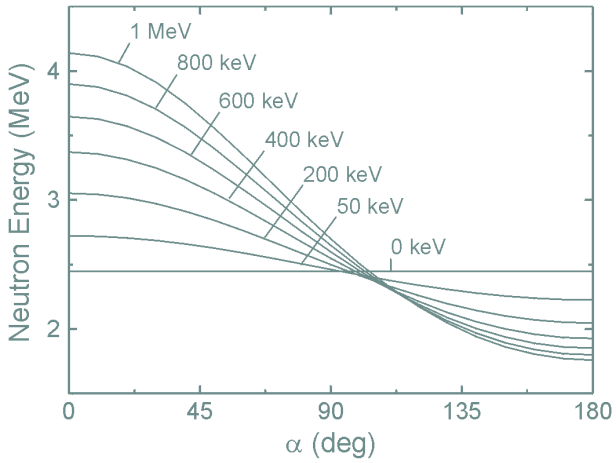

Figure 3.2: Neutron energy as function of angular emission for different deuteron energies inducing $D(d,n)^3He$ reactions.

$$T_n(\alpha) = T_d \frac{m_d\, m_n}{(m_n + m_{He})^2} \left\{ 2\cos^2\alpha + \frac{m_{He}(m_{He}+m_n)}{m_d\, m_n} \left[\frac{Q}{T_d} + \left(1 - \frac{m_d}{m_{He}}\right)\right] + \right.$$
$$\left. + 2\cos\alpha \sqrt{\cos^2\alpha + \frac{m_{He}(m_{He}+m_n)}{m_d\, m_n} \left[\frac{Q}{T_d} + \left(1 - \frac{m_d}{m_{He}}\right)\right]} \right\}. \qquad (3.3)$$

Figure 3.2 shows the calculated neutron energy as a function of emission angle for different deuteron energies. Clearly, a beam of deuterons penetrating a stationary

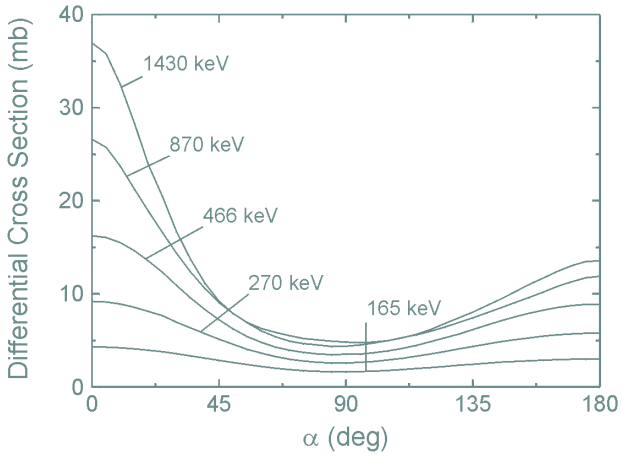

Figure 3.3: Laboratory differential cross section for different deuteron energies inducing $D(d,n)^3He$ reactions.

deuterated target leads to a varying neutron energy as a function of its angle of emission. Data shown in Fig. 3.3 indicate, that the neutron emission for $D(d,n)^3He$ is more likely to occur on the axis of incidence of the incoming deuteron [67]. Obviously, the energy of the reacting deuteron can then be determined by measuring the energy of the generated neutron as a function of α.

3.3.1.2 Thermonuclear Source

In the center of mass system of two reacting deuterons the conservation of momentum is zero

$$m_n \overrightarrow{u}_n + m_{He} \overrightarrow{u}_{He} = 0, \tag{3.4}$$

when $\overrightarrow{u}$ represents the particle velocity. Therefore, the conservation of energy of this nuclear reaction is found to be

$$Q + K = m_n \frac{u_n^2}{2} + m_{He} \frac{u_{He}^2}{2} = \frac{1}{2} \left(\frac{m_n}{m_{He}} \right) (m_n + m_{He}) u_n^2, \tag{3.5}$$

where K is the relative kinetic energy of the reacting deuterons. In the laboratory system, the center of mass has the velocity $\overrightarrow{V}$ and the neutron velocity is thus $\overrightarrow{v}_n = \overrightarrow{V} + \overrightarrow{u}_n$. Providing an isotropic deuteron distribution, the mean energy of the generated neutron, $\langle T_n \rangle$, can so be given as

$$\langle T_n \rangle = \frac{m_n}{2} \langle V^2 \rangle + \frac{m_{He}}{m_n + m_{He}} \left(Q + \langle K \rangle \right), \tag{3.6}$$

since the integration over the random angle, ζ, between $\overrightarrow{V}$ and $\overrightarrow{u}_n$ vanishes. Consequently, the neutron energy spectrum is independent of the angle of detection [68]. Assuming Q to be much in excess of these mean temperatures, the displacement in energy of the generated neutron becomes

$$T_n - \langle T_n \rangle = \sqrt{\frac{2\, m_{He}\, m_n}{m_{He} + m_n}\, Q}\; V \cos\zeta. \tag{3.7}$$

Since $V \cos\zeta$ represents the component of $\overrightarrow{V}$ in the direction of $\overrightarrow{u}_n$, the distribution of $T_n - \langle T_n \rangle$ reflects the distribution of $\overrightarrow{V}$ in one dimension. It can then be shown that this neutron energy distribution corresponds to a Gaussian distribution

$$f(T_n)\, dT_n = dT_n \exp\left[-2\, m_d \left(T_n - \langle T_n \rangle \right)^2 \left(\frac{4\, m_n\, m_{He}}{m_n + m_{He}}\, Q\, T \right)^{-1} \right], \tag{3.8}$$

where T is the temperature of the Maxwellian deuteron distribution [69]. Thus, the standard deviation of the energy spectrum of the expelled neutrons reflects the initially unknown deuteron temperature.

3.3.2 Cross Sections and Neutron Yield

Integration over the known differential cross section, $\sigma(T_d, \alpha)$, of the D$(d,n)^3$He reaction, a given deuteron density and the deuteron energy spectrum, dN_d/dT_n, determines the number of generated neutrons for a certain angle of emission. However, in the experiment presented here the underlying deuteron spectrum is unknown. Instead, it will be shown that the measured neutron yield as a function of the angle of detection can also be used to decipher the energy as well as the number of the initial deuterons, which accounts for the beam target model as well as thermonuclear sources.

3.3.2.1 Beam Target Model

Cross sections for D$(d,n)^3$He reactions are well known from nuclear physics [22]. As can be seen in Fig. 3.4, the probability for a D$(d,n)^3$He reaction to occur increases with the kinetic energy of the incident deuteron. Thus the number of neutrons, N_n, a Maxwellian beam of deuterons entering a stationary target with a given deuteron density, n_D, is given by

$$N_n(T_d, \alpha) = n_D \int_0^{\infty} \frac{dN_d}{dT_d}\, dT_d \int_0^{T_d} \frac{\sigma(T_d, \alpha)}{\varepsilon(T_d)}\, dT, \tag{3.9}$$

where $\varepsilon(T_d)$ is the stopping cross section for deuterons per atom of deuterium. Consequently, a known neutron yield as a function of angular emission can provide the number of incident deuterons by reversing Eq. 3.9.

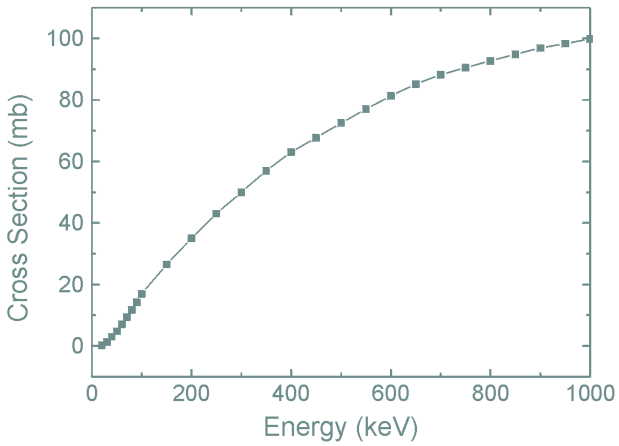

Figure 3.4: Cross section for D$(d,n)^3$He reaction in the laboratory system.

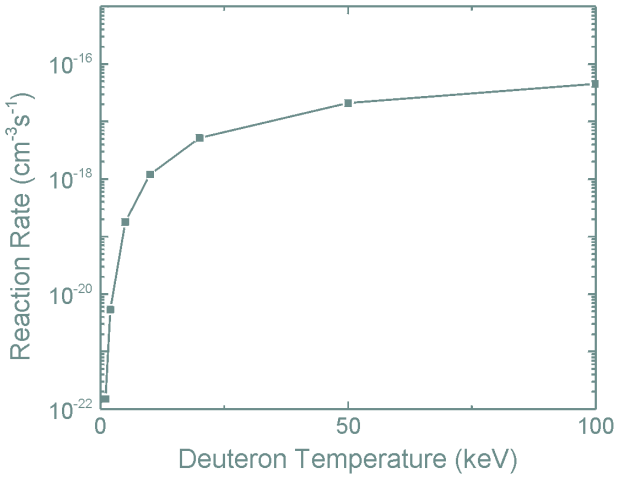

Figure 3.5: Reaction rates, $\langle \sigma v \rangle$, for D$(d,n)^3$He fusion of Maxwellian distributions.

3.3.2.2 Thermonuclear Source

For Maxwellian deuteron distributions it is convenient to evaluate a mean reaction rate, $\langle \sigma v \rangle$, by folding the laboratory system cross section into the deuteron velocity distribution, which has a certain temperature, T. As can be seen in Fig. 3.5, this reaction rate increases dramatically the higher the deuteron temperature. Assuming that V is the volume of such a plasma, τ its confinement time and n_d the number of reactants, the attainable neutron yield is

$$N_n = \frac{1}{2} \langle \sigma v \rangle \, n_d^2 \, V \, \tau, \tag{3.10}$$

where the factor $\frac{1}{2}$ corrects for counting all reacting deuterons twice.

3.4 Summary and Discussion

In this chapter it has been shown, that measurements of neutrons generated by D$(d,n)^3$He reactions can be used to visualize deuteron energies within a thermonuclear plasma. However, these reactions can also be induced within the stationary and ambient gas jet by deuterons accelerated by the Coulomb explosion. Nevertheless, these two possibilities differ significantly. For the beam target model, where by the Coulomb explosion radially expelled deuterons propagate through the ambient gas jet the energy and the yield of the generated neutrons changes with the angle of detection. This is due to the conversation of energy as well as momentum and the implying cross sections. In the case of a thermonuclear source this dependence will clearly not occur, since any reaction geometry has the same probability. Furthermore, if the measured neutrons

could be identified to be thermonuclear it would be possible to determine the plasma ion temperature from the neutron energy spectrum.

The potential advantage of basing a temperature on such an energy spectrum width rather than an absolute measurement of the total neutron yield removes the necessity for absolute calibration of the used detectors. Uncertainties arising from deuteron densities are removed and performing such a measurement over all angles of emission can clearly stress the obtained results since the kinematics and cross sections of the $D(d,n)^3He$ reaction are known. However, to obtain such a neutron spectrum, detectors are required that have a sufficient temporal resolution since the neutron shift will be located slightly around 2.45 MeV for low deuteron energies. These detectors have to be specially designed in order to prevent measurement of scattered neutrons or those generated elsewhere. Special attention has to be paid to a precise measurement of the neutron yield, as the thermonuclear reaction rate depends greatly on the temperature of the initial deuteron distribution. Clearly, this also provides difficulties with non-Maxwellian spectra, since the $D(d,n)^3He$ cross section shows a great dependence with deuteron energy.

To decipher these two possibilities the generated deuterons and neutrons have to be precisely characterized, such as the plasma density in this interaction. How these requirements were met in the experiment will be described in the next chapter.

Chapter 4

Experimental Set-up

This chapter describes the set-up of the experiment performed on the VULCAN laser system, in Target Area West of the Central Laser Facility at the Rutherford Appleton Laboratory. By way of introduction the laser and its parameters will be described. This will be concluded by the detailed discussion of the set-up used and the detectors, starting with the deuterium gas jet and its density profile, which was surveyed with optical diagnostics in order to obtain the plasma density. Subsequently, the implemented Thomson parabola, CR-39 nuclear track detector and radiochromic film will be presented, from which the spectrum, yield and angular distribution of the generated deuterons were obtained. The same information was acquired for by $D(d,n)^3He$ reactions generated neutrons. The Time-of-Flight and activation detectors for these neutrons will be stressed in particular, since they revealed information on ion heating processes during this interaction.

4.1 VULCAN Laser System

VULCAN is an infrared Neodymium Glass (Nd:Glass) laser and based on a standard implementation of the Chirped Pulse Amplification (CPA) scheme already well known to the scientific community [70]. It is capable of generating 100 TW laser pulses with a pulse duration of less than a picosecond [71]. An overall schematic of this laser chain is given in Fig. 4.1.

The system starts with a Titanium doped Sapphire (Ti:Sa) oscillator. A pulse picker selects single laser pulses, which are injected into double-passed rod amplifiers, where each holds a Nd:Glass rod of different diameter. These are surrounded by flash-lamps and highly polished ceramic reflectors. The largest amplifiers are cooled after each laser shot using filtered air blowers, which limits the repetition rate of VULCAN to one shot every 20 minutes. Pockels cells change the polarization of the laser beam, which, by additional timing of its birefringent crystal enables to use them as switches. Reflections are thus prevented from travelling back through the entire laser system and due to the timing, the pulse is cleaned temporally in the order of nanoseconds. Faraday isolators (FI's) change the polarization of the laser beam in between any amplification stage, also preventing beams from travelling in the opposite direction.

Figure 4.1: Schematic of the VULCAN Nd:Glass laser chain configured for CPA operations. The single components are briefly described in the text.

Table 4.1: VULCAN laser parameters for described experiment.

Laser Wavelength	λ_L		1054 nm
Energy on Target	E_L	$\leq$	62 J
Pulse Length	τ_0		0.8 - 1 ps
Repetition Rate			20 min
Waist of Focal Spot	w_0		20 μm
Peak Laser Intensity	I_L	$\leq$	2×10^{19} W/cm^2
Contrast Ratio		$\geq$	1×10^6

Air Spatial Filters (ASF's) and Vacuum Spatial Filters (VSF's) consist of two lenses and a pinhole in order to eliminate off-axis parts of the laser beam and reduce high spatial frequency growth. In any of these filters the beam is spatially expanded in order to avoid optical damage to the amplifiers and any other components. This was the main limitation for high-intensity lasers some decades ago and was finally overcome by the CPA scheme. This involves stretching of the pulse using a dispersive medium, i.e., anti-parallel reflection gratings, which change the pulse duration and consequently the power of the laser by some orders of magnitude. Finally and after all amplification stages, the pulse is re-compressed to its original length using a second set of gratings. This recompression, which for a single pass is only about 50 % efficient, must be done under vacuum in order to prevent serious degradation of the compressed beam by self modulation, principally in the window of the evacuated target chamber.

For the described experiment, this laser beam was focused down to a focal spot with a waist, w_0, of 20 μm using a $f/4$ off-axis parabolic mirror. The energy of each amplified laser pulse was measured by leaking a defined fraction of the pulse from a final turning mirror into a calorimeter. Its pulse duration was obtained using a single shot autocorrelator and was found to increase slightly with laser energy. Those two measurements were routinely performed on every laser shot. Table 4.1 gives the typical laser parameters during this experiment.

4.2 Diagnostics

The target chamber indicated in Fig. 4.1 was in fact separated from the laser system and located in Target Area West. The overall layout of the set-up in this experimental hall is shown in Fig. 4.2 and will be discussed in detail in the following sections.

Figure 4.2: Experimental set-up at Target Area West. The laser beam was focused with an off-axis parabolic mirror *(a)* onto the edge of a D_2 gas jet *(b)*. The transmitted beam was analyzed with an optical spectrometer and a CCD camera *(c)*. From the gas jet radially expelled ions were detected with a Thomson parabola, CR-39 nuclear track detectors *(d)* and radiochromic film *(e)*. Neutrons were measured with plastic scintillators and PMT's, which were shielded with tapered collimators made out of polyethylene and lead *(f)*. These detectors were installed at different angles, θ, in the horizontal (x, z) plane. Details and comprehensive discussions are given in the text.

4.2.1 Gas Jet and Optical Diagnostics

The laser was focused onto the edge of a D_2 gas jet produced by a 1 mm diameter sonic nozzle, which was located 1 mm below the focus. Interferometric studies were used to characterize the atomic density profile [72]. By changing the backing pressure, the electron plasma density, n_e, was selected to be in the range 1×10^{19} to 1×10^{20} cm^{-3}, which was verified on each shot by FRS measurements. For this, the transmitted laser light was collected and imaged onto the slit of an optical spectrometer. The spectra were recorded with a 16-bit Charged-Coupled-Device (CCD) camera, which was shielded in order to eliminate measurements of scattered light or light generated elsewhere in the experimental hall.

In chapter 1.2.1 FRS was introduced as the decay of the laser light into two forward moving electromagnetic side-bands at frequencies $\omega_L - \omega_p$ (Stokes wave) and $\omega_L + \omega_p$ (anti-Stokes wave). Obviously, the electron plasma density can then be derived from the separation of these lines by the Bohm-Gross frequency shift [73]-[76] as

$$n_e = \sqrt{\frac{\omega_p^2 \, \varepsilon_0 \, m_e}{e^2}} = n_c \sqrt{\frac{\triangle\omega - \omega_L}{\omega_L}}, \tag{4.1}$$

where absolute value of either the Stokes or the anti-Stokes wave can be used for $\triangle\omega$.

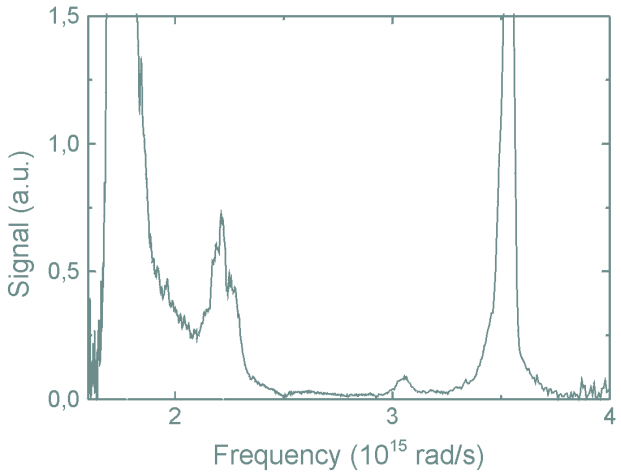

Figure 4.3: Forward Raman Scattering of transmitted laser beam. The separation of the laser beam, ω_L, and the anti-Stokes wave, ω_+, reveals the plasma electron density to be 5.5×10^{19} cm^{-3}. The peaks at higher frequencies are the second harmonic and its satellite.

For the intensities used in this experiment and for sufficiently underdense plasmas it is found that the laser is highly susceptible to FRS. Measurements of FRS were performed for every single laser shot. Figure 4.3 shows a typical example of such a measurement, demonstrating n_e to be 5.5×10^{19} cm^{-3}.

4.2.2 Deuteron Detectors

Deuterons expelled by the Coulomb explosion during this interaction were measured using a Thomson parabola and CR-39 nuclear track detectors [77]. These were installed at 90° on the x-axis, 40 cm away from the nozzle. This position is indicated in Fig. 4.2, which also defines the geometry described below.

4.2.2.1 Thomson Parabola

The spectrometer used consists of a permanent magnet with an uniform field, $|\overrightarrow{B}|$, of 0.1 T and a parallel and adjustable electric field, $|\overrightarrow{E}|$, of up to 4×10^5 V/m. Ions could enter the device through a 250 μm diameter pinhole in a 1 mm thick lead plate, which resulted in a solid angle of 3×10^{-7} srad. This lead plate stopps all deuterons below an energy of 11 MeV.

Due to their charge to mass ratio, Z/A, these ions get independently deflected due to the Lorentz Force. Consequently, they describe on the detector plane at a distance L in (m) behind the spectrometer for their species unique parabolic curves given by

$$y^2 = \frac{B^2\, Ze\, l}{A\, m_i\, E}\left(\frac{1}{2} + L\right) z, \tag{4.2}$$

where m_i is the mass of the ion in (kg) and l the length in (m) over which the magnetic and electric field extend. The accelerated ion, its speed and accordingly its energy can be identified by measuring the deflection on the detector plane with a suitable detector. The energy resolution of this device depends on the drift distance, L, from the Thomson parabola to the detector.

4.2.2.2 CR-39 Nuclear Track Detector

Here, CR-39 nuclear track detectors have been used, which are sensitive to ions with an energy above 100 keV per nucleon. Ions penetrating CR-39 deposit their energy in this material as a function of its stopping power, which results in the production of secondary electrons. This energy deposition can cause damage by breaking bonds in the material structure. Due to the dominant and particularly well defined Bragg Peak, which occurs once the ion comes to rest in matter, this energy deposition is highly localized where the ion stops in the CR-39. Contrarily, electrons and γ-rays deposit their energy more homogenously over all their entire range, which makes CR-39 relatively insensitive to them.

Taking advantage of this unique energy deposition, an ion creates a pit in this detector, and the sampled number of all these pits corresponds to the number of detected ions. To obtain this yield, the pits are visualized, i.e. enlarged by etching the detector in a 20 % concentrated sodium hydroxide solution for 3 hours at 90° C and counted afterwards using a microscope. The resolution which can be obtained with this arrangement depends mainly on the flux of protons and the drift distance, L, the detector was placed behind the Thomson parabola. Since one proton creates one pit, single ions with an energy above the detection threshold can be detected. Though the diameter of approximately 10 μm of each etched pit in the CR-39 sets the limit for the energy resolution and the maximum number of deuterons that can be detected.

4.2.2.3 Radiochromic Film

The Thomson parabola gives only information about the energy and yield of the deuterons entering the device through its pinhole. However, the opening cone of by the Coulomb explosion expelled ions is larger than this limiting solid angle [44]. In order to know about the angular distribution and therefore the entire deuteron yield, additional measurements with radiochromic film [78] of the type MD55 have been performed. This film was installed opposing the Thomson Parabola, e.g. at an angle, θ, of $-90°$ according to Fig. 4.2, in order to have simultaneous information with both diagnostics.

MD55 radiochromic film is a transparent nylon substrate coated in an organic dye, which is 260 μm thick and continuously distributed through the substrate [79]. It is sensitive to the dose delivered by all ionizing radiation and undergoes a color change, which is a function of the exposing dose. MD55 is analyzed by measuring its optical density before and after exposure using a Microdensitometer, where a spatial resolving power of greater than 1200 lines per mm is attainable. In [80] it was deciphered, that Ψ, the number of deuterons per (cm^2), is then given as

$$\Psi = 8.1 \times 10^7 \, D, \tag{4.3}$$

where D is the measured dose of the film in (Gy). However, the interpretation of radiochromic film must be done carefully, since it is also sensitive to electrons, γ-rays, protons and any other ionizing radiation.

4.2.3 Neutron Detectors

Neutrons generated during this experiment were measured with two different approaches. Their energy and the angular distribution were determined using the Time-of-Flight technique [67], whilst their entire yield was obtained by separate nuclear activation measurements.

4.2.3.1 Time-of-Flight Measurements

With the Time-of-Flight (TOF) technique the neutron energy is determined by measuring its velocity, i.e. the time, t, it needs to travel a known distance, s, towards a detector. These detectors were 5 cm diameter cylindrical NE102a scintillators with different thicknesses between 1 and 4 cm, which were coupled with optical grease to the windows of Philips photomultiplier tubes (PMT's) [81], whose electrical output was recorded on oscilloscopes. As indicated in Fig. 4.2, up to five of these detectors were used simultaneously at various distances from 1.9 to 5.5 m from the gas jet nozzle and at angles, θ, of 0 to 180° relative to the direction of propagation of the laser beam. They were calibrated relative to one another by swapping their position for different shots under the same conditions. To suppress background signals due to bremsstrahlung, scattered neutrons and those generated elsewhere by (γ, n) or $(e, e'n)$ reactions, tapered collimators pointing directly towards the interaction region were used. These were up to 53 cm long and more than 10 cm thick and consisted of polyethylene and lead, which was sufficient to suppress any serious signals to below noise level.

The kinetic energy, T_n, of the detected neutron can be calculated as

$$T_n = (\gamma - 1)\, m_n c^2 \approx \frac{1}{2}\, m_n c^2\, \beta_n^2 \left(1 + \frac{3}{4}\beta_n^2\right), \tag{4.4}$$

where their normalized velocity, β_n, can be determined from the measured flight time, t, and the known flight path, s. The depart of the time measurement was taken to be the prompt signal of the γ-flash due to bremsstrahlung generated by relativistic electrons that are produced during this interaction. The flight path was estimated to be the distance between the center of the gas jet nozzle and the center of the scintillator. The attainable energy resolution, $\triangle T_n$, is a function of the relative time resolution, $\triangle t/t$, and the uncertainty of the flight path, $\triangle s/s$, and is given as

$$\frac{\triangle T_n}{T_n} \approx 2\sqrt{\left(\frac{\triangle t}{t}\right)^2 + \left(\frac{\triangle s}{s}\right)^2}. \tag{4.5}$$

Neutrons are indirectly identified within these NE102a plastic scintillators due to their scattering with hydrogen and carbon ions, which causes their ionization. Additionally, this detector is also sensitive to γ-rays interacting with the scintillator via the Compton effect, which generates free electrons. These charged particles excite the scintillator, which results in the emission of light, i.e. a scintillation. This scintillation occurs with a fast rise time of 1.5 ns and a high light output for NE102a. However, its decay is influenced by the so-called afterglow of this material, when the scintillator still emits light after the charged particle has already gone. This effect can be described as the convolution of a Gaussian with an exponential

$$N(t) = N_0 f(\sigma, t)\, \exp\left(\frac{-t}{\tau}\right), \tag{4.6}$$

where $f(\sigma, t)$ is a Gaussian with a standard deviation σ of 0.7 ns, τ the decay constant of 2.4 ns and N_0 the total number of photons emitted [82]. The Tektronix oscilloscopes used had a sampling rate of 500 ps [83]. With this experimental set-up, and taking into account the sampling rate of the oscilloscope as well as the afterglow of the scintillator it was therefore possible to achieve a typical energy resolution for $\mathrm{D}(d,n)^3\mathrm{He}$ fusion neutrons of around 2 %.

4.2.3.2 Nuclear Activation

To ensure that the signal obtained by the PMT's is indeed due to neutrons and not a random artefact or noise signal, the nuclear activation of ^{115}In was carried out. The process

$$^{115}\mathrm{In} + \mathrm{n} \rightarrow {}^{116}\mathrm{In}^* \rightarrow {}^{116}\mathrm{Sn} + e^- + \overline{\nu_e} \tag{4.7}$$

can solely be evoked by neutrons. Additionally the measurement of the β^- decay of the metastable $^{116}\mathrm{In}^*$ to ^{116}Sn emitting an electron as well as an antineutrino $\overline{\nu_e}$ also ascertained the number of generated neutrons. The activity of $^{116}\mathrm{In}^*$ was measured

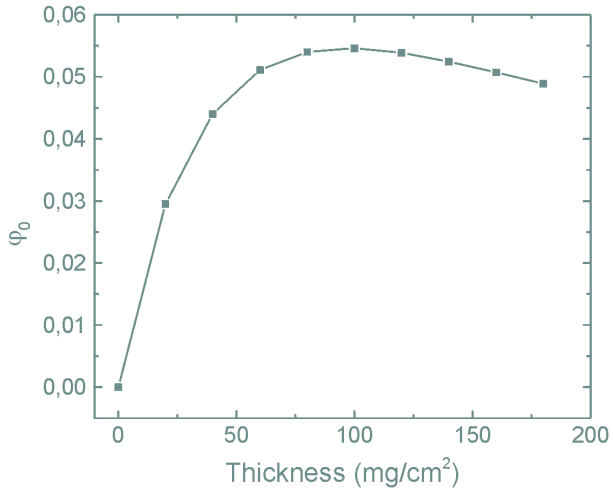

Figure 4.4: Function φ_0 as a function of the areal density of an indium foil to determine their optimum thickness for this experiment. The chosen areal density of 100 mg/cm^2 was close to the optimum at 90 mg/cm^2.

using a standard Geiger-Müller counter, which covered a solid angle, Ω, of 2π. This secondary detector was specially shielded to account for a low background.

Activation Foils

The activity $\dot{A}$ of an indium foil at a time, t, after its exposure, which was much shorter than the half-life of $^{116}\mathrm{In}^*$ is

$$\dot{A}(t) = \Sigma_{act}\,\Phi\,F\,x\,\delta_i(x)\,\delta_a(F,x)\,\mathrm{e}^{-\lambda t}, \tag{4.8}$$

where Φ defines the flux of neutrons, which exposed the indium foil of surface F and thickness x. The decay constant of this reaction is λ. The macroscopic cross section to capture a neutron is Σ_{act}, and δ_i and δ_a are corrections for the inner and outer flux depression in the foil facing the entrance window of the Geiger-Müller counter [61]. The obtained counting rate, $\dot{z}$, and the actual activity, $\dot{A}$, are correlated as

$$\dot{z} = \dot{A}\,\frac{\Omega}{4\pi}\,f_s(x), \tag{4.9}$$

where the correcting factor f_s accounts for the self-absorption of the emitted electrons within the foil. Additional corrections for the absorption of these electrons within the entrance window of the Geiger-Müller counter were neglected. Combining Eq. 4.8 and Eq. 4.9, the initial counting rate $\dot{z}^{(0)}(t=0)$ can then be given as

$$\dot{z}^{(0)} = \frac{F}{2}\,\Sigma_{act}\,\Phi\,x\,\delta_i(x)\,\delta_a(F,x)\,f_s(x), \tag{4.10}$$

Figure 4.5: Schematic of geometry for secondary indium activation targets.

where $\Sigma_{act}\, x\, \delta_i(x)\, f_s(x)$ is defined to be $\frac{1}{2}\,\varphi_0$ and is shown in Fig. 4.4 as a function of the areal density, ρx, of the indium foil. These corrections were taken from [61] and the diameter of the round indium foils was chosen to be 29 mm. Consequently, the flux of generated neutrons, Φ, can then be calculated as

$$\Phi = \frac{100(\mathrm{cm}^2)}{F(\mathrm{cm}^2)}\,\dot{z}^{(0)}. \tag{4.11}$$

Activating ^{115}In is of particular interest since the decay given in Eq. 4.7 has got a half-life, $T_{1/2}$, of 54 min. Increasing the flux of neutrons exposing this activation target, i.e. increasing its activity and therefore decreasing the relative error of the activation measurement, implies its installation as close as possible to the neutron source. This was done by placing these activation targets inside the evacuated target chamber. Therefore it is necessary, that the half-life of the activation targets is much in excess of the time to let up the target chamber. Since this procedure took approximately 12 min, indium could serve as the activation target.

Moreover, ^{115}In has got a high neutron capture cross section of several hundred mb for neutrons with a kinetic energy of some eV [84]. Since the expected neutron energy for $D(d,n)^3He$ for this experiment is in the MeV order, these neutrons needed to be slowed down. This was done by installing the ^{115}In targets in polyethylene bricks, which acted as a moderator. Within these bricks, the indium foils were installed at distances, $\tilde{x}$, between 2.5 and 30 cm. This set-up was placed at closest 9 cm from the gas jet nozzle and at an angle, θ, of 90°. This arrangement is indicated in Fig. 4.5

Fermi's Age Theory

The spatial distribution of neutrons with different energies, which result from their diffusion within the moderator is described by Fermi's Age Theory [85]. The spatial

density of these slowed down neutrons, $q = q(\tilde{x}, \tau)$, in such a moderator can be given as

$$\frac{\partial q}{\partial \tau} = \frac{\partial^2 q}{\partial \tilde{x}^2}, \tag{4.12}$$

where τ is the Fermi Age in (cm^2). This Fermi Age describes the dispersion of the slowing down process and thus characterizes the efficiency of the moderator.

In the following the neutron source is assumed to be isotropic and at the center of the gas jet. Since the moderator was quite some distance away from this gas jet, it can be assumed that the generated neutrons enter this moderator homogenously with a certain source strength, $\dot{Q}_1$. In this case and following the geometry defined in Fig. 4.5, it can be written that

$$\frac{\partial q}{\partial \tau} = \frac{\partial^2 q}{\partial \tilde{x}^2} + \dot{Q}_1 \, \delta(\tilde{x}) \, \delta(\tau), \tag{4.13}$$

when $q = 0$ for $\tilde{x} = \pm\infty$. Consequently, the solution of Eq. 4.12 can be derived by a Fourier transformation of the latter equation and is found to be

$$q(\tilde{x}, \tau) = \frac{\dot{Q}_1}{\sqrt{4\pi\tau}} \, \exp\left(-\frac{\tilde{x}^2}{4\tau}\right). \tag{4.14}$$

Due to the measured counting rate of the single indium foils within this moderator this spatial neutron density distribution is known and q is consequently proportional to $\dot{z}^{(0)}$. Thus, measuring the relative density of neutrons within the polyethylene bricks determines $\dot{Q}$, i.e., the total number of neutrons generated during the interaction of the laser with the plasma. For this cylindrical symmetry of the set-up $\dot{Q}$ is

$$\dot{Q} = \dot{Q}_1 SK = 2\pi SK \int \Sigma_{act} \, \Phi(\tilde{x}) \, \tilde{x} \, d\tilde{x}. \tag{4.15}$$

Here, S is a correction for the covered solid angle and K a normalization to the PMT's signal, which were recorded simultaneously during this activation.

Measuring the neutron yield with several indium foils at various distances within a moderator offers the advantage that all neutrons with a broad energy spectrum can be detected, since the moderator can be extended over long distances. Using a single activation target either with or without moderator permits solely a single and limited look at neutrons at one position. Determining the entire neutron yield afterwards requires additional assumptions on their initial spectrum.

Assuming an isotropic emission profile of neutrons which should be determined with the activation of ^{115}In, it is necessary that the counting rate with the Geiger-Müller detector exceeds its background counting rate. This was tested before the actual

experiment and it was calculated that at least 10^4 neutrons have to be generated to make this set-up sensitive to their detection.

Differences for Thermal and Epithermal Neutrons

Since a precise determination of the neutron yield is essential for the interpretation of the experiment and its results, it is necessary to have a closer look at the process evoking Eq. 4.7. The cross section for this reaction is approximately several hundred mb for thermal neutrons with an energy of around 1/40 eV. However, it can also be triggered by epithermal neutrons with an energy of 1.46 eV due to a resonance of the indium nuclei. Those two neutron energy ranges were distinguished in the experiment by performing the activation of ^{115}In twice : Once solely with indium foils, and a second time by shielding them in their front and back with additional cadmium foils of the same thickness and size. The cross section of cadmium for neutron capture at thermal energies is a factor 100 higher than for indium; for epithermal neutrons it is negligible [84]. The difference in activity between shielded and unshielded indium foils allows calculation of the neutron yield due to the activation of thermal neutrons alone.

Chapter 5

Experimental Results

In the following the results of the neutron as well as deuteron measurements will be presented. Comparisons with calculations will decipher the possibilities for D$(d,n)^3$He neutron generation for the beam target model as well as a thermonuclear deuteron source within the plasma core. Deuteron distribution temperatures will be deduced and the influence of the ambient gas jet will be stressed in particular by the presentation of shots with a secondary solid CD_2 target, which was installed next to the gas jet nozzle.

5.1 Gas Jet Interaction

5.1.1 Neutron Energies

Figure 5.1 shows a typical TOF trace. The observed peak is characteristic for D$(d,n)^3$He reactions as it reflects a neutron energy, T_n, of (2.45 ± 0.05) MeV. The

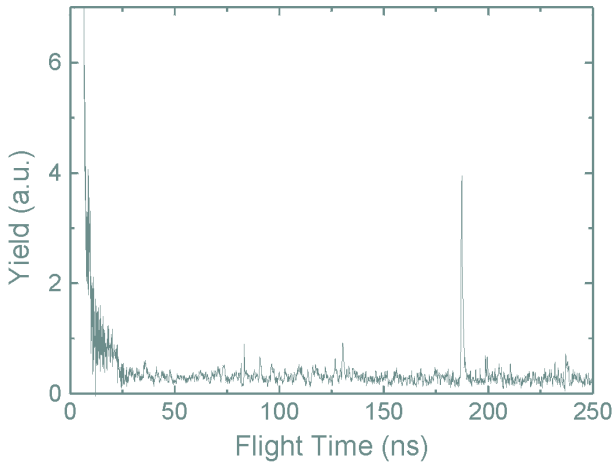

Figure 5.1: Typical TOF signal for a plasma electron density of 5×10^{19} cm^{-3} and a laser energy of 62 J. The prompt signal is the γ-flash due to bremsstrahlung generated by energetic electrons that are produced during this interaction. The peak at 187 ns is produced by neutron events with an energy of (2.45 ± 0.05) MeV.

short pulse confirms furthermore that these neutron events cannot be due to (γ, n) or $(e, e'n)$ processes, which would produce a broader spectrum that would arise from the γ-flash. To ensure that this peak was indeed due to the $D(d, n)^3He$ reaction, additional shots with helium as a target gas were performed. In this case and as it was expected, no neutron peaks were observed.

These TOF traces were converted to neutron energy spectra and corrected for the afterglow of the plastic scintillators. Since these detectors were at some distance from the gas jet, the signals extended typically over more than 10 ns and were therefore much in excess of the response time of the plastic scintillator described by Eq. 4.6. Additional simulations with the Monte Carlo neutron transportation code MCNP [86] were carried out to evaluate the modification of such neutron spectra passing the target chamber. These calculations confirmed that no significant broadening was expected to occur. Interestingly, the relative neutron yield among the single PMT's scaled inversely proportional to the square of the distance, s, from the detector to the nozzle. This is expected for a thermonuclear neutron source. Furthermore, the to the solid angle normalized neutron spectra were quite insensitive to the angle of detection, θ, as it can be seen in Fig. 5.2.

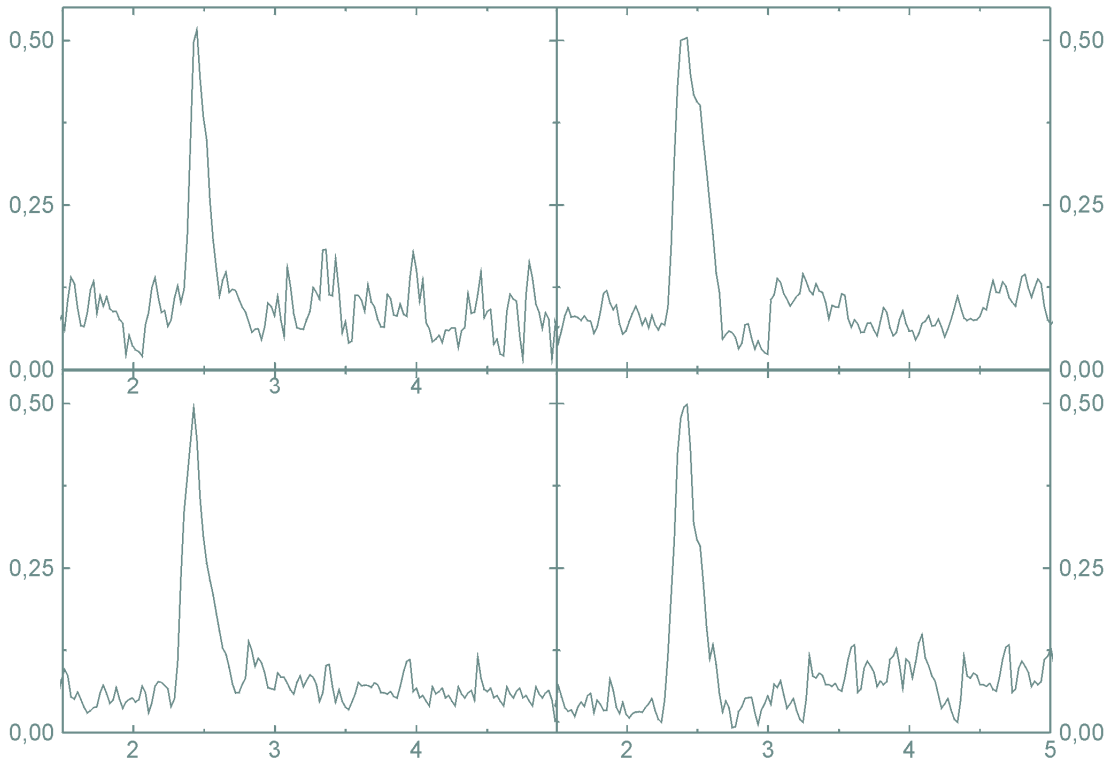

Figure 5.2: Normalized neutron energy spectra for different angles of emission : *(a)* $\theta = 67°$, *(b)* $\theta = 117°$, *(c)* $\theta = 245°$ and *(d)* $\theta = 270°$. At this shot the electron plasma densty, n_e, was 7×10^{19} cm^{-3} and the laser energy, E_L, 57 J.

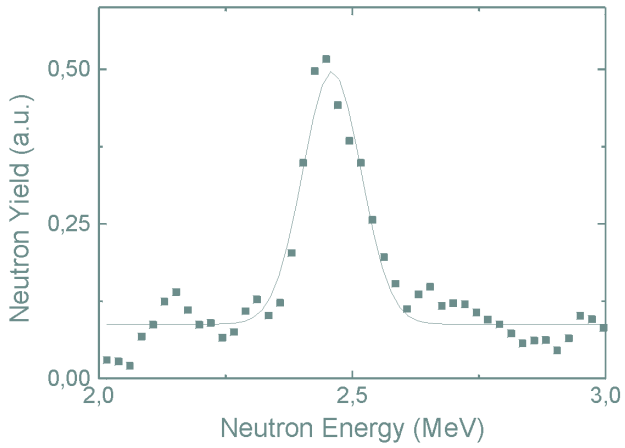

Figure 5.3: Gaussian fit of D$(d,n)^3$He fusion neutron peak. The implied temperature of the assumed Maxwellian deuteron distribution is (1 ± 0.2) keV.

5.1.2 Plasma Ion Temperature

This isotropy and approximate Gaussian shape of the neutron spectra suggest an initial Maxwellian deuteron distribution within the plasma core. A typical example of fitting these neutron spectra with a Gaussian distribution is shown in Fig. 5.3. Implying Eq. 3.8 reveals therefore a Maxwellian deuteron distribution temperature, T, of (1 ± 0.2) keV.

Surprisingly, this temperature did not exhibit a very strong dependence with the deuteron density as it is indicated in Table 5.1 for two arbitrary shots. However, this is not expressed in this particular fit, but characterizes the underlying deuteron heating mechanism itself.

Table 5.1: Maxwellian deuteron distribution temperatures, T, for different plasma densities, n_e, measured under different angles, θ, for the same laser energy, E_L, of 57 J.

	$n_e = 3 \times 10^{19}$ cm^{-3}	$n_e = 7 \times 10^{19}$ cm^{-3}
Angle θ (deg)	Temperature T (keV)	Temperature T (keV)
67	(1.1 ± 0.4)	(1.1 ± 0.4)
117	(0.9 ± 0.2)	(1.0 ± 0.3)
245	(1.2 ± 0.3)	(0.8 ± 0.2)
270	(1.0 ± 0.2)	(0.9 ± 0.2)

The indicated error bars are mainly influenced by the uncertainties of the detector position and the fit of the signals. It is noted that the relative errors between two shots under the same experimental conditions could be up to 40%.

5.1.3 Neutron Yield

The counting rates of the single indium foils for the two shots with and without cadmium shielding were corrected for the exponential decay to their initial activation, $\dot{z}^{(0)}$. To ensure that no great fluctuations between these two laser shots influenced this measurement, one unshielded indium foil was installed at one fixed position for normalization. Extensive additional measurement of scattered neutrons or those generated by other processes can be precluded, since this moderator was heavily shielded in any direction by extra layers of polyethylene.

The integration over the distribution shown in Fig. 5.4 gave the number of measured neutrons. In order to obtain the total yield according to Eq. 4.15, two corrections were applied, where S marked the solid angle this activation set-up has covered. This can be assumed to be the surface, F, of the indium foils at the entrance of the moderator. Additionally, K corrected the relative fluctuations between the single shots. Since the angular distribution measured with the PMT's was found to be almost isotropic, the total yield was determined to be $(1.0 \pm 0.2) \times 10^6$ neutrons.

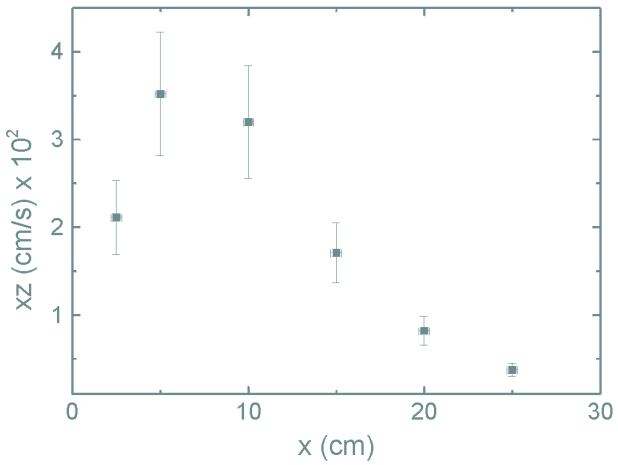

Figure 5.4: Measured counting rate of indium foils within the moderator. These values were corrected for the exponential decay of the $^{116}In^*$ as well as the background counts during this measurement.

5.2 Beam Target Interaction

Another possibility for neutron generation by $D(d,n)^3He$ reactions in this experiment was the propagation of the Coulomb explosion deuterons through the ambient and stationary gas jet. To assess if the observed neutron yield could be due to this beam target interaction its practicability was investigated in detail.

5.2.1 Deuteron Measurements

5.2.1.1 Deuteron Spectrum

As mentioned in the previous chapter, the spectrum of the deuterons accelerated by the Coulomb explosion was measured using a Thomson parabola at 90° relative to the laser beam axis. As can be seen in Fig. 5.5 these measurements reveal a maximum deuteron energy of (1.2 ± 0.2) MeV. Equating this to the ponderomotive potential energy, U_{max}, given in Eq. 2.60 indicates that the averaged intensities in the focal spot were as expected of the order 10^{19} W/cm^2.

This spectrum did not change in temperature with varying plasma electron density and it was even found once n_e was below the threshold for wavebreaking, n_{WB}, at 1.5×10^{19} cm^{-3}. This is not surprising, since the ponderomotive ion energy, U_{max}, is solely a function of the laser intensity. However, this ascertains that the interaction of the deuteron beam with the ambient gas did not generate the observed neutrons, since the neutron signal dropped below the detection limit once the electron plasma density was below n_{WB}.

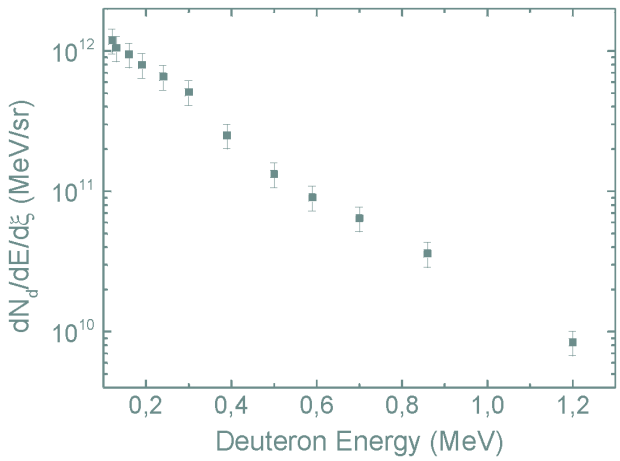

Figure 5.5: Deuteron spectrum from Coulomb explosion as measured by the Thomson parabola.

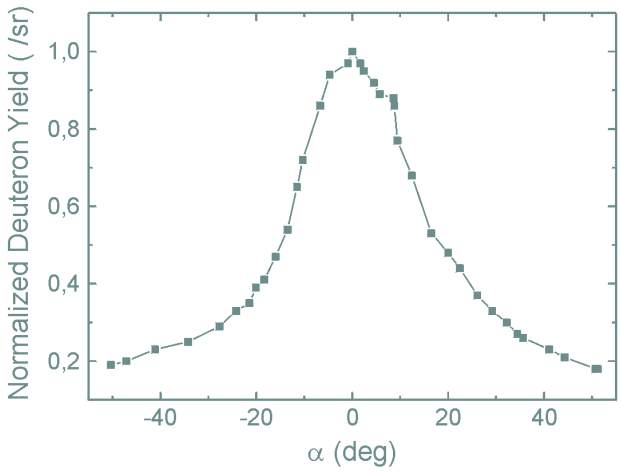

Figure 5.6: Angular distribution of deuteron emission as measured by radiochromic film. The error bars are within the dot size.

5.2.1.2 Angular Distribution

Figure 5.6 shows, that this deuteron emission was sharply peaked towards the direction of the Thomson parabola. To ensure that this signal was indeed due to deuterons additional shots with a pinhole and CR-39 were carried out. As this created pits in the detector it ensured that this signal was due to deuterons.

Evaluating the total number of deuterons by applying Eq. 4.3 reveals that in these experiments about 2×10^{11} deuterons were accelerated beyond a kinetic energy of 100 keV. However, the total number of deuterons as a function of their energy was not determined in this experiment as the Thomson parabola was only installed at 90° relative to the laser axis. Therefore, it was assumed for the ensuing calculations that this total deuteron number of 2×10^{11} is the integral over the deuteron spectrum and this measured opening cone. It is likely that this assumption is too optimistic as the maximum accelerating field and thus the highest deuteron energies due to the Coulomb explosion are predominantly along the axis the Thomson parabola was installed. Nevertheless, this can be taken as an upper limit, since a higher deuteron energy has a higher cross section for the $D(d,n)^3He$ reaction, as was shown in Fig. 3.4.

5.2.1.3 Expectations for Neutron Generation

Calculating the upper-limit yield that such a deuteron beam produces as it travels through the ambient gas surrounding the plasma, one finds by applying Eq. 3.9 that no more than 10^4 neutrons are produced this way due to the relatively low deuteron density, n_D, within the gas jet even at its highest density used. However, the above described activation measurements revealed a total neutron yield, which was two orders of

magnitude higher than what this classical beam target interaction produces. Moreover, such a deuteron beam would lead to broad neutron spectra between 1.75 and 4.2 MeV, which should vary relative to the detection angle as discussed in Chapter 3.3.1.1. Experimentally, such a variation was not observed and solely neutron energies of around (2.5 ± 0.05) MeV were detected.

5.2.2 Secondary CD_2 Target

To demonstrate this more clearly, a 200 μm thick and 5 mm wide solid deuterated plastic (CD_2) target was placed 2.5 mm away from the interaction at the same angle as the Thomson parabola and as indicated in Fig. 5.7. The purpose of this target was to simulate the beam target interaction of the expelled deuterons as they pass through the stationary ambient gas, but obviously with a much higher reaction rate due to the higher deuteron density in the solid.

5.2.2.1 Neutron Energy

This modified set-up did change the energy spectrum of the detected neutrons as can be seen in Fig. 5.8. Comparison with calculated neutron energy as a function of angular emission given in Fig. 3.2 reflects a continuous deuteron distribution for the $D(d,n)^3He$ reaction up to an energy of (1.0 ± 0.1) MeV. This is indeed, what was previously measured with the Thomson parabola.

By reversing Eq. 3.9 it is possible to determine which deuteron distribution caused the neutron spectrum shown in Fig. 5.8. This calculation reveals that these neutrons had to be produced by a Maxwellian deuteron distribution with a temperature, T^{calc},

Figure 5.7: Schematic of set-up with secondary 200 μm thick and 5 mm wide solid deuterated plastic (CD_2) target was placed 2.5 mm away from the interaction at the same angle as the Thomson parabola.

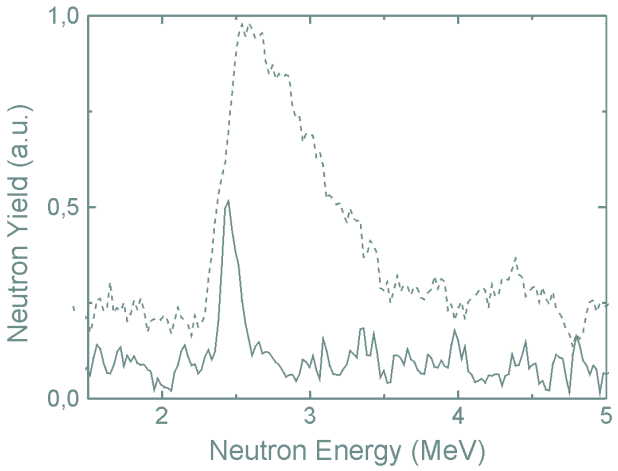

Figure 5.8: Neutron spectra for a detector at θ of 67° with (dashed line) and without the secondary CD_2 target (solid line). For both shots the experimental conditions were the same.

of (186±39) keV. This compares favorably with the measured ion temperature, T^{exp}, of (216±36) keV shown in Fig. 5.5. Thus, it is found that with this secondary target, the calculated beam target reaction accurately describes the observed neutron spectrum and yield. However, without the target none of the features of the beam target reaction were observed.

Clearly, the entire neutron yield increased significantly with the secondary target. Figure 5.8 shows a one order of magnitude increase due to the higher deuteron density, n_D, with the solid target than without it.

5.2.2.2 Angular Distribution

This significant difference between the shots with and without the solid CD_2 target is also emphasized by the angular dependence of the neutron emission as presented in Fig. 5.9 for the experimental results as well as the calculated angular dependence for the beam target model.

With Secondary CD_2 Target

In the case of $D(d,n)^3He$ reactions with the secondary target, an angular variation in the distribution can be observed with a minimum in the laser propagation direction, since this direction is orthogonal to the motion of by the Coulomb explosion accelerated deuterons. This compares favorably with the calculations.

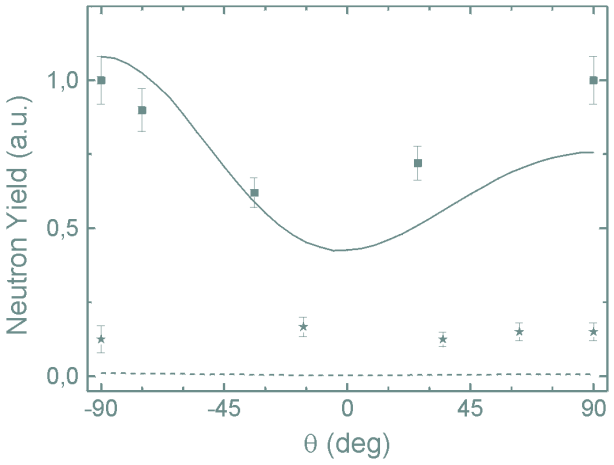

Figure 5.9: Angular distribution of neutrons with (squares) and without (stars) the solid CD_2 target for two typical shots. Also included is the expected yield for the beam target model with (solid line) and without the secondary CD_2 target (dashed line).

Ambient Gas Jet

Obviously, such a calculation for beam target interactions with the ambient gas jet target only results in a slightly changing curve. However, the actual experimental result has a factor 100 higher neutron yield, which, hence, cannot be explained by this scenario.

Chapter 6

Discussion

In summary, in the previous chapter it was shown that the interaction of a 62 J, 1 ps laser focused down to intensities of 2×10^{19} W/cm^2 onto a deuterium gas jet with an electron plasma density of 1×10^{20} cm^{-3} can yield up to $(1.0 \pm 0.2) \times 10^6$ fusion neutrons with an isotropic emission profile. Additionally, it was demonstrated that the interaction of the Coulomb explosion expelled deuterons propagating through the ambient gas jet cannot account neither for the yield nor the angular distribution of the measured neutrons. It was therefore deduced that plasma ions are heated to fusion temperatures of about 1 keV by a noncollisional heating mechanism during this interaction.

With Eq. 3.10 a simplified estimate for the expected neutron yield for a thermal deuterium plasma is given. Assuming that the confinement duration, τ, is about the plasma disassembly time, i.e. $\tau = w_0/C_s$, where C_s is the ion sound speed, and that the volume, V, is given by the original laser volume and the length of the gas jet, no more than 10^2 neutrons can be obtained. On the other hand, to reach a yield of 10^6 neutrons an ion plasma temperature of 40 keV would be required. Consequently, the assumption made in Chapter 2 that plasma ion motion in the interaction of a high-intensity laser with an underdense plasma can be neglected for the time of the laser pulse duration appears not to be entirely tenable.

The discrepancy between the temperature measured from the neutron spectra and that implied by the yield suggests that the assumption of a Maxwellian deuteron distribution, underlying the calculations presented in Chapter 3.3.1.2 is not adequate. In particular, it suggests the existence of a hotter tail of deuterons which are colliding with small center of mass momentum, which results in less broadening of the neutron spectrum than expected. Due to the great dependence of the D$(d,n)^3$He cross section with deuteron energy, this could significantly enhance the neutron yield.

The neutron yield may also be increased due to a heating over a larger volume and over time greater than the disassembly time due to shock heating. This was recently demonstrated in numerical simulations [138]. There, the plasma response to a ps laser focused down to intensities of 10^{18} to 10^{19} W/cm^2 was characterized by several distinctly different time scales. It was shown, that such a strong laser pulse is capable of driving MA ion currents with a typical ion energy of 50 to 150 keV, which, hence, could initiate D$(d,n)^3$He reactions. This too would result in an overestimation in the temperature as calculated from the simplified yield equation.

It is well known that the interaction of an intense laser pulse with underdense plasmas can result in efficient absorption of the laser pulse. This can lead to the production of not only beams of energetic electrons but also to a hot thermal bulk of electrons [88]. However it is also evident that for the range of densities explored in this study, the time for the electrons to equilibrate with the ions is well in excess of the disassembly time for the plasma. For the conditions presented here, τ_{eq} is more than 1 ns. Hence, this ion heating must be the result of direct non-collisional heating mechanisms that occurs on the time scale of the laser pulse. The simplest explanation for the ion heating is due to variations in the Coulomb potential caused by the ponderomotive expulsion of charge by the laser pulse. This is quite likely due to the presence of self-focusing and other propagation instabilities under these conditions. However, it is also noted that by systematically varying the plasma density, a correlation was observed between the neutron yield and the generation of energetic electrons. As has been noted previously, the electrons are generated by wavebreaking and result in a hot electron tail in the distribution with a total current approaching the Alfvén limit [89]. At densities, n_{WB}, below the wavebreaking limit of about 1.5×10^{19} cm^{-3}, both neutron and hot electron yields dropped dramatically. However above this deuteron density, the neutron yield showed no great variation with density. Recent simulations have shown that the filamentation and propagation instabilities of such high current electron beams in a plasma can result in collisionless heating of the ions to a hot tail with energies as high as 100 keV [90].

Part III

Electron Beam Generation in the FLWF Regime

Chapter 7

Experimental Layout

In this chapter a brief review will be given on previously performed experiments on electron beam generation by the interaction of high-intensity lasers with underdense plasmas. This introduction will conclude with the motivation for the experiment presented here, which was carried out on the "salle jaune" laser at Laboratoire d'Optique Appliquée (LOA). Subsequently, the layout of this experiment will be discussed in detail, starting with the laser beam and gas jet parameters as well as the electron beam diagnostics used such as the magnetic spectrometer, integrating current transformer, radiochromic film and copper stack, activation set-up and emittance diagnostics, as these revealed information on a new electron acceleration regime.

7.1 Previous Experiments and Motivation

For lucidity due to the great variety of possible electron acceleration mechanisms by laser plasma interactions only the forward Raman scattering (FRS) and self-modulated laser wakefield (SMLWF) schemes introduced in Chapter 2 will be discussed in the following, as they appear to be the dominant mechanisms.

The first experimental observation of FRS was reported in [23], where electrons with a kinetic energy of up to 1.4 MeV were measured, when a weakly relativistic CO_2 laser with a wavelength of 10 μm, FWHM pulse duration of 700 ps and a normalized vector potential of 0.3 was focused onto thin carbon foils of 130 Å thickness. Integration over the measured azimuthal angular distribution revealed that about 10^{11} electrons with energies greater than 400 keV escaped the plasma.
In the SMLWF regime an electron beam with an energy of up to 44 MeV was obtained in [7] by focusing a 25 J, 1 ps FWHM Nd:Glass laser pulse down to a focal waist of 20 μm onto a 4 mm helium gas jet, which delivered a neutral electron density of 1.5×10^{19} cm^{-3}. This interaction lead to wavebreaking, which was determined by the sudden increase in both, the number and the maximum energy of generated electrons, as well as the loss of coherence of the plasma wave, which was observed from the broadening of forward Raman satellites. This measurement of high energy electrons was limited by the electron spectrometer used, which is why in [91] a maximum electron energy of 100 MeV was reported for similar experimental conditions. Interestingly, this electron energy gain indicated a greatly extended dephasing length. Measurements of

the Thomson scattered light on the relativistic plasma wave along the laser propagation axis indicated a self-guiding of the laser pulse over the entire gas jet length and an electron plasma wave amplitude of (40 ± 20) % [92].
The angular distribution of such energetic electron beams was recently characterized by photonuclear techniques, when a highly relativistic electron beam was produced by focusing a 50 TW laser beam down to intensities of about 10^{19} W/cm^2 onto helium gas jets with neutral plasmas electron densities beyond 1×10^{19} cm^{-3} [89]. Behind the gas jet these electrons were converted in a secondary high Z target into γ-rays, which induced (γ, n) reactions in several copper wedges installed in a circle behind this converter. The relative activity of those wedges indicated that the high energy electron beam has a large opening cone centered on the laser beam axis with a FWHM of at least 10°, which increases with plasma density.
Due to enhancements in laser technology these intensities also became recently available at "table top", Ti:Sa laser systems, which operate at higher repetition rates of 10 Hz. Here, electrons with energies of up to 12 MeV were obtained focusing a 250 mJ, 1.2 TW laser down to intensities of 4×10^{18} W/cm^2 onto helium gas jets with neutral electron densities of up to 4×10^{20} cm^{-3} [93]. As it was reported in [94], this maximum electron energy was increased up to 70 MeV by using 600 mJ, 35 fs FWHM laser pulses focused down to intensities of 2×10^{19} W/cm^2 onto a helium gas jet with a neutral electron density of 5×10^{19} cm^{-3}. Increasing the neutral plasma electron density it was observed that the maximum electron energy decreases, which indicates that higher plasma wave phase velocities correspond, as expected, to higher electron energies.

Up to now it was shown that the interaction of relativistic laser pulses with underdense plasmas in the SMLWF regime, where the laser pulse length, $c\tau_0$, is much longer than the plasma wavelength, λ_p, can be a bright source of energetic electron beams. The temporal structure of these electron beams appears to be similar to the modulated laser envelope, thus consisting of a train of electrons with single bunch lengths of the order of λ_p and a total bunch length comparable to $c\tau_0$ [95]. However, for accelerator or pump-probe experiments single and ultra short electron bunches would be preferential. Therefore, implementing a Ti:Sa laser, the aims of the experiment presented in this manuscript were to

1. enhance the electron beam quality in terms of bunch length as well as emittance
2. increase the maximum electron energy.

Obviously, the collimation of the generated electron beam will be improved when radial accelerating fields are diminished. This can be achieved if the laser focal waist is much in excess of the plasma wave number, $w_0 k_p \gg 1$. As it was shown in Chapter 2.2.3.3 the energy gain of electrons in relativistic plasma waves is higher, the lower the plasma electron density, since this increases the phase velocity of the wave. Finally, a single electron bunch might be generated if only one cycle of such a plasma wave could be driven to wavebreaking.

Figure 7.1: Schematic of the "salle jaune" Ti:Sa laser chain configured for CPA operations. The single components are briefly described in the text.

7.2 Experimental Parameters

7.2.1 "Salle Jaune" Laser and Optical Diagnostic

This experiment was performed on the "salle jaune" laser at Laboratoire d'Optique Appliquée, which is an infrared titanium-doped sapphire (Ti:Sa), p-polarized laser based on a classical CPA configuration [70]. It is capable of generating 100 TW laser pulses with a FWHM pulse duration of 25 fs [96]. An overall schematic of this laser chain is given in Fig. 7.1.

The laser chain starts from a Ti:Sa self-mode-locked oscillator, which produces a 88 MHz, 300 mW train of laser pulses of 15 fs duration. Each of these pulses is stretched up to 400 ps in an aberration-free stretcher and then injected into an acousto-optic dispersive filter (AOPDF). This permits to actively control the spectral shape and to adjust the spectral phase of the laser pulses. Subsequently, a pulse picker selects single pulses at a repetition rate of 10 Hz. Pockels cells act both as a back reflection isolator as well as a temporal gate which limit the ASE energy. These 1 nJ pulses are first amplified to 2 mJ in a 8-pass preamplifier and then injected into a 5-pass power amplifier to reach an energy of 200 mJ. After each amplification stage the beam is spatially filtered by Air

Table 7.1: "Salle jaune" laser parameters for electron acceleration experiment.

Laser Wavelength	λ_L		820 nm
Energy on Target	E_L	$\leq$	1 J
Pulse Length	τ_0		30 fs
Repetition Rate			10 Hz
Waist of Focal Spot	w_0		18 μm
Peak Laser Intensity	I_L	$\leq$	3×10^{18} W/cm^2
Contrast Ratio		$\geq$	1×10^6

Spatial Filters (ASF) and Vacuum Spatial Filters (VSF) to increase the spatial quality of the laser beam as well as to limit its flux below the damage threshold of the crystal of the third amplification stage. This high power amplifier is cryogenically cooled to cancel the thermal dependence of the laser wavefront and to amplify the laser pulses after four passes up to an energy of 3.5 J. Finally, the laser pulses can be re-compressed with a 60 % efficiency to 25 fs after four passes on two parallel gratings.

For the described experiment, this laser beam was focused down to a focal waist, w_0, of 18 μm using a $f/18$ off-axis parabolic mirror. This results in a normalized vector potential, a_0, of 1.2. The spectrum of the laser beam after the interaction with the plasma was routinely analyzed with an optical spectrometer and recorded onto a 18-bit CCD camera, like it was described above in Chapter 4.2.1. Table 7.1 gives the typical laser parameters during this experiment.

7.2.2 Initial Plasma Electron Density

The laser was focused onto the sharp edge of a 3 mm diameter supersonic helium gas jet since helium has a simple atomic structure, which ensures its full ionization due to the pedestal of the laser pulse. The neutral density profile of this jet was characterized by interferometry and found to be uniform [72]. The plasma period, $2\pi\omega_p^{-1}$, was chosen to vary between 25 and 14 fs by selecting initial electron densities, n_e, between 2 and 6×10^{19} cm^{-3}, which was achieved by changing the backing pressure on the gas jet.

It is noted that for these parameters the SMLWF regime, where $c\tau_0 \gg \lambda_p$, is ruled out as the electron acceleration mechanism. Nonetheless, electron trapping and acceleration from the breaking of a relativistic plasma wave can still be obtained in what is later termed "Forced Laser Wakefield" regime. How these generated electron bunches were characterized experimentally will be described in the following.

Figure 7.2: Experimental set-up at "salle jaune" laser. The laser beam was focused with an off-axis parabolic mirror *(a)* onto the edge of a 3 mm helium gas jet *(b)*. The total number of generated electrons was determined with an Integrating Current Transformer *(c)*, which could be replaced with a secondary set-up for activation and emittance measurements. The transmitted laser beam was analyzed with an optical spectrometer and recorded onto a CCD camera *(d)*. A glass plate with a center hole separated the laser and electron beams non-destructively. The electron yield as a function of energy was determined with a spectrometer, which electrons could entered through a collimator *(e)* and measured with silicon barrier detectors *(f)*. Lead walls shielded those from bremsstrahlung *(g)*.

7.3 Electron Beam Diagnostics

The overall layout of the experimental set-up is shown in Fig. 7.2. The implemented diagnostics will subsequently be discussed in detail.

7.3.1 Electron Spectrometer

7.3.1.1 Electromagnet

The spectrum of the generated electron beam was measured with an electromagnet and Silicon Barrier Detectors (SBD's). Electrons could enter the magnet 1 m behind the gas jet nozzle through a 4 cm thick stainless steel collimator with an internal diameter of 1 cm. Depending on their energy, W_e, electrons are dispersed in the magnetic field. Due to the specially shaped pole pieces of this electromagnet the electron source originating from the gas jet nozzle is imaged on the focusing plane of this device, where up to four SBD's were installed. The radius, R_B, of this electron dispersion can be given in (m) as

$$R_B = \frac{\sqrt{W_e(W_e+1)}}{300B}, \tag{7.1}$$

when W_e is expressed in (MeV) and the magnetic field of the spectrometer, B, in (T). This magnetic field of the electromagnet, and hence the dispersion of the spectrometer, can be altered by changing the current passing through the solenoidal coils, which allows to measure with the same instrument a wide range of energies on a series of shots with different current settings. Due to the geometry of this device the total range in imaging mode is from 0 to 217 MeV.

7.3.1.2 Silicon Surface Barrier Detectors

The dispersed electrons were detected with SBD's, which had a circular area of approximately 1 cm^2. These detectors are biased, and the current generated by ionizing radiation in the diodes depletion region was measured on oscilloscopes. The number of electrons, N, as a function of electron energy in (MeV) can then be derived from

$$N(/\text{MeV}) = 5 \times 10^6 \frac{V_{max}}{W_{depo}}, \tag{7.2}$$

where V_{max} is the maximum voltage in (V) of the usually 20 ps wide signals measured. The in (keV) deposited energy of electrons in the SBD is W_{depo} and given in (MeV) as

$$W_{depo} = l\rho P_{stop}, \tag{7.3}$$

where l is the thickness of the diode depletion region in (cm), ρ its density in (g/cm^3) and P_{stop} its stopping power in (MeV cm^2/g), which is listed in [97]. Due to the used collimator these electron spectra are furthermore normalized to a solid angle, $\triangle\Omega$, of 0.0785 msrad.

7.3.1.3 Energy Resolution and Detection Threshold

The attainable electron energy resolution, $\triangle W_e$, of this set-up is determined by the dispersion of the electron spectrometer and the diameter of the SBD's. As a function of electron energy, W_e, it varies in between 0.5 and 1 MeV.

The detection threshold of this device shows a strong dependence on the noise level, which is different for any set-up as well as electron energy. To ensure that the signal obtained with the SBD's is indeed due to electrons and in order to achieve an optimum data acquisition the noise levels for this electron detector were eliminated as follows.

First, sources of electric noise in the data acquisition were suppressed by shielding any electric device. Second, the magnetic field was slowly varied during a measurement over its entire range from 0 to 1.5 T, which changed the obtained signal correspondingly. Third, because SBD's are also sensitive to bremsstrahlung, thick lead walls next to the collimator as well as around the detectors were set up to suppress stray γ-rays. Fourth,

because the spectrometer focuses the electron beam but obviously has no influence on the propagation of γ-rays, a clear distinction between the signal in and out of the focusing plane can be ascertained. Here, only signals with a signal-to-noise ratio of better than 25:1 were considered. Finally, 1 cm thick copper pieces were installed directly in front of the SBD's. This changed the signals according to the stopping power in copper. With those precautions the detection threshold of this spectrometer is for, say, 10 MeV electrons about 100 electrons.

7.3.2 Integrating Current Transformer

To monitor the entire electron bunch charge an Integrating Current Transformer (ICT) was implemented, which is simply an electric spool the electron beam could pass through. The ICT inductively couples to the electron beam, which generates a current that is transformed electronically to a voltage [98].

The ICT used had an internal diameter of 10 cm and was placed 20 cm behind the gas jet nozzle. It gave unipolar pulses approximately 20 to 30 ns wide, the integral of which was proportional to the electron bunch charge. Under the conditions of interest, the pulse height was very linearly dependent on the electron bunch charge, and being a rapidly measurable quantity on an oscilloscope.

It is noted that a minimum bunch charge of 20 pC is required to obtain an ICT signal beyond the noise level. In order to prevent any influence of the high-intensity laser pulse, which would also pass through the ICT, this device was shielded with a black pasteboard, whose stopping power for low energy electrons has to be taken into account. Self-explanatory, an ICT is insensitive to bremsstrahlung.

This total charge of the electron beam could also be calculated by the convolution of the measured electron spectrum and its angular divergence as a function of energy. How the latter was experimentally obtained will be described in the following.

7.3.3 Radiochromic Film and Copper Stack

In order to obtain furthermore information about the opening cone of the generated electron beam as a function of its energy, a secondary detector was implemented. This consisted of a stack of radiochromic film (RCF), which was introduced in Chapter 4.2.2.3, to visualize and copper pieces of various thicknesses to stop the electron beam. To avoid illumination of the RCF by the laser, this stack was completely shielded with aluminium wrapping. It was placed on the laser beam axis behind the center of the gas jet nozzle, like it is indicated in Fig. 7.3.

The traces on the single RCF's correspond to the opening cone of all electrons, which had the required minimum energy, W_e^{min}, to penetrate the RCF at its position inside the stack. This energy can be calculated by the above mentioned stopping power

Figure 7.3: Schematic of radiochromic film and copper stack, which was installed behind the gas jet nozzle. The copper pieces (Cu) stopped the electron beam, whose beam envelope was visualized with radiochromic film (RCF). The opening cone of the electron beam as a function of its energy, θ_{oc}, can be obtained by subtraction of the measured opening cone, θ_{ex}, and the calculated scattering angle of electrons propagating through matter, which is described in the text.

of the stack. Analyzing all RCF's the FWHM of the opening cone of the electron beam as a function of its energy can be reconstructed by subtraction. The energy bin that is resolved with any RCF is determined by W_e^{min} and the electron energy to reach the subsequent RCF without penetrating it. This was typically found to be ± 0.5 MeV.

Special attention has to be paid to the scattering of electrons passing through this stack as this increases the measured opening cone of the electron beam. This scattering is described by the theory of Molière in the following.

Theory of Molière

Electrons traversing a medium of thickness d are deflected by many small angle scatters, where most of this deflection is due to Coulomb scattering from nuclei. This scattering angle, θ_{sc}, can be approximated as

$$\theta_{sc} = \frac{13.6\text{MeV}}{\beta c p}\sqrt{\frac{d}{X_0}}\left[1 + 0.0038\ln\left(\frac{d}{X_0}\right)\right], \tag{7.4}$$

when p and βc are the momentum and velocity of the electron and X_0 the radiation length of the medium, which is the mean distance over which a high energy electron loses all but $1/e$ of its energy. This radiation length can be estimated as

$$X_0 = \frac{716.4\,\text{g}\,\text{cm}^{-2} A}{Z_T(Z_T+1)\ln(\frac{287}{\sqrt{Z_T}})}, \tag{7.5}$$

where A is the mass number and Z_T the charge number of matter the electron is passing through [99]. Consequently, the traces on the RCF correspond to the opening cone of

Figure 7.4: Schematic of activation measurements. By sending the electron beam through a tantalum (Ta) piece, bremsstrahlung was generated, which induced (γ, n) reactions in copper (Cu) or coal (C) wedges placed in a circle behind the converter. The angular distribution of bremsstrahlung with an energy beyond the threshold for these reactions is obtained from the relative activity of the wedges.

the electron beam and its scattering within this stack. Hence, they need to be corrected for θ_{sc} in order to obtain the opening con of the electron beam, $\theta_{oc} = \theta_{ex} - \theta_{sc}$.

7.3.4 Nuclear Activation Diagnostic

As mentioned in Chapter 4.2.2.3 radiochromic film is sensitive to bremsstrahlung. To ensure that the traces obtained with the above described RCF and copper stack are indeed due to electrons this measurement was verified with secondary (γ, n) activation of ^{63}Cu and ^{12}C. Figure 7.4 indicates this below described nuclear activation diagnostic, which was installed behind the gas jet nozzle.

The electron beam escaping the plasma was incident on a 2 mm thick tantalum slab, which was installed 2 mm behind the gas jet nozzle. Here, a significant part of the electron kinetic energy was converted into hard γ-rays via the bremsstrahlung mechanism. Subsequently, these photons induced (γ, n) reactions in copper or coal wedges placed in a circle 22.5 mm behind the converter. To trigger the nuclear reactions given in Tab. 7.2 the incident photon energy must be above the reaction threshold

Table 7.2: Nuclear reactions used. The reaction threshold is Q, the peak cross section σ_{max} and the half-life of the reaction product $T_{1/2}$.

Reaction	Q (MeV)	σ_{max} (mb)	$T_{1/2}$ (min)	Decay
$^{63}\mathrm{Cu}(\gamma, n)^{62}\mathrm{Cu}$	9.7	75	9.7	β^+
$^{12}\mathrm{C}(\gamma, n)^{11}\mathrm{C}$	18.7	9	20.4	β^+

energies, Q. Consequently, this diagnostic is solely sensitive to the higher energy part of the γ-spectrum. The angular distribution of such γ-rays was obtained from the relative activity of the copper and coal wedges and can be correlated with the initial electron distribution by simulations with the Monte Carlo code GEANT [100]. Since the dimensions of the wedges used were 4 by 10 by 10 mm an angular resolution, $\triangle\theta$, of about 5° was obtained.

It is noted that this tantalum converter is not sufficient to stop electrons with an energy beyond 11 MeV. However, in [48] it was found for the same experimental set-up that the photon yield of electrons beyond 11 MeV, which was generated directly in the copper or coal wedges is by about one order of magnitude lower than the yield generated in the tantalum slab.

The β^+ decay of the activated ^{63}Cu and ^{12}C was measured by standard coincidence techniques in which the simultaneous detection of two counterpropagating 511 keV photons is taken to be due to the annihilation of the positron inside the target. In order to minimize the relative error of this measurement, up to 75 laser shots were accumulated on the same activation targets. Hence, the simultaneous decay during this activation has to be taken into account. Since furthermore only one coincidence detector was available for the measurement of the decay of up to nine of these wedges their initial activity has to be corrected for the different times of their measurements.

7.3.4.1 Accumulated Measurement

An activation process induced by numerous laser shots over a time scale which is comparable to the half-life of the reaction product, $T_{1/2}$, has to be corrected for the simultaneous decay of the activation target. This can be described as a function of time, t, by

$$dN = \dot{Q}dt - \lambda N dt, \tag{7.6}$$

where N is the number of activated nuclei, $\dot{Q}$ the activation rate and λ the decay constant, $\ln 2\, T_{1/2}^{-1}$. Self-explanatory, the same accounts for the counting rate, $\dot{z}$. If the activation process ends after a time T solely the usual exponential decay occurs for $t > T$. Hence,

$$\dot{z}(t) = \dot{z}_\infty\Big(1 - \exp(-\lambda T)\Big)\exp\Big(-\lambda(t-T)\Big). \tag{7.7}$$

Since after a certain time of activation the decay matches the activation rate, only a limited counting rate can be ideally achieved, $\dot{z}_\infty$. Assuming that the subsequent measurement of the radioactive decay starts at t_1, ends at t_2 and gave z_M counts this leads to

$$\dot{z}_\infty = \frac{\lambda z_M}{1-\exp\Big(-\lambda T\Big)} \cdot \frac{1}{\exp\Big(-\lambda(t_1-T)\Big)-\exp\Big(-\lambda(t_2-T)\Big)}. \tag{7.8}$$

Therefore, following this formalism activation processes induced by various number of laser shots and the measurement of several activated targets at different times can nevertheless be compared.

7.3.5 Emittance Diagnostics

One of the aforementioned aims of this experiment was to improve the electron beam quality. This quality is in accelerator physics commonly described by the emittance, which is the area of electron beam distribution in phase space. Since this quantity is according to Liouville's theorem a constant in an isolated volume element it is crucial for any electron source of interest.

7.3.5.1 Liouville's Theorem

Fundamental to all electron beam quantities is the 6D particle distribution function of the coordinates, $\vec{r}$, and momenta, $\vec{p} = \gamma\vec{\beta}m_e c$, given as

$$\Pi(\vec{r},\vec{p}) \equiv \Pi(x,y,z,p_x,p_y,p_z), \tag{7.9}$$

which, physically, is simply the probability of finding a particle at point $(\vec{r},\vec{p})$. This distribution is normalized in the 6D phase space, and, as expected, yields the total charge in the distribution. Its continuity equation reduces for Hamiltonian systems to

$$\frac{d\Pi}{dt} = 0, \tag{7.10}$$

which is the statement that the probability density is a constant for a conservative system. This is commonly known as Liouville's theorem.

7.3.5.2 RMS Emittance

The full probability distribution in Π is rather unwieldy theoretically and at present experimentally inaccessible, motivating a wide variety of abstracted parameters. Least ambiguous of the parameters employed is the vertical 2D sigma matrix,

$$\Sigma_x \equiv \begin{bmatrix} \langle xx\rangle & \langle xx'\rangle \\ \langle xx'\rangle & \langle x'x'\rangle \end{bmatrix} = \varepsilon_g \begin{bmatrix} \beta & -\alpha \\ -\alpha & \gamma \end{bmatrix},$$

which correlates between the coordinates, x, and momenta, x'. The quantities in the second matrix are the Courant-Snyder ellipse parameters already well known to the scientific community, whereas ε_g is the geometrical emittance of this beam distribution [101]. These parameters are implemented for the definition of the normalized vertical root-mean-square (RMS) emittance, $\epsilon_{n,x}^{RMS}$, given as

$$\epsilon_{n,x}^{RMS} = \beta\gamma\sqrt{\langle x^2\rangle\langle (x')^2\rangle - \langle xx'\rangle^2}, \tag{7.11}$$

where β and γ are the usual relativistic electron parameters.

7.3.5.3 Pepper-Pot Method

Experimentally accessible is the emittance by the implementation of the "pepper-pot" method. The experimental set-up used as well as the formalism to derive the electron beam emittance from such data will be described in the following.

Experimental Set-up

The emittance of an electron beam is usually normalized to its relativistic electron parameters, β and γ. As the energy spectrum of the electron source generated in this experiment is expected to be broad the single electron energies need to be dispersed. This was achieved by implementing a secondary magnet, which was installed directly behind the gas jet nozzle, like it is indicated in Fig. 7.5.

Electrons could enter this non-focusing magnet of 5 cm in diameter through two different stainless steel collimators, which resulted in solid angles of 300 and 500 msrad. These collimators served to obtain a reasonable energy resolution whilst taking into account the opening cone as well as the halo of the electron beam. It is additionally

Figure 7.5: Schematic of pepper-pot measurement. The electron beam generated in the gas jet subsequently passed a collimator *(a)* and entered a magnetic field *(b)*. The dispersed electron beam could partially pass through the holes of a pepper-pot mask *(c)* and leave traces on RCF installed behind it *(d)*.

Figure 7.6: Cross section of a beamlet passing through a pinhole of the pepper-pot mask. Descriptions are given in the text.

noted that the separation of the pole pieces of this magnet was sufficient not to cut any part of the electron beam envelope. Hence, single electron energy bins could be regarded separately.

Since the emittance can be seen as the area of the electron divergence distribution as a function of position within the beam envelope, the electron beam envelope was partially masked, solely permitting single electron beamlets at a defined position to pass through (750 ± 100) μm holes, like it is indicated in Fig. 7.6. Such an arrangement is known as a "pepper-pot." Here, lead plates of varying thicknesses were implemented, which were sufficient to stop electrons at the regarded energy bins. These masks were fixed directly next to the magnet and were displaced vertically along the x-axis with a stepping motor and a 5 μm precision, which enabled to scan the entire electron beam envelope. For any of the pepper-pot mask positions, 150 shots were performed.

The electron beam passing through these holes was visualized at various distances behind the mask with RCF, which has a spatial resolution below 10 μm [79] and which was scanned with the same resolution directly after the experiment. To avoid illumination of the RCF by the laser beam it was shielded with aluminum wrapping. Scattering of electrons within these thin foils of 25 μm thickness can be corrected as it was presented above in Chapter 7.3.3. It is noted that the influence of bremsstrahlung, which resulted in a low and homogenous background on the exposed film, could be easily distinguished by the clear electron traces on the RCF.

The emittance was only determined in the x-axis, i.e., perpendicular to the floor of the experimental hall, since any other direction would be corrupted by the large energy spread of the electron beam.

Calculation of Emittance

The area and the shape of the electron beam in phase space is calculated through measurements of the position and size of the beam spots. Figure 7.6 shows a schematic

cross section which depicts a beamlet passing through such a pinhole, drifting a distance L and striking the RCF. The inclination of the dashed line, which connects between the pinhole center, S, and the beam spot center, S_z, permits to derive the spread of the divergent angle of the beam, $\triangle x'$, which is simply due to the transformation of the phase space along the electron propagation axis from the pepper-pot mask to the RCF. Consequently, the relation

$$\begin{aligned} D_z &= x_{max} - x_{min} \\ &= D\frac{S_z}{S} + L\triangle x'. \end{aligned} \tag{7.12}$$

can be found. From the measured values for D, D_z, L and S_z/S it is therefore possible to determine $\triangle x'$. Tracing the latter as a function of the position within the beam envelope, $\triangle x'(x)$, the vertical beam emittance in (π mm mrad) is obtained as $1/\pi$ times this phase space area [102].

In the analysis, the peak on the x-axis of the scanned RCF was regarded as the center of the electron beam, whilst D_z was the standard deviation of the Gaussian fit of the measured traces. The error in $\triangle x'$ was determined by the accuracies of $D_z, DS_z/S$ and L and was typically of the order of 20 %.

Detection Limits

Ideally, the emittance is the distribution of all electrons in phase-space. However, single electrons can not be measured with RCF, since its sensitometric response is limited, as can be seen in Fig. 7.7. Thus, it is important to compare the measured

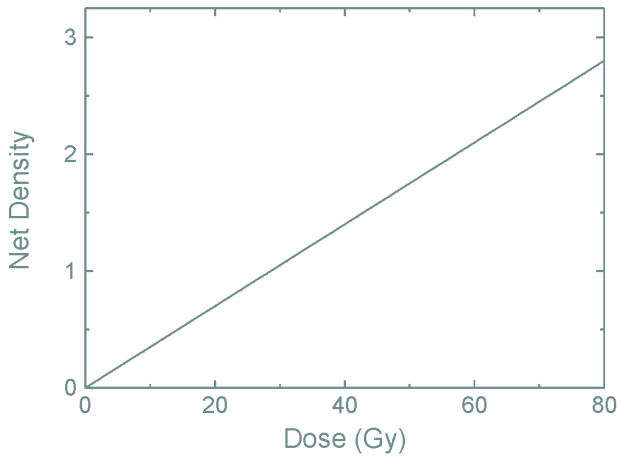

Figure 7.7: Sensitometric response of MD55 radiochromic film [79].

optical density of the scanned RCF to the computed number of accelerated electrons in the energy bin of interest. This permits to determine the fraction of the detected electrons and deciphers the importance of the electron beam halo.

Chapter 8

Experimental Results and Simulations

In the following the results on the electron beam characterization will be presented, whereas the electron energy gain as well as the electron beam quality will be regarded in detail. Comparison with the transmitted laser beam as well as 3D Particle-In-Cell simulations indicate that the interaction occurred in a new acceleration regime, which will finally be termed "Forced Laser Wakefield."

8.1 Electron Spectra and Yield

8.1.1 Experimental Result

The resulting electron spectrum for a neutral plasma electron density, n_e, of 2.5×10^{19} cm^{-3} is shown in Fig. 8.1. Although it is possible to fit to the lower energy

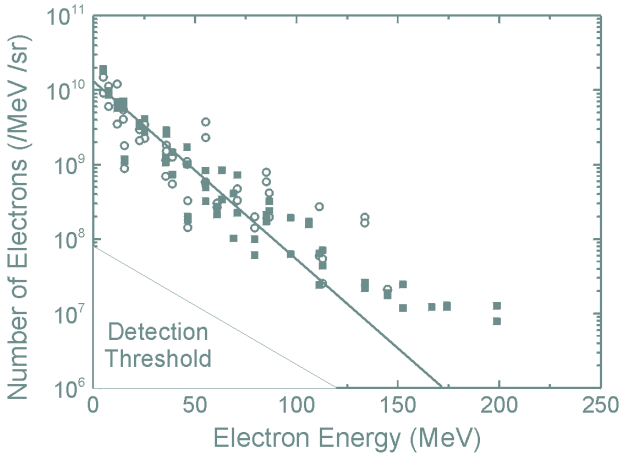

Figure 8.1: Electron energy spectra for neutral plasma electron densities of 2.5 (squares) and 6×10^{19} cm^{-3} (light circles) and a laser irradiance of 3×10^{18} W/cm^2. An effective longitudinal electron temperature of (18 ± 1) MeV is obtained from the exponential fit for electrons of less than 130 MeV (continuous line). A total beam charge of about 5 nC was obtained.

electrons a relativistic Maxwell-Jüttner distribution, which results in an electron temperature of (18 ± 1) MeV for electrons of less than 130 MeV, this description is not adequate to describe the higher energy electrons. A significant number of electrons exist in a "hot tail" that extends beyond 200 MeV. At this electron density the cold wavebreaking limit, E_{WB}, is 3.8 E_{max}, and the maximum energy that an electron can gain in relativistic plasma waves at such an amplitude is slightly greater than 250 MeV. This indicates that the relativistic plasma wave excited by the short laser pulse does indeed reach an amplitude close to the wavebreaking limit, which is consistent with the absence of thermal effects in this regime.

At a higher electron density of 6×10^{19} cm^{-3}, similar spectra have been observed in yield and temperature, but without the hot tail as it is also indicated in Fig. 8.1. The plateau extending to 200 MeV has only been obtained for densities between 2.5 and 4.7×10^{19} cm^{-3}.

The total beam charge was determined to be about 5 nC and showed little dependance on the neutral plasma electron density. This indicates that the spectra shown in Fig. 8.1 are mainly dominated by low energy electrons.

8.1.2 Comparison with 3D PIC Simulation

The numerical modelling of these electron spectra was done using the 3D Particle-in-cell (PIC) code CALDER. This code includes a "moving window" capability, i.e., the simulation box moves with the laser pulse, thus enabling simulations with realistic parameters to be carried out, such as a 15 μm focal waist and a 1 mm long plasma at a density of 1.2 % n_c. This calculation features more than 6×10^8 electrons and as many ions moving through a mesh with 1.5×10^8 cells. It was run on 500 nodes of the TERA supercomputer at CEA/DIF.

The laser pulse is injected into the plasma as a 30 fs FWHM Gaussian pulse with a peak irradiance of 3.5×10^{18} W/cm^2. The simulation indicates that strong transverse self-focusing takes place in less than 300 μm inside the plasma, resulting in an order of magnitude increase in the pulse intensity. The strong ponderomotive force of this "light bullet" pushes electrons out of its path, driving a large plasma wave in the wake of the pulse, as it is shown exemplary in Fig. 8.2.

After 210 μm, the electron density modulation and wake field have a relatively regular structure, with a maximum electric field of 1 E_{WB}, or 430 GV/m as it is shown in Fig. 8.3. This is a factor of 4 below the wavebreaking limit at this density. Some electrons have already been accelerated in this field to a maximum energy of 20 MeV.

As it can already be seen in Fig. 8.2, in the next 350 μm of propagation, the plasma wake and electron density evolve markedly. A large concentration of electrons is observed on axis, one half plasma period behind the laser pulse, resulting in a density increase much larger than the background plasma density, $\delta n_e/n_e \gg 1$. The wakefield

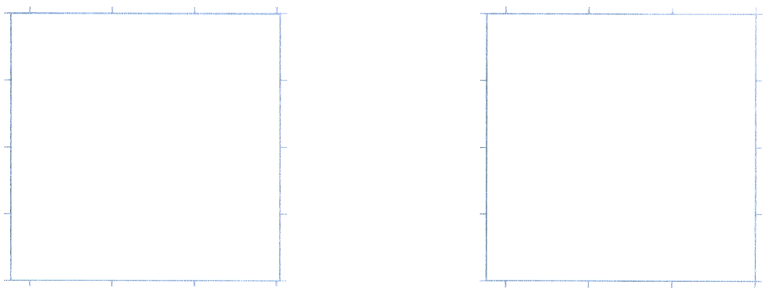

Figure 8.2: Electron density (left) and laser intensity (right) in plasma.

amplitude grows close to the wavebreaking limit, reaching 3.2 E_{WB}, or close to 1.4 TV/m, as it is also indicated in Fig. 8.3.

The maximum electron energy rapidly increases, reaching 235 MeV after 560 μm of propagation in the plasma. Most of the accelerated electrons are located between 550 and 560 μm, in the density dip created by the pulse. The electron spectrum does not evolve substantially later on. The guided pulse propagation is sustained until the end of the simulation, at 900 μm, but the plasma wave loses some of its coherence, and its

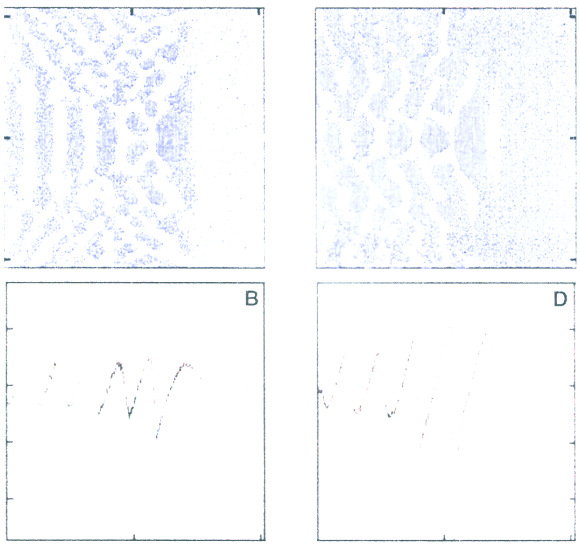

Figure 8.3: Electron density cuts along the vertical laser plane and electric fields along the laser axis after propagation through 210 μm ((A) and (B)) and 560 μm ((C) and (D)). In (C), the density scale has been truncated to 0.06 n_c, which is five times the background density. In (D), the on-axis electric field of the plasma wave almost reaches the wavebreaking value of 4 E_{WB}.

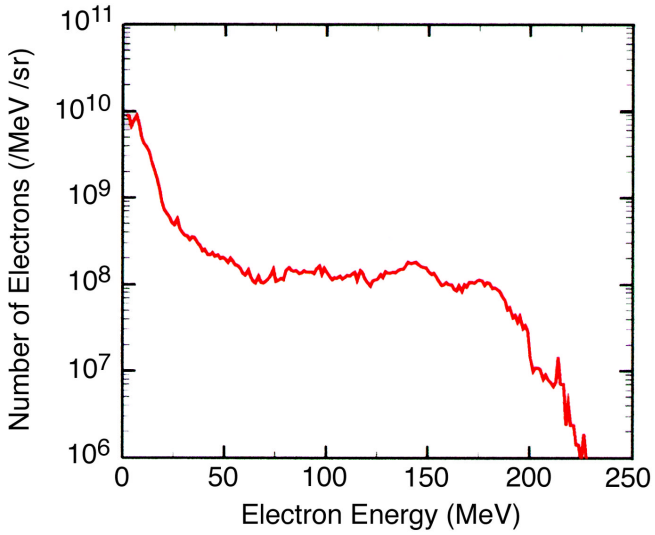

Figure 8.4: Calculated electron energy distribution after propagating 900 μm through the plasma. This spectrum is measured inside a 2° half-angle cone along the laser axis, which is the angular resolution of the code diagnostic.

amplitude is reduced. Half of the incident laser energy is transmitted through the first 900 μm of plasma.

The energy distribution of electrons along the laser direction at this point shown in Fig. 8.4 is essentially identical to the spectrum at 560 μm. Counting all the particles above 1.25 MeV, an average electron energy of 11 MeV, a total beam energy of 6.4 mJ, i.e. slightly more than 1 % of the incident laser energy, and a beam charge of 0.6 nC is obtained. The difference between the measured and computed beam charge reflects the low energy electron contribution to the ICT measurement. Interestingly, the most energetic electrons are found to have a greater relative transverse component of their momenta. This is because, as they "out-run" the plasma wave, they are no longer influenced by its focusing effect, and so can gain transverse momentum from radial electrostatic and electromagnetic fields.

Finally, it is worth noting that although 2D PIC simulations qualitatively show the same phenomena, they fail to correctly describe the self-focusing of the laser pulse and the maximum electron energy. All attempts to model this experiment with 2D simulations show a deficit by more than 50 MeV in the maximum electron energy, which was experimentally observed to be greater than 200 MeV.

In conclusion, consistent with other results [103], this 3D simulation clearly indicates that relativistic plasma waves can be efficiently driven to wavebreaking in a regime where the pulse length is of the order of the plasma period, i.e., where the resonance condition for classical wakefield acceleration is not met. Obviously, this can be experimentally demonstrated by measurements of the transmitted laser beam, since this can not show any signature of laser energy cascading to satellites frequencies, as it is known from the SMLWF regime.

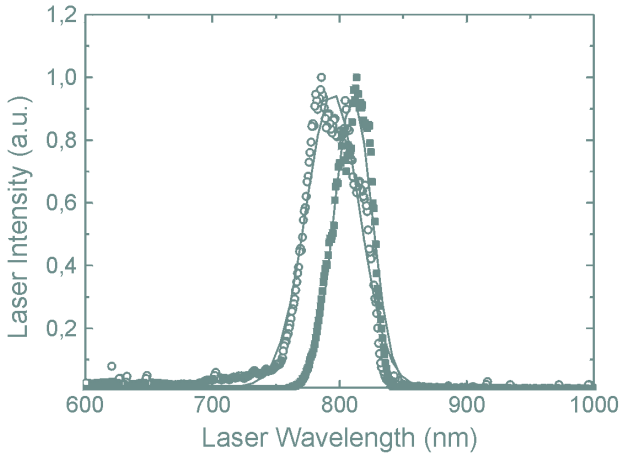

Figure 8.5: Normalized transmitted laser spectra in vacuum (squares) and in the plasma (light circles) for shots at full laser energy with an irradiance of 3×10^{18} W/cm^2 and a plasma electron density of 2.7×10^{19} cm^{-3}. Note, the broadening of the spectrum.

8.2 Transmitted Laser Beam

The transmitted laser intensity in vacuum and plasma for shots at full laser energy and a plasma electron density of 2.7×10^{19} cm^{-3} is presented in Fig. 8.5. Their FWHM is obtained from a Gaussian fit and reveals the initial pulse spectrum to be 33 nm whereas the plasma-distorted pulse is 48 nm. Hence, the transmitted spectrum got broader.

As it was observed in the 3D PIC simulation, the front of the laser pulse pushes electrons forward, while the rear propagates in the density depression of the plasma wave. Consequently, the back of the pulse propagates faster, v_{gb}, than its front, v_{gf}, compressing it to an optical shock. Formally, this change in pulse length, $\triangle c\tau_0$, was in [104] expressed as

$$\begin{aligned} \triangle c\tau_0 &= (v_{gf} - v_{gb})\triangle ct \\ &= \simeq -\frac{\omega_p^2}{\omega_L^2}\delta\triangle ct. \end{aligned} \tag{8.1}$$

The resulting amplification of the ultra-short pulse, in particular the formation of an extremely sharp leading edge, can drive a plasma wave beyond its wavebreaking limit. In this case, there can be no spectral cascading of laser energy, and the only signature in the transmitted laser spectra will be a broadening of the driver laser frequency bandwidth, which can indeed be seen in Fig. 8.5.

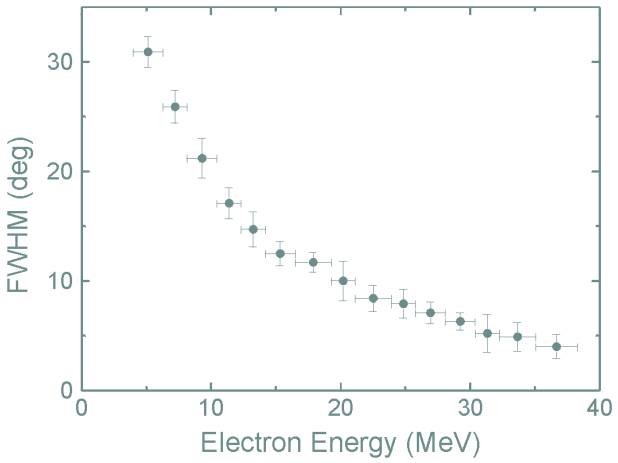

Figure 8.6: FWHM of the angular distribution of the electron beam as measured with the RCF and copper stack. Multiple scattering of the electrons inside this stack and superposition of the individual signals have been corrected.

8.3 Electron Angular Divergence

8.3.1 Measurement with RCF and Copper Stack

The FWHM of the angular distribution of the electron beam as a function of energy is shown in Fig. 8.6. Interestingly, the high energy part of the beam is observed to be well collimated, whereas the low energy electrons are accelerated in a much broader cone in the forward direction. These traces on the RCF indicate a Gaussian electron beam profile, which is in good agreement with the numerical modelling, as it predicts a FWHM of 4° for 30 MeV electrons. However, there is a disagreement for electrons with an energy below 20 MeV, which appear in the 3D PIC simulation to be better collimated than the experiment revealed. This is likely to be due to the "moving window" capability of the code CALDER, which only considers the laser plasma interaction within the laser pulse length, $c\tau_0$. Thus, electrons and their movement way behind the laser pulse are neglected. However, it might still be possible that these electrons are accelerated to some MeV. Another possibility might be that the modelling of this interaction is limited to a fraction, w_0, of the laser focal spot [105].

It is noted that this angular distribution measurement solely extends to an energy of up to 37 MeV as it was accumulated over several laser shots. As RCF has a limited sensitivity and as bremsstrahlung generated in this stack induced (γ, n) reactions and, consequently, radioactive nuclei in the single copper pieces, radiation protection had to be obeyed, which limited the number of possibly accumulated shots. However, such an activity is wanted for the following activation measurements.

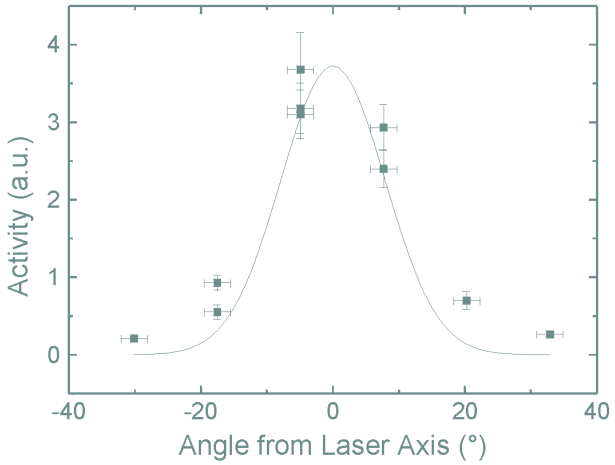

Figure 8.7: Angular electron distribution measured by the nuclear activation of ^{63}Cu, which has a (γ, n) threshold of 9.7 MeV. The FWHM of $(18 \pm 1)°$ is obtained from a Gaussian fit.

8.3.2 Activation Measurement

This observation of the collimation of the electron beam as a function of its energy is in qualitative agreement with (γ, n) activation of copper and coal wedges, which were installed in a circle behind the gas jet nozzle and a tantalum converter.

Figure 8.7 shows the measured relative ^{62}Cu activity of the used copper wedges. Assuming a Gaussian angular distribution for the electron beam and bremsstrahlung, which is supported by the data obtained with radiochromic film, the FWHM of the angular distribution beyond 9.7 MeV was measured to be $(16 \pm 1)°$. Performing the same measurement with ^{12}C instead, which has a reaction threshold of 18.7 MeV, revealed a FWHM of $(10 \pm 1)°$. This compares favorably with the data shown in Fig. 8.6 and the 3D PIC simulation.

It is noted that the nuclear activation measurement presented here is a qualitative comparison only, since the measured angular distribution of the γ-spectrum was not correlated with the initial electron spectrum. However, it supports clearly all of the obtained results.

8.4 Emittance

This low angular distribution of the electron beam might also conjecture a low emittance, which was experimentally and numerically determined with the pepper-pot method.

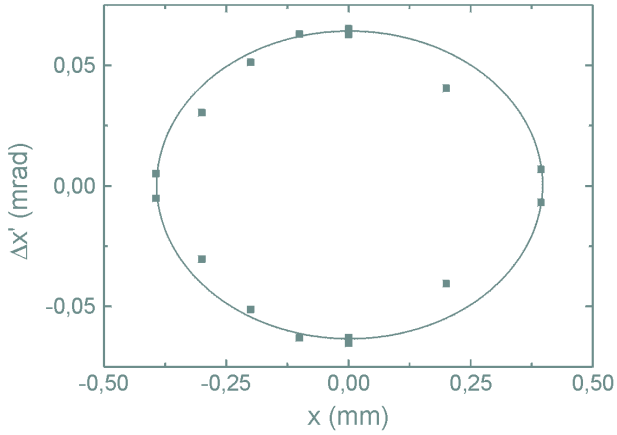

Figure 8.8: Spread of the divergent angle, $\triangle x'$, versus pinhole position, x, for (54.9 ± 2) MeV electrons. The dots mark the maximum of the error bars. The normalized emittance is calculated from this plot to be $(2.7 \pm 0.9)\,\pi$ mm mrad for xx % of the total beam charge in this energy bin.

8.4.1 Measurement with Pepper-Pot Diagnostic

Figure 8.8 shows the experimentally determined spread of the electron beam divergent angle, $\triangle x'$, versus the height of the pepper-pot mask, x, relative to the center of the laser beam axis for (54.9 ± 2) MeV electrons. Normalizing the area of this distribution to the relativistic electron beam parameters, β and γ, allows to derive the vertical normalized emittance, $\epsilon_{n,x}$, which is here found to be $(2.7 \pm 0.9)\,\pi$ mm mrad. Tracing these values in Fig. 8.9 for a wide range of electron energies it was obtained that the emittance decreases for increasing electron energies, similar to the result obtained with the RCF and copper stack.

However, and as it was mentioned in Chapter 7.3.5.3, it is important to understand which dynamical range was underlying this measurement, i.e., how many of all the electrons within the investigated energy bin were actually detected. This crucial aspect was deciphered with numerical calculations for the 2D phase space.

8.4.2 Comparison with Numerical Modelling

THIS NUMERICAL MODELLING OF THE ELECTRON BEAM EMITTANCE IS STILL UNDER CONSIDERATION. UNFORTUNATELY, THE FINAL 3D SIMULATIONS WERE NOT DONE BEFORE THE DEADLINE TO HAND IN THIS MANUSCRIPT. HENCE, I WILL SEND THIS SUBCHAPTER ON THE RESULTS DIRECTLY TO YOU ASAP.

THEY WILL THEN INCLUDE

- CALCULATED PHASE SPACE FOR SINGLE ELECTRON BEAM ENERGIES

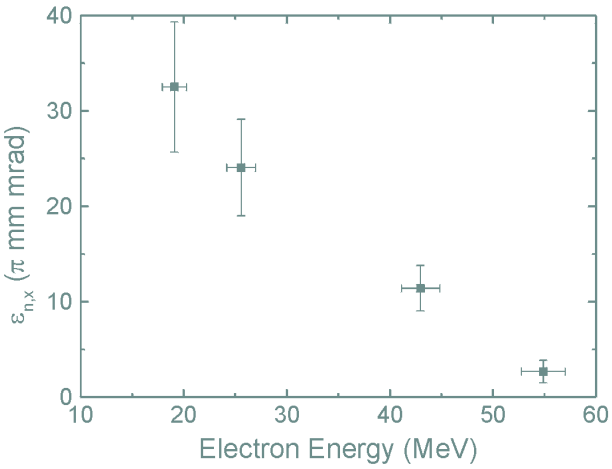

Figure 8.9: Normalized vertical emittance, $\epsilon_{n,x}$ as a function of electron energy. As the error bars indicate, the lower energy electrons get accelerated with a higher statistical fluctuation.

- CALCULATED EMITTANCE, AS IT WAS DONE IN THE EXPERIMENT
- CALCULATED RMS EMITTANCE
- DISCUSSION

PRELIMINARY RUNS HAVE ALREADY SHOWN THAT IT IS INDEED POSSIBLE TO MODEL THIS EXPERIMENT NUMERICALLY. THUS, THE STATEMENT AS WELL AS THE MEANING OF THE MEASUREMENTS PRESENTED HERE ARE NOT AFFECTED. I AM INDEED SORRY ABOUT THIS INCONVENIENCE. SF

8.5 Bunch Length Calculations

As for this experiment the laser pulse duration, $c\tau_0$, was of the order of the plasma wavelength, λ_p, the self-modulation of the laser envelope as the acceleration mechanism is ruled out. Due to this short laser pulse duration one might conjecture that only a single electron bunch is accelerated, with a bunch duration of the order of tens of fs. This was evaluated with 3D kinetic simulation with the PIC code CALDER.

As the plasma wave generated in this experiment suffered strong wavebreaking and accelerated electrons up to 200 MeV, it is also rapidly damped after its first accelerating extremum. As a result these simulations showed that there is little or no wavebreaking for the plasma wave oscillations behind the first extremum, so that the hot electron population is very localized in space.

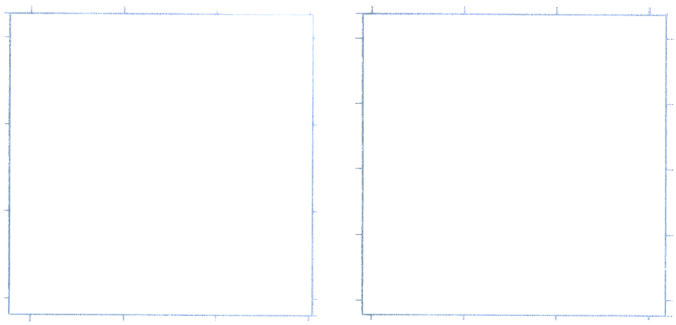

Figure 8.10: Electron phase space on the laser beam axis after two different propagation distances in the plasma.

After 320 μm inside the plasma, electrons above 30 MeV are all concentrated in a bunch less than 5 μm (17 fs) long, as it can be seen in Fig. 8.10. At 550 μm, the next two plasma wavelengths have also accelerated electrons above 30 MeV, so that the 30-plus MeV bunch now extends over roughly 25 μm. However, only in the first plasma wavelength are electrons accelerated above 50 MeV. The 50-plus MeV bunch duration at that point is less than 10 μm (33 fs). At 910 μm, it has spread somewhat more, but still extends over less than 20 μm (67 fs). This bunch lengthening cannot be explained by time-of-flight arguments: The spread between free-streaming 400 $m_e c$ and 100 $m_e c$ electrons over that distance only accounts for $2 \times 10^{-2} \mu$m. Actually, it results from the propagation speed difference between the energetic electrons, travelling very close to the speed of light, c, and the accelerating structure, moving at $0.97c$. Electrons accelerated inside the wake plasma wave, behind the laser pulse, progressively catch up with it and eventually preceed it, so that the bunch duration grows as it propagates. Hence, it appears that in the FLWF regime only one spatially very localized electron bunch is generated, which is a severe difference to the SMLWF scheme.

In conclusion, the experimental results and their numerical modelling have shown that in the newly described "Forced Laser Wakefield" regime electrons can be efficiently accelerated beyond an energy of 200 MeV. Since it appears that only one cycle of the plasma wave was driven to wavebreaking, one might conjecture that a single high energy electron bunch is generated. Interestingly, this electron bunch is highly collimated and can be characterized by an emittance which is indeed comparable to accelerators'. This makes the FLWF scheme potentially valuable, which is why it will be discussed in detail in the following chapter. Subsequently, several interesting and unique applications will be suggested.

Chapter 9

Forced Laser Wakefield Regime

In the previous chapter experimental and numerical evidence was presented, which clearly indicate that relativistic plasma waves can be efficiently driven to wavebreaking, even though the resonance condition for classical wakefield acceleration is not met. Reducing the laser pulse length to $\tau_0 \sim 2\pi\omega_p^{-1}$, decreasing the laser energy by more than a factor of 25 compared to the above mentioned experiments in the SMLWF regime, and, thus, retaining a similar laser power also leads to wavebreaking, i.e., the generation of an energetic electron beam. This new regime is termed "Forced Laser Wakefield" (FLWF).

Here, a combination of laser beam self-focusing, front edge laser pulse steepening and relativistic lengthening of the plasma wave wavelength can result in a forced growth of the wakefield plasma wave, even for initially non-resonant laser pulses, $\tau_0 \neq \pi\omega_p^{-1}$. Since in the FLWF regime the interaction of the bunch of accelerated electrons and the plasma wave with the laser is reduced, this can yield higher electron energy gains beyond 200 MeV as well as better beam quality.

Indeed the maximum energy of detected electrons is significantly greater, suggesting the growth of plasma waves with peak amplitude greater than the initial plasma density. Because in this regime, the interaction of the plasma wave and the electrons trapped by it with the laser pulse is minimized, the electron beam is found to have improved quality compared to that produced in the SMLWF regime. Also improved is the shot-to-shot variation, although the electron charge for a given energy does typically vary by a factor 2 to 3. This is a considerable improvement on the SMLWF experiments where this can be greater than an order of magnitude [106]. This is likely to be because the FLWF is less dependent on fast growth of instabilities from noise sources, as it was shown in Chapter 2.2.1.1.

Transmitted laser spectra in the FLWF regime solely show their broadening and, noticeably, a complete absence of satellites. Evidently the pulse is not modulated at the plasma frequency, though it is likely to have experienced a compression. This might be due to the nonlinear interaction of the rising edge of the pulse with the plasma wake pushed in front of the laser pulse by its ponderomotive force. The growing plasma wave retards the very front of the laser pulse so compressing it. This optical compression in conjecture with the nonlinear wavelength increase of the plasma wave as the amplitude increases can result in a highly efficient growth of the plasma wave even in the case where the laser pulse length is initially longer than the plasma period.

The main features of this nonlinear wakefield generation by such an ultra short pulse are demonstrated through the use of PIC simulations. Using the code OSIRIS with the experimental parameters, though generating a large amplitude wakefield in a 1D description, never exhibits wavebreaking [107]. Additionally a measurable amount of light is trapped in front of the sharp edge and is gradually redshifted as it loses energy to the plasma wave. Experimentally, there is no appreciable redshifted component to the transmitted light. Indeed the whole pulse appears to be blueshifted.

In the 3D simulations presented earlier, despite being in the short pulse regime, $\tau_0 \sim 2\pi\omega_p^{-1}$, self-focusing of the laser energy is observed. This can explain how the intensity can be sufficiently high for an impulsive plasma wave growth to wavebreaking amplitude, despite the fact that neither the initial laser intensity nor the observed pulse compression are sufficiently large. At lower densities, including at the wakefield resonant density, $\tau_0 = \pi\omega_p^{-1}$, no accelerated electrons are observed at all. This is a subtle difference between the FLWF and nonlinear wakefield regimes. Without self-focusing, no wavebreaking is observed, but this can only happen if the laser pulse length is not below $\pi\omega_p^{-1}$. But if there is self-focusing then pulse erosion takes place, which can allow efficient wake generation. Since the very front of the laser pulse is not self-focused, the erosion will be more severe, explaining why the redshifted edge seen in the 1D simulations is not observed in the experiment. In fact, ionization, which is not included in this model, further enhances this effect by increasing diffraction of the front of the pulse. The wake then is mostly formed by this fast rising edge, and the back of the pulse has little interaction with the relativistic longitudinal oscillation of the plasma wave electrons. Indeed the increase of plasma wave wavelength due to relativistic effects means that the breaking and accelerating peak of the plasma wave sits behind most, if not all, of the laser pulse. Hence, its interaction and that of the accelerated electrons with the laser pulse is minimized, thus reducing possible emittance growth.

Also observed in the 3D simulations is that the radial plasma wave oscillations interact coherently with the longitudinal field, so enhancing the peak amplitude of the plasma wave. This coupled with the aforementioned strong self-focusing are ingredients absent from 1D treatment of this interaction. Even in 2D simulation, it is not possible to observe electrons beyond 200 MeV, as measured in the experiment, since except in 3D simulations, both the radial plasma wave enhancement and self-focusing effects are underestimated. Hence it is only in 3D simulations that E_{WB} can be reached. That such large electric fields are generated, demonstrates another important difference between the FLWF and SMLWF regimes, since in the latter, plasma heating by instabilities limits the accelerating field to an order of magnitude below the wavebreaking limit.

Chapter 10

Applications and Conclusions

In this chapter possible applications of this unique electron source will be regarded. Its direct implementation as an injector for contemporary accelerator physics will be discussed, as well as an example for its use in current quests in radiation chemistry. Additionally, its feasibility to generate secondary X-rays via the channelling effect and Thomson scattering will be examined.

10.1 Electron Source

10.1.1 Injector for Conventional Accelerators

Conventional accelerators typically provide energetic electron bunches with a pulse duration in the ps order and an energy resolution, $\triangle W_e/W_e$, of less than 10^{-3}. To achieve these performances, such devices are precisely designed and, hence, for a fixed electron energy only.

Even though this high energy resolution is not met in the FWLF scheme, it enables to select an arbitrary energy bin out of the entire spectrum of up to 200 MeV. As it was shown in Chapter 8, this can deliver low emittance, ultra short and single electron bunches. A possible set-up for this approach is presented in Fig. 10.1, where a magnetic

Figure 10.1: Possible configuration to use the FLWF as an injector for accelerators. The electron beam escaping the gas jet *(a)* is dispersed in a magnetic field *(b)* and focused with solenoids *(c)* before injection or transport to an experiment.

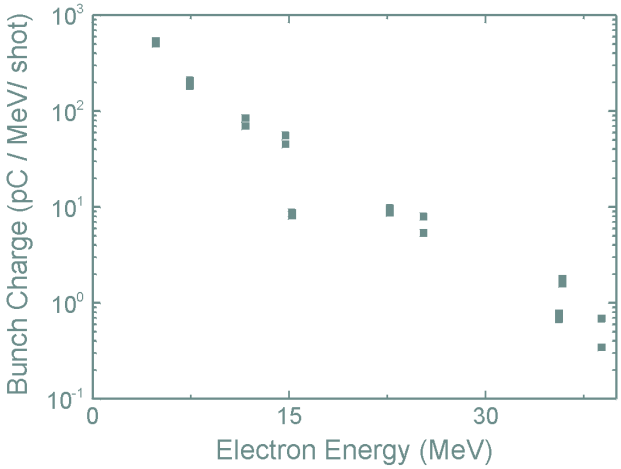

Figure 10.2: Bunch charge spectrum obtained in the FLWF regime. This spectrum ends at 37 MeV as this was the experimental limit of detection for the opening cone of the electron beam.

field behind the gas jet disperses the single electron energies. Additional solenoids and further electron beam optics can be implemented to adapt the beam envelope before injection or transport to an experiment. Hence, this laser produced electron source allows to make experiments over a wide range of electron energies.

10.1.1.1 Bunch Charge

It is essential to know which electron bunch charges can be obtained per laser shot by selecting one arbitrary energy bin out of the entire spectrum. Figure 10.2 shows the convolution of the measured electron yield and its angular distribution presented above in Chapter 8. As can be seen the bunch charge of high energy electrons does not compare so far to accelerators', which typically operate at several pC and even nC. Additionally, peak electron currents of about 10 A for 45 MeV electrons are not competitive, even though this quantity is favored by the ultra short bunches.

However, simulations for a 12 J, 33 fs laser pulse interacting with an underdense plasma suggest that a large beam charge increase could be obtained in an improved mode of the FLWF regime, where the laser pulse is substantially shorter than the plasma wavelength and propagates inside a solitary plasma cavity [103]. In this case, the distribution of the accelerated electrons is no longer Maxwellian but shows a clear peak with charges as high as, say, 5 nC at (300 ± 25) MeV.

Up to now, this "broken wave" regime cannot be experimentally verified, since such challenging laser systems do not currently exist. Nevertheless, they are already today an issue for laser development.

10.1.1.2 Benefits and Discussion

Obviously, the FLWF shows some flexibility in terms of the experimentally required electron energy. The simple implementation of a magnet yields low emittance and ultra short electron bunches over a wide range of energies – a feature usually not possible at conventional accelerators. Additionally, and in contrast to the SMLWF scheme, the FLWF delivers a single electron bunch, which might be easier to inject and synchronize with today's radio frequency cavities. Finally, it was already demonstrated that there are no theoretical limits to increase the peak current of high energy electrons, which might make this compact and tunable electron source an alternative for high energy injectors.

However, it must also be noted that this approach suffers from a large background, when only small fractions out of the broad energy spectrum with a total charge of 5 nC are selected. Dumping an important part of this electron beam in a Faraday cup consequently leads to bremsstrahlung, which might be a concern for experimental data acquisition as well as radioprotection.

In contrast, if a high energy resolution is not required for an experiment, such a laser produced electron source clearly benefits from its ultra short bunches, which permit to carry out pump-probe experiments with a sub-ps temporal resolution. In the following such an experiment in ultra rapid chemistry will be briefly presented.

10.1.2 Ultra Fast Radiation Chemistry

Radiation chemistry deals with damages of ionizing radiation on chemical and biological media, e.g., the energy transfer of energetic electron pulses to water molecules. Here, their physicochemical interaction concerns electron ejection, thermalization, hydration and the ultra fast positive hole reaction (H_2O^+) with adjacent water molecules. Such studies are nowadays routinely carried out on conventional photo-injectors, which operate with electron bunch lengths of several tens of ps [108].

10.1.2.1 Interest

However, these devices limit the real-time experimental observation of such ultra rapid radiolytic events, whose domain of research was recently termed "Femtolysis" [109], as, e.g., the positive hole reaction is assumed to occur in less than 100 fs [110]. Here, the ionization induced by an energetic electron yields hydrated electrons (e^-_{aq}), strong oxidants (OH radicals), hydronium ions (hydrated protons, H_3O^+) as well as molecular products, such as H_2 and H_2O_2. These secondary, hydrated electrons, e^-_{aq}, correspond to an excess electron stabilized by several water molecules. Due to partial recombination with their OH^- and H_3O^+ neighbors in nascent confined spaces (spurs), their escape probability can be significantly influenced on the sub-ps time scale :

$$\mathrm{nH_20} \xrightarrow[\text{(fs)}]{\text{electrons}} \left\langle \mathrm{e^-_{aq}}, \mathrm{OH}, \mathrm{H_3O^+} \right\rangle_{\mathrm{Spurs}} \xrightarrow[\text{(ps)}]{\text{part.recombination}} \left\langle \mathrm{OH^-}, \mathrm{H_3O^+} \right\rangle_{\mathrm{Spurs}}$$

Continuous experimental and theoretical efforts are directed towards understanding these elementary physicochemical properties [111, 112]. As the quantum character of this molecular hydrogen precursor greatly determines oxidoreduction reactions in irradiated water, the early fate of hydrated electrons in nascent spurs is of particular relevance. However, it has never been observed in real time, and, up to now, its best estimates of radiolytic events are in the 30 to 100 ps range [113].

Obviously, electrons produced by relativistic laser plasma interactions could serve for these studies, since their bunch length is of the order of the laser pulse length, as it was mentioned above. Thus, implementing a 30 fs FWHM laser, a sub-ps time resolution could be experimentally obtained, which could lead to a better understanding of such ultra rapid physicochemical events.

10.1.2.2 Pump-Probe Experiment

Experimentally accessible is the generation of these hydrated electrons in water, $\mathrm{e^-_{aq}}$, due to their $1s \rightarrow 2p$ transition, which results in the absorption of light with a wavelength, λ_L, of 820 nm. Hence, the benefit that laser produced ultra short electron bunches are additionally synchronized with laser pulses, permits to carry out a pump-probe experiment, like it is indicated in Fig. 10.3.

This experiment was performed on the aforementioned "salle jaune" laser, operating at 10 Hz and a wavelength, λ_L, of 820 nm. The laser delivered on target energies of 960

Figure 10.3: Sketch of experimental set-up for Femtolysis experiment. The pump laser beam generated electrons in a gas jet *(a)*. To suppress the influence of electrons below an energy of 2.5 MeV, a 1 mm thick copper piece was used as a filter *(b)*. Subsequently, the electron pulse passed through a suprasil cell containing pure liquid water *(c)*. Their interaction was probed with 30 fs FWHM laser pulses under 90°, whose transmission was recorded onto a 18-bit CCD camera *(d)*.

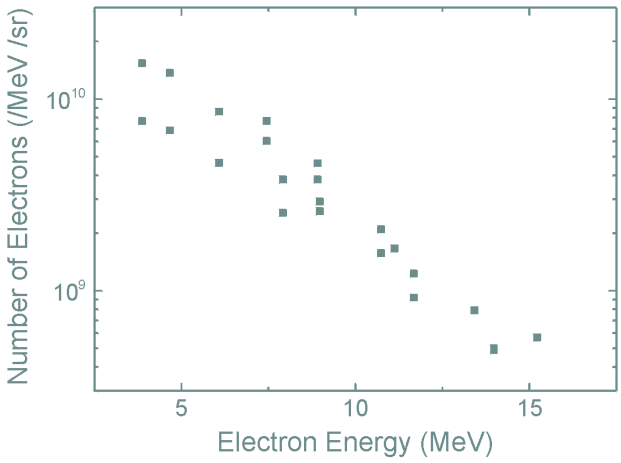

Figure 10.4: Electron spectrum for Femtolysis experiment, which was measured in the same way as described in Chapter 7.3.

mJ in 30 fs FWHM laser pulses. The pump laser beam was focused with a $f/6$ off-axis parabolic mirror onto the sharp edge of a 2 mm diameter supersonic helium gas jet. The laser distribution at full energy in the focal plane was a Gaussian with a waist, w_0, of 6 μm containing 50 % of the total laser energy. This produced vacuum-focused intensities on the order of 2.7×10^{19} W/cm^2. The initial plasma electron densities was about 1×10^{20} cm^{-3}, which was achieved by changing the backing pressure on the gas jet. The hereof generated electron beam was characterized in precisely the same way as described in Chapter 7.3.

As can be seen in Fig. 10.4, these deliberately chosen experimental parameters resulted in a maximum electron energy of up to 15 MeV. This is of particular interest since the stopping power in water for this energy range does not show any great dependance on electron energy. Consequently, this simplifies the subsequent analysis.

It is evident, that these experimental parameters did not meet the aforementioned conditions for the FLWF regime. However, the in this SMLWF scheme generated ultra short train of electron bunches did not affect the investigation carried out in this study. Note, that the aim of the work presented here is to elucidate the unique temporal benefits of laser produced electron bunches, which are synchronized with laser pulses.

The probe laser beam, also at a wavelength of 820 nm and a FWHM pulse length of 30 fs, was not focused and had therefore an energy flux below 10^{-3} J cm^{-2}. This precaution avoided any excitation of the water sample. Synchronization of the pump and the probe laser beam with a 30 fs precision was achieved by shadowgraphy of the plasma created by the pump laser beam in the gas jet. This arrangement resulted in a very accurate synchronization and was free of any jitter.

Figure 10.5: Short-time dependence of measured optical density magnitude at 820 nm for the irradiation of pure liquid water at 294 K with a sub-ps electron beam (circles). An instrumental response is determined with two Lorentzian profiles of 700 and 100 fs FWHM for the relativistic electron beam and the optical probe respectively. The continuous line represents the best computed fit of a non-instantaneous Femtolysis signal rise time.

The measurements were performed 5.5 mm downstream from the helium gas jet and at 1 mm depth in the 10 by 10 mm suprasil cell. At this distance, the electron beam diameter was found to be (2.5 ± 0.5) mm, which was deduced from its angular divergence. Consequently, the electron beam had a mean luminosity of $(9.5 \pm 0.3) \times 10^{10}$ e^- cm^{-2}.

The absorption of the probe laser beam inside the water was recorded for a well given pixel position onto a 18-bit CCD camera. These optical absorption measurements were alternatively performed with and without the laser pump beam. Self-explanatory, changing the time delay between the pump and the probe beam with a sub-ps accuracy permitted to determine the interaction at high temporal resolution, which is well above what is attainable at conventional accelerators. Finally, to avoid statistical fluctuations, these transmission signals were averaged over several measurements to a mean value.

10.1.2.3 Experimental Results

Figure 10.5 shows the measured signal for pure water. Clearly, the instrumental response exhibits a non-instantaneous rise time. Its dynamics was analyzed with a model for which secondary electrons slow down, become hydrated and follow early recombination processes in nascent aqueous spurs. Considering previous time resolved investigations of low energy electron hydration in aqueous environments, the physico-chemical events of these electrons are defined by a two stage process : a trapping

step (pre-hydration) and a non-radiative relaxation (hydration), with the characteristic times of 850 and 150 fs respectively, since the optical density magnitude at 820 nm indicates an apparent maximum at 3.5 ps [114].

It is clear, that this time resolution was only possible due to the sub-ps electron bunch length, which is provided at high flux by relativistic laser plasma interactions. Thus, these electron bunches can indeed be implemented to study ultra rapid events in various and different scientific domains.

10.2 Feasibility as X-Ray Source

Obviously, these electron bunches can be used to generate secondary X-rays. In the following this possibility will be theoretically assessed for the well known channelling effect as well as Thomson scattering.

10.2.1 Channelling Radiation

Channelling radiation in the keV order can be generated when low emittance MeV electrons are "guided" through a crystal along its axis and planes [115]. Due to the discrete spatial translation symmetry in a crystal lattice, this effect can be described as numerous peripheral and correlated scattering of electrons. As indicated in Fig. 10.6, electrons can undergo transitions between discretely bound energy levels within such a crystal potential. These transitions result in the emission of X-ray photons with well defined energies in the keV order, which is reached due to a large relativistic Doppler shift. However, for a given electron energy, these X-ray lines can only be tuned at some keV by changing the crystal potential, i.e., the crystal orientation.

Figure 10.6: Principle of channelling. Electrons are injected under a critical angle, φ_{cr}, into a crystal lattice. Bound by the crystal potential, electrons oscillate, classically spoken, along its axis and planes. Quantum mechanically, these electrons occupy discrete levels in this crystal potential, whereas their transition between those levels can result in the emission of X-rays.

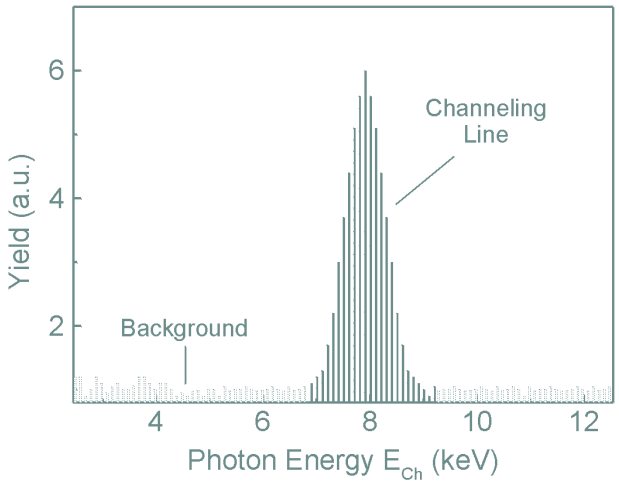

Figure 10.7: Possible channelling radiation spectrum from a 1-0 transition, when (9 ± 0.1) MeV electrons are injected along the (110) plane of a 13 μm thick diamond crystal. The bremsstrahlung background has been subtracted [117].

Channelling radiation experiments are usually carried out at low emittance electron accelerators, which operate at one fixed electron beam energy only. Hence, this limits the experimentally accessible X-ray lines – unlike the FLWF electron source, which would show more flexibility, since it fulfills the required beam quality over a wide range of energies. Consequently, a wider X-ray energy range could become accessible using this electron source instead.

10.2.1.1 Channelling Radiation Spectra

The discrete spatial invariance of the lattice potential in a single crystal acts as a periodic distortion for electrons, which can be described with Fermi's Golden Rule. The intensity of channelling radiation, I_{Ch}, can then be expressed as

$$I_{Ch} = \frac{1}{2}\frac{\alpha}{4\pi}\frac{E_{Ch}^3\, d}{(\hbar c)^3\, \gamma^2}|r_{i\to f}|^2\, d\Omega, \tag{10.1}$$

where $|r_{i\to f}|$ is the transition matrix element of electrons within a crystal potential, U. The separation of the single crystal axes or planes is d, and α is the fine structure constant. Since the energy of channelling photons, E_{Ch}, on the electron beam axis is approximately $2\hbar\sqrt{2U/m_e}\,\gamma^{\frac{3}{2}}$ the intensity, I_{Ch}, shows a strong dependence, $\gamma^{5/2}$, on the relativistic Lorentz factor, γ [116]. These photons are emitted in an opening cone proportional to γ^{-1}, indicating that harder X-rays are better collimated.

Adapting these scaling laws and known experimental results for various crystals and symmetries to the parameters of the FLWF electron beam, the channelling spec-

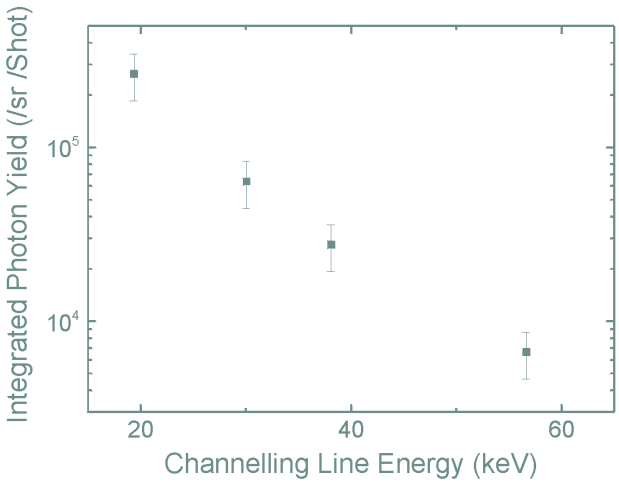

Figure 10.8: Integrated channelling photon yield for the same symmetry as in Fig. 10.7 but for varying electron energies.

trum shown in Fig. 10.7 could be obtained, when (9 ± 0.1) MeV electrons are injected along the (110) plane of a 13 μm thick diamond crystal. Here, the bremsstrahlung background was subtracted, which can be estimated when the crystal is randomly orientated towards the electron beam axis.

10.2.1.2 Channelling Photon Yield

Maintaining the assumed symmetry, but varying the electron energy could yield the in Fig. 10.8 given integrated peak channelling photon intensities with different line energies, E_{Ch}. Even though the FLWF electron source is available at 10 Hz, higher photon yields of up to 10^{10} photons s^{-1} can so far be obtained with accelerators operating at 10 MeV [115]. However, this is solely due to the higher repetition rates of such installations, which can even operate with cw beams.

Using the FLWF electron source instead, this will deliver shorter photon flashes of the order of 100 fs, as they are induced by ultra short electron bunches. Additionally, a greatly increased photon energy range will be covered. This might be important and particularly interesting as an approach for medicine, when this channelling X-ray source would be used for imaging coronary vessels by differential spectroscopy.

It is noted that this lower photon yield is due to the selection of an electron energy bin. Since the bunch charge of all electrons was experimentally determined to be 5 nC, the photon flux could be enhanced using the entire electron spectrum as it will be shown in the following.

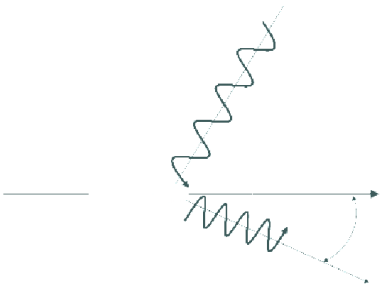

Figure 10.9: Schematic of Thomson X scattering. Details are given in the text.

10.2.2 Thomson Scattering

A polychromatic X-ray source in the keV range can be produced by Thomson scattering a second laser beam of lower intensity on the entire electron bunch [118]. A schematic representation of the experimental set-up is given in Fig. 10.9.

The interaction between the electrons and the laser electromagnetic field can be described by an undulator model in which the radiation pattern is that of a relativistic oscillating dipole. As for the channelling effect, the keV photon energy range is reached in the linear regime of Thomson scattering due to a large relativistic Doppler shift of the radiation emitted by the oscillating electrons. The energy, E_{Th}, of the produced X-rays depends on the angle between the laser and electron beam, θ, as well as on the angle of observation relative to the electron beam direction, φ. It is given in [119] by

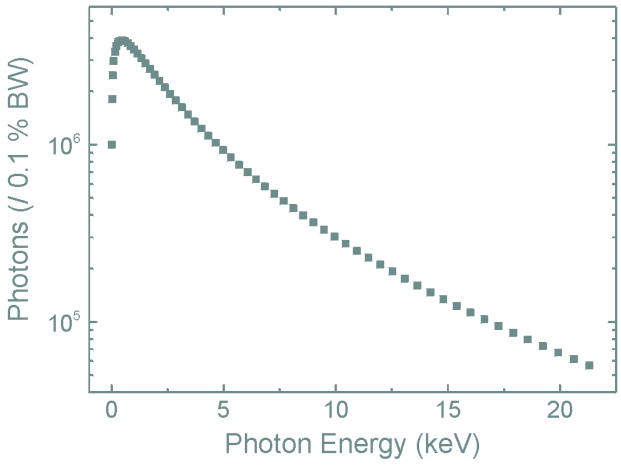

Figure 10.10: Thomson X photon intensity for θ of 90°, integrated over all φ. The laser wavelength was assumed to be 820 nm.

$$E_{Th} = \frac{2\hbar\gamma^2\omega_0}{1+\gamma^2\varphi^2}(1+\beta\cos\theta). \tag{10.2}$$

The calculated spectrum of the expected X-ray pulse using the entire FLWF electron spectrum up to 200 MeV is displayed in Fig. 10.10. Clearly, the number of few keV X-ray photons reaches 10^7 in a 0.1 % spectral bandwidth.

In addition to its "table top" size, this "laser synchrotron" offers two principal advantages. First, it produces highly collimated hard X-rays with an opening cone proportional to γ^{-1}, and a tight focusing of a 30 fs laser beam crossing the bunch of electrons at 90° should provide 30 fs X-ray flashes. Second, as the period of the electromagnetic field is much shorter (μm scale) than in an usual undulator of static magnets (cm scale), the required electron energy to produce hard X-rays is about a few hundred times less than in a synchrotron.

Part IV

Proton Beam Generation with Foil Targets

Chapter 11

Motivation and Experimental Layout

In the following a brief review will be given on recent experimental results on proton beam generation with high intensity lasers, which were focused onto solid targets. This introduction will subsequently lead to the motivation of the presented experiments. Their set-ups will be summarized, since the single components were already discussed in this manuscript.

11.1 Previous Work and Motivation

The emission of high energy ions from solid targets has been measured in numerous experiments since the 1960's over a vast range of intensities, laser pulse durations and target materials [120]. One of the most consistent results from all these measurements was that the bulk of the fast ion signal observed consisted always of protons, regardless of the actual target material. This was found to be due to thin impurity layers in the nm range of hydrocarbons originating from grease or oil, which contaminate the target surface, since, in practice, it is impossible to obtain pure targets. Given that hydrogen is present, protons will respond more rapidly to the electrical fields induced by the laser plasma interaction than any heavier ion.
As mentioned in Chapter 2.3.2.3 the origin of these laser accelerated protons can be the front as well as the rear of the target illuminated. In [8], protons were observed to be emitted in ring patterns, the radii of which depend on the proton energy, which was explained by self-generated magnetic fields inside the target due to the propagation of hot electrons. Hence, these protons were originating from the front of the target. For this interpretation additional evidence comes from an experiment in which deuterium was coated on a thin film of mylar and a boron target was placed behind it [121]. It was found that only when the deuterium was on the front side the boron became activated by $^{10}\mathrm{B}(d,n)^{11}\mathrm{C}$ reactions. In contrast, evidence was given in [53] that laser produced protons originate from the back side, which comes from the results obtained using wedge-shaped targets. The proton beam was observed to point in the direction normal to the back side of the target, which was not perpendicular to the front surface. Theoretically it is clear that such protons can originate from either side of the target. Thus, experimental observations must not only be compared for the laser energy and pulse length, but also for the angle of incidence of the laser beam, its polarization,

pulse duration, contrast ratio as well as the target dimensions. All these parameters should make a severe difference in any experiment, which might explain the differences of the reported results.
Despite this alleged disagreement, the majority of these experiments concentrated on measuring the maximum proton energy. Here, the highest energy yet reported is 58 MeV for a peak laser intensity of 3×10^{20} W/cm^2 using a 500 J, 500 fs FWHM laser pulse, which was focused onto a 100 μm thick plastic foil [53]. Using smaller lasers delivering 50 J pulses of 1 ps FWHM duration, which were focused down to intensities of 5×10^{19} W/cm^2 onto 125 μm thick aluminum targets resulted in the generation of 10^{12} protons beyond 2 MeV and a maximum energy of up to 18 MeV [8].
In both these "proof of principle" experiments large scale Nd:Glass lasers were used, which have a repetition rate of 1 shot every 20 minutes. However, due to these low repetition rates it is unlikely that such laser systems will provide sufficient information to elucidate the processes of proton acceleration. Additionally, due to their inherently large costs it is questionable if they will ever be suitable for applications. Thus, the extension of these studies to smaller, but higher repetition rate lasers, maintaining similar focused intensities is required.
Recent results in [122] using a 3 J, 100 fs FWHM laser pulse focused down to an intensity greater than 10^{20} W/cm^2 onto an aluminum target showed that proton energies as high as 24 MeV can be obtained from 3 μm targets. Here, the enhanced proton energy was assigned to be due to the high contrast ratio of 10^{-10} provided by the laser implemented. Any deterioration resulted in a decreased maximum proton energy under the same experimental conditions.
In contrast, proton generation on existing, "table top," Ti:Sa lasers, which operate at a repetition rate of 10 Hz, has received less attention. Here, only proton beams of up to 1.5 MeV have been recently reported in [123], where a 200 mJ, 60 fs laser was focused down to intensities of 7×10^{18} W/cm^2 onto 23 μm thick plastic foils. This observation was explained to be due to the low laser contrast ratio of the order of some 10^{-5}.

Obviously, there are so far neither the quantity nor the range of data needed to decipher the processes and the feasibility of proton generation and acceleration using "table top" lasers. Hence, it is the aim of the experiments presented here to perform a first experiment on

1. energetic proton beam generation with solid targets using a
2. high repetition rate, high contrast, high energy, Ti:Sa laser system.

11.2 Experimental Layout

The experiments presented here were performed at two different campaigns on the in Chapter 7.2.1 presented "salle jaune" laser operating at 820 nm and 10 Hz in the CPA mode. At the first campaign, the laser was focused at normal incidence onto the target,

whereas for the second run the target was positioned at 45° relative to the laser beam axis. Obviously, these different geometries change the interaction parameters such as the laser focal waist, intensity and preplasma conditions. As furthermore also different targets were used, these experiments will in the following be regarded separately.

11.2.1 Laser Parameters and Targets

11.2.1.1 Irradiation at Normal Incidence

Here, the laser with an on target energy, E_L, of up to 840 mJ and p-polarized pulses with a FWHM duration, τ_0, of 40 fs was focused using a $f/3$ off-axis parabolic mirror. Since the focal waist, w_0, was 4 μm, this resulted in peak intensities, I_L, of up to 6×10^{19} W/cm^2. For these impulsions the laser contrast ratio was found to be of the order of 10^{-6}.

The target foils were mounted on a 70 μm thick nickel grid, whereas the diameter and spacing of the holes into the grid were 1 and 2 mm respectively. The foils were placed in the laser focal spot, which was verified by the back reflection of the laser onto a 8-bit CCD camera. For this experiment two different kinds of targets were used : *(i)* 6 μm thick plastic, and, *(ii)* 6 μm thick aluminium foils.

11.2.1.2 Irradiation at 45°

For the second campaign, this laser delivered higher on target energies, E_L, of up to 1.2 J in 30 fs FWHM linearly polarized pulses. Implementing the same $f/3$ off-axis parabolic mirror, the focal waist, w_0, was due to the different geometry 5.6 μm. Consequently, the peak laser intensity, I_L, was 5.8×10^{19} W/cm^2. Again, the laser contrast ratio was found to be of the order of 10^{-6}.

For this experiment the targets were mounted and aligned the same way as for the irradiation at normal incidence. Here, however, two different targets were used :*(i)* 6 μm, and, *(b)* 13 μm thick plastic foils.

NB, that for both these experiments the preplasma parameters were not monitored due to technological difficulties. For both these arrangements, the proton detectors implemented were the same and will be described in the following.

11.2.2 Proton Detector

CR-39 nuclear track detectors, which were introduced in Chapter 4.2.2.2 were used to obtain the yield as well as the opening cone of the proton beam. As it is indicated in Fig. 11.1 they were installed at a distance of typically 3 cm behind the target foils on the laser beam axis, and, eventually, on the target normal.

Figure 11.1: Sketch of the experimental set-up. The laser was focused with an off-axis parabolic mirror *(a)* onto the surface of thin foils *(b)*. In case these were, as indicated, positioned under 45° towards the laser beam axis the expelled proton beam was characterized with CR-39 detectors and aluminum filters *(c)* on the laser beam axis as well as on the target normal. In case the foils were under 90° these detectors were only positioned on the laser axis.

11.2.2.1 Proton Energy Determination

Since CR-39 for itself does not reveal any information on the energy of the protons penetrating it, they were covered with single layers of aluminium foils, which served as energy filters. As it was described in Chapter 7.3.1.2, protons require a kinetic energy, W_p, beyond the energy they deposit propagating through these filters, W_{depo}, in order to reach the CR-39 placed behind it. Thus, varying their thickness, an energy spectrum can be reconstructed for protons with a kinetic energy beyond $W_{depo} + 100$ keV.

Despite its simplicity, this method clearly suffers from its rough energy resolution, which is determined by the stopping power, i.e., the thickness of the aluminium filters used. Since their step size was about 50 μm the attainable energy resolution, $\triangle W_p$, was typically ± 1 MeV or worse. Hence, in case of a clear cut-off energy of the proton beam its determination is seriously compounded, as it is indicated in Fig. 11.2.

Finally it is noted, that this energy determination also ensured that the analyzed traces on the CR-39 detectors were due to protons rather than different ions. Focusing, e.g., the laser onto plastic targets, there would be the possibility that carbon ions are accelerated to extremely high energies during the laser plasma interaction. This possibility is quite unlikely, since, first, carbon ions with an energy well beyond 200 MeV would be required to pass the 625 μm aluminum filters implemented to stop 10 MeV protons. Second, the traces behind these filters did not show any great difference, which would be expected if two different ion species would have been accelerated.

11.2.2.2 Determination of Opening Cone

Since these energy filters had additionally various widths, the opening cone of the proton beam could be determined simultaneously, as it is illustrated in Fig. 11.3. Here,

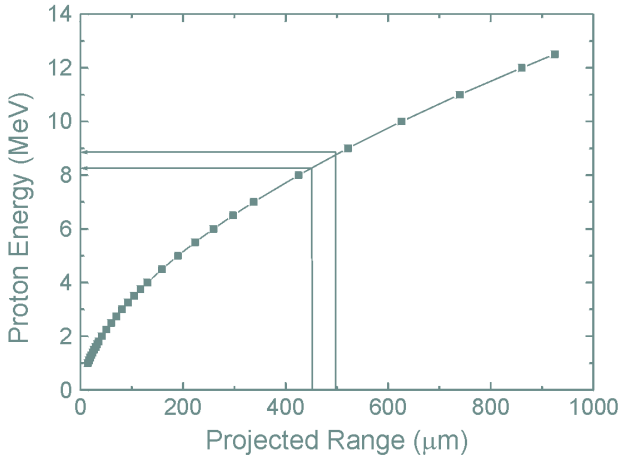

Figure 11.2: Energy resolution of aluminium filters used, exemplary indicated for two superposing layers of 450 and 500 μm.

the aluminum filters were adapted to only partially cover the proton beam envelope, which allowed to reconstruct the angular divergence of the proton beam within the given energy resolution of the implemented aluminum filters.

Indeed, the measured opening cone has to be corrected for the well known Coulomb scattering of the proton beam within these layers, as it was described in Chapter 7.3.3. Finally it is noted, that it was ensured with additional laser shots, where just one aluminum filter with a thickness of interest covered the entire CR-39, that the proton beam had indeed a homogeneous spatial distribution.

Figure 11.3: Principle of aluminium filters on top of CR-39. Superposing aluminium filters with various widths and thicknesses stopped protons according to their energies. Consequently, this arrangement gave additionally the divergence of the proton beam.

Chapter 12

Experimental and Numerical Results

In this chapter experimental as well as numerical results will be given for the target irradiation at normal incidence. It will be shown, that protons are accelerated up to an energy of 10 MeV and that this acceleration origins from the front as well as the back surface of the target. The presentation of the irradiation under 45°, which yielded two distinct proton beams, one along the laser direction and the other directed off the target normal, is restricted to the experimental results only.

12.1 Irradiation at Normal Incidence

12.1.1 Experimental Results and Discussion

Figure 12.1 shows the optimum proton energy spectrum measured at an irradiance of 6×10^{19} W/cm^2 for 6 μm thick plastic targets. Obviously, the proton energy reaches

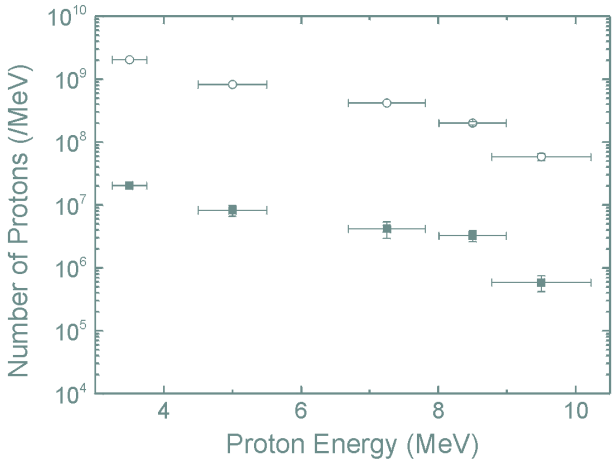

Figure 12.1: Proton spectra at an irradiance of 6×10^{19} W/cm^2 for 6 μm plastic (black dots) and aluminium targets (light circles). For the latter, the arrows indicate the minimum number of protons, which results in the saturation of the detectors.

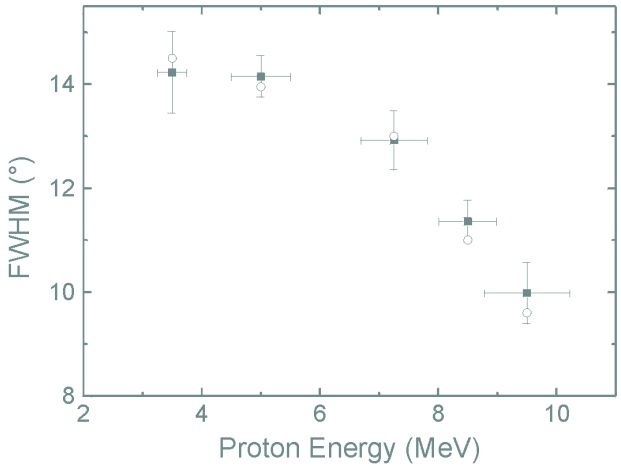

Figure 12.2: FWHM of the proton beams shown in Fig. 12.1 obtained with the 6 μm plastic (black dots) and aluminum (light circles) targets.

10 MeV, where a clear cut-off energy is suggested. As can be seen in Fig. 12.2, this proton beam is better collimated the higher the proton energy. It is noted that this maximum proton energy was only obtained at the best contrast ratio of the laser, i.e., any deterioration resulted in a lower maximum proton energy. This might be explained by the approximately 3 ns wide laser prepulse with an intensity of up to 10^{13} W/cm^2. It is well known that at such an intensity a laser can ablate about 1 μm of plastic foils per ns [124], generating shock waves, which can break out before the short laser pulse interacts with the target. Additionally, the different preplasma conditions might have resulted in a less efficient absorption of the laser energy, and, consequently, to the generation of an electron beam with a lower temperature.

Interestingly, the high energy proton yield was enhanced at the same irradiance by at least a factor of 100 by using 6 μm thick aluminum targets, as it is also shown in Fig. 12.1. However, an accurate determination of the distribution below 8 MeV could not be obtained due to this extremely high flux, which saturated the detectors. Nevertheless the minimum value to obtain such a saturation can be given by the limiting resolution of pits in the CR-39. Note, that the angular divergence of the proton beam with this metallic target did not change, as can be seen in Fig. 12.2. This difference in the number of accelerated protons might be due to the different electrical response of these materials, which is either an isolator or a conductor [125]. As isolators are characterized by a smaller electrical conductivity, their Ohmic dissipation is stronger and laser heated electrons propagating through the target are losing their energy faster. Hence, the number of electrons, which reach the target back surface and induce an accelerating field could be smaller. Another explanation might be the experimentally not monitored different initial preplasma conditions. Since aluminium has a higher reflectivity than the transparent plastic, the target ablation as well as the formation of the preplasma might be different.

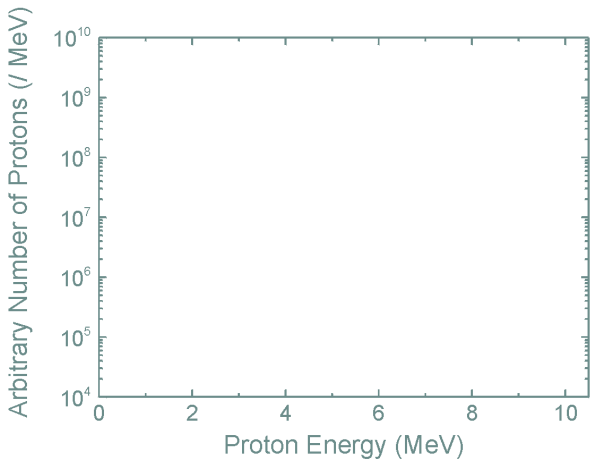

Figure 12.3: Calculated proton energy at an irradiance of 3×10^{19} W/cm^2 for a carbon and hydrogen plasma. Note that the proton number from the PIC simulation is in arbitrary units.

12.1.2 Numerical Modelling

12.1.2.1 Energy Spectrum

These measurements are in qualitative agreement with a kinetic simulation that was performed with the PIC code CALDER. In this calculation, a 35 fs laser pulse was focused at normal incidence onto a plastic target down to a 6.8 μm FWHM spot, with a peak irradiance of 3×10^{19} W/cm^2. The target was modelled as a $6n_c$, fully ionized, 5 μm thick carbon and hydrogen plasma. It is preceded by an exponential density gradient with a 4 μm characteristic length, to account for the slight expansion that results from laser prepulse.

This small, lower density plasma is important as it favors an efficient energy transfer from the laser pulse to the target electrons. At the end of the pulse, almost 75 % of the incident energy has been coupled to hot electrons that spread and form an electron cloud around the target. The electrons that leave the plasma and extend into vacuum set up a quasi-static electric field at the back of the target that reaches a maximum value of a few TV/m. As a result, proton and carbon ions are accelerated into vacuum from the rear side of the target, and the space-charge field decays as this expansion proceeds. Due to their lower mass, protons are accelerated with the highest efficiency.

In less than 1 ps, the distributions of protons extends up to 10 MeV, as shown in Fig. 12.3. The regular variations, followed by an abrupt cut-off at the maximum energy, is similar to the experiment. The dip in the proton spectrum, observed around 1 MeV, can be linked to the acceleration of carbon ions : as these ions are less mobile than protons, they are accelerated to a lower velocity – hence reducing the number of protons in the blow-off below that energy, compared to a pure proton expansion. Finally, it is

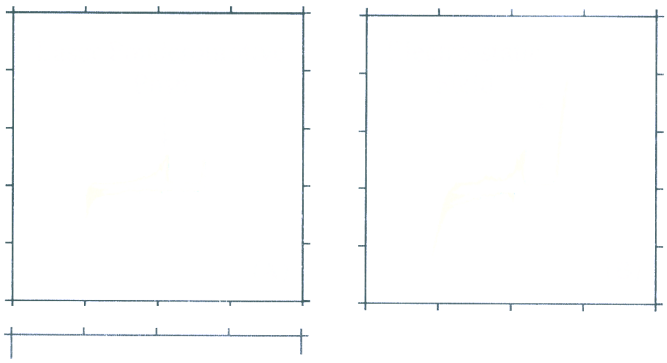

Figure 12.4: Calculated proton phase space for three consecutive time steps along the laser beam axis. Closer descriptions are given in the text.

noted that the smooth transverse variations of the accelerating field, computed with a FWHM of 16 μm, explains why the proton beam is generated with a good collimation : the calculated angular FWHM at (5 ± 1) MeV is 12°, which is in qualitative agreement with the experimental measurement.

12.1.2.2 Phase Space

To better understand the occurring mechanisms it is instructive to regard the calculated evolution of the proton phase space, which is shown in Fig. 12.4. At the beginning of the simulation, (A), both, the laser ponderomotive push and the induced electrostatic field on the back side of the target accelerate protons equally. Since not all electrons propagating through the target have reached the back surface, the maximum energy protons gain is limited to 1 MeV.

Obviously the laser ponderomotive push can solely contribute to the acceleration of protons during the presence of the laser pulse and vanishes once the laser is reflected at the critical surface. Since under the experimental conditions the laser pulse length, τ_0, is only 40 fs, there appears not to be enough time to establish the maximum equilibrium between the generated electrostatic field and the laser ponderomotive push given in Eq. 2.62. This might be why 200 fs later, (B), protons do not experience any

acceleration beyond 1 MeV anymore from this acceleration mechanism, even though Eq. 2.65 suggests a maximum proton energy of about 8 MeV.

Meanwhile, as more electrons reached the back surface of the target, the quasi-static electric field passes its maximum in less than 1 ps. And it is here, were protons experience their highest acceleration of up to 10 MeV, (C). Finally it is noted, that the created plasma does also expand on the target front side, which also induces an electro-static field, and which accelerates protons to an energy of about 6.5 MeV.

12.2 Irradiation under 45°

Interestingly, turning the target under 45° towards the laser beam axis yielded two distinct proton beams in the forward direction – one along the laser direction and the other off the target normal.

12.2.1 6 μm Plastic Foil

12.2.1.1 Energy and Angular Divergence

Figure 12.5 shows the spectra of the two distinct proton beams on the laser beam axis as well as on the target normal for a laser irradiance of 2.7×10^{19} W/cm^2. Both reveal no great difference within the resolution of the implemented detector. The same accounts for their angular divergence, which appears to be identical, as it is indicated in Fig. 12.6.

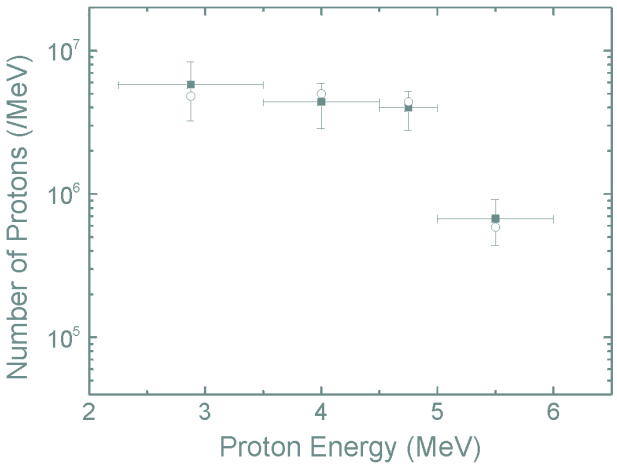

Figure 12.5: Proton spectra on the laser axis (squares) and on the target normal (light circles) for 6 μm thick plastic targets and an irradiance of 2.7×10^{19} W/cm^2.

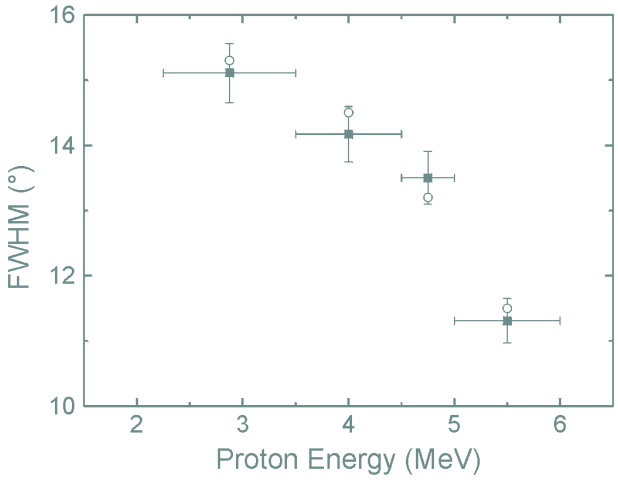

Figure 12.6: FWHM for the proton beams shown in Fig. 12.5 on the laser axis (squares) and on the target normal (light circles) using 6 μm thick plastic targets.

Indeed, as can be seen in Fig. 12.7, those two beams are completely distinct, i.e., fully separated. The space in between the two beam envelopes did not show any trace of energetic protons with an energy beyond 2 MeV. It is noted, that this interaction yielded a homogenous proton emission with such an energy in the forward solid angle.

Dependence on Laser Contrast Ratio

Interestingly, the indicated cut-off energy of around 5.5 MeV for these two beams was not obtained at every laser shot, but showed a strong dependence on the laser

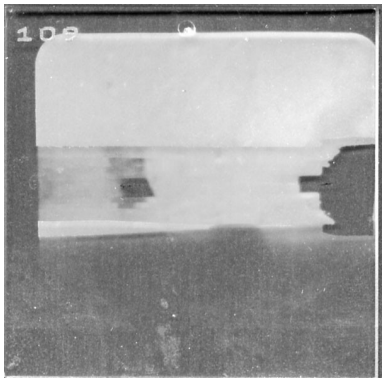

Figure 12.7: Traces of two distinct proton beams on the implemented CR-39 detectors. The upper part of the figure shows traces of low energy protons with an energy below 2 MeV. The lower part of the CR-39 was blocked by the target mount. Clearly, the two proton beams were distinct, since the "gap" in between their beam envelopes did not show any trace of energetic protons.

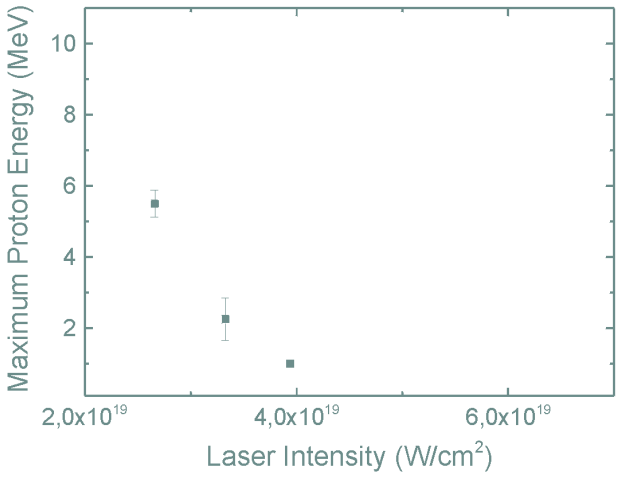

Figure 12.8: Dependence of maximum proton energy on laser intensity for 6 μm plastic target.

contrast ratio. Clearly, increasing the prepulse intensity to approximately 2×10^{13} W/cm^2 decreased the maximum proton energy to (3.5 ± 0.75) MeV – even though, the low energy proton flux was identical.

Interestingly, the direction of the proton beam on the target normal did not change its direction with varying preplasma scale lengths. This observation is different to [128], where the emission of hot electrons for increasing plasma scale lengths moved from the target normal towards the laser beam axis, which was explained by Brunel-type resonance absorption being the dominant laser absorption mechanism and possible filamentation and self-focusing of the laser beam in the generated underdense plasma. However, in the case presented here, only the maximum proton beam energy changed. Not the direction.

Dependence on Laser Intensity

Figure 12.8 shows the dependence of the maximum proton energy on laser intensity. Clearly, for an irradiance beyond 4×10^{19} W/cm^2 none of the two proton beams was experimentally observed, which indicates, that the plastic target might got altered by the preplasma, when the irradiance was increased.

12.2.2 13 μm Plastic Foil

12.2.2.1 Energy and Angular Divergence

Replacing the target with 13 μm thick plastic foils lead to a higher maximum proton energy of up to (10.3 ± 0.6) MeV and an enhanced proton yield by more than

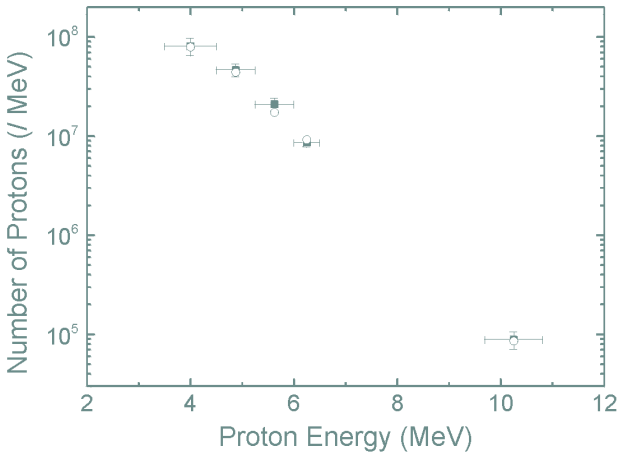

Figure 12.9: Proton spectra on the laser axis (squares) and on the target normal (light circles) using a 13 μm thick plastic target at an irradiance of 6×10^{19} W/cm^2.

one order of magnitude, as can be seen in Fig. 12.9. Here, again, it is observed that the opening cone of this beam decreases as the proton energy increases, like it is indicated in Fig. 12.10.

Dependence on Laser Intensity

Changing the laser intensity, but remaining the same contrast ratio of the laser changed the maximum proton energy corresponding to Fig. 12.11. Since the target

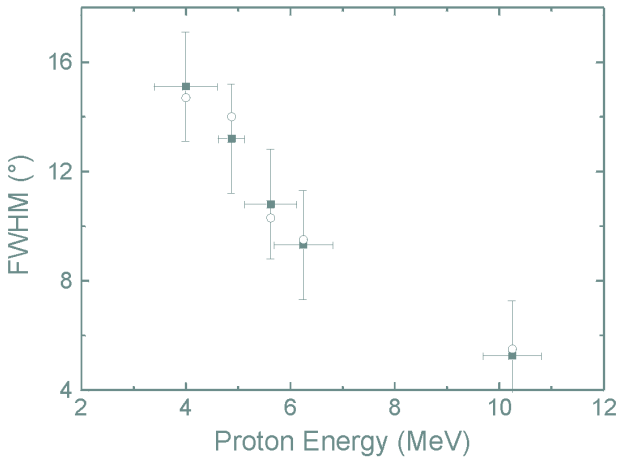

Figure 12.10: FWHM for the proton beams shown in Fig. 12.9 on the laser axis (squares) and on the target normal (light circles) using 13 μm thick plastic targets.

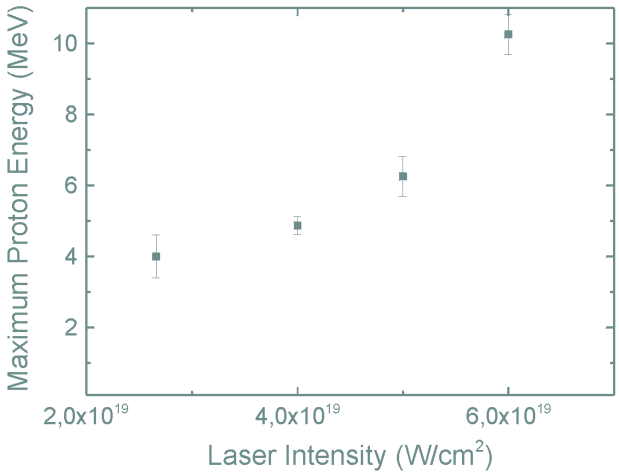

Figure 12.11: Dependence of maximum proton energy on laser intensity for 13 μm plastic target.

thickness has been chosen to avoid the break out of shock waves, the increased proton energy is in agreement with theoretical predictions presented in Chapter 2.3.2. Assuming that the preplasma is identical for varying laser intensities the electron temperature will increase accordingly, and, hence, increase the maximum proton energy.

It is noted that this presentation of the data is purely restricted to experimental observations, since the modelling of this interaction at 45° is compounded by the occurring planar plasma density gradient. Since this gradient was not monitored experimentally, and since this preplasma on the target surface already appeared for the irradiation at normal incidence to be the most critical parameter, the numerical modelling of these results is currently the scope of the work in [127].

In conclusion, it was shown that the interaction of a laser at 6×10^{19} W/cm^2, which is focused under normal incidence onto 6 μm thick plastic targets can result in a proton beam with an energy of up to 10 MeV. Using an aluminium target with the same thickness can increase the proton flux by at least a factor of 100, which is probably due to the different electrical response of this material.
Turning the target at 45° towards the laser beam axis can yield two distinct proton beams, one along the laser direction and the other directed off the target normal. Here, changing the target thickness from 6 to 13 μm enhances the maximum proton energy from 5.5 up to 10 MeV by increasing the laser irradiance from 2.6 to 6×10^{19} W/cm^2.

Interestingly, these energetic proton beams are generated with 50 times less laser energy than in [8] and at a 10 Hz laser facility. This might favor their implementation for various application, whereas two possibilities will be assessed in the following chapter.

Chapter 13

Applications

In the previous chapter the generation of a proton beam with an energy of up to 10 MeV was demonstrated. Since this energy is much in excess of recently reported results at similar high repetition rate laser systems, this enhancement might permit to pursue some applications for positron emission tomography as well as probing of structures. Their feasibility will be elucidated in the following.

13.1 Positron Emission Tomography

The production of short-lived isotopes such as ^{11}C or ^{18}F is important in medicine for Positron Emission Tomography (PET), since they undergo β^+ decays with half-lifes of 20.4 and 109.7 min respectively. When these positrons pass through matter, they slow down and annihilate at rest with free electrons, which produces two counter-propagating photons of 511 keV. Using an arrangement of coincidence detectors at 180° around a sample with such a radioactive probe inside, the activity and location of the radio-isotopes can be determined.

13.1.1 Principle and Requirements

This principle is used in medical imaging, where these radio-pharmaceuticals are injected into a patient. The radioisotope carriers are taken up wherever they are used in the body, enabling the imaging of blood flow or tumors, where the blood circulation is significantly reduced, and, hence, the emission of positrons increased. This principle is indicated in Fig. 13.1.

Nowadays, these radio-pharmaceuticals are generated using proton beams produced by cyclotrons or Van de Graaff accelerators, which induce (p, n) reactions with ^{11}B and ^{18}O nuclei inside a target. Due to the size, cost and shielding required for such installations, PET is limited to a few facilities only [129].

Even though the energy spectrum of the in Chapter 12.1 presented proton beam has a broad Maxwellian-like distribution, it can nevertheless be used for the generation of radio-isotopes as long as their energy is greater than the Q-value, i.e. the threshold

Figure 13.1: Principle of positron emission tomography. Using an arrangement of coincidence detectors around a patient the concentrated location of PET isotopes in, e.g., brain tumors can be determined.

of the (p, n) reaction, and the number of protons is sufficient to obtain an appropriate activation. Since the corresponding Q-values for (p, n) reactions for ^{11}B and ^{18}O are 2.8 and 2.4 MeV respectively, this laser produced proton beam might therefore represent an alternative method for PET isotope production.

13.1.2 Benefits using High Repetition Rate Laser Systems

So far, this possibility was mostly investigated on large Nd:Glass lasers [130], which have a repetition rate of roughly 1 shot every 20 minutes. Even though PET isotopes were produced with activities larger than 10^5 Bq [129], their practical usage is limited due to this low repetition rate. Obviously, using existing, "table top", Ti:Sa lasers, which typically operate at a repetition rate of 10 Hz, would not suffer from this drawback.

This principle would be particularly interesting, since, compared to conventional accelerators, it has a number of advantages : *(i)* as it was shown above, the accelerating fields can reach the TV/m range, which cuts down the required acceleration length to some tens of microns; *(ii)* such laser systems are comparatively compact and cheap; *(iii)* no shielding for radioprotection is needed up to the point where protons are generated, i.e., where the laser interacts with the plasma. All this makes this approach potentially valuable.

13.1.3 Expected Activities

Indeed, the generated proton beam using the 6 μm thick plastic target at normal incidence can be used to generate ^{11}C and ^{18}F isotopes. Their expected activities were calculated with the CALDER MC code, using experimental values for the cross sections

Table 13.1: Calculated PET activities for the minimum proton beam obtained with the 6 μm aluminum target. The secondary activation targets are chosen to have an areal thickness of 0.24 g/cm^2. The laser irradiation time would be 30 min.

Activation Target	Q-value (MeV)	LOA laser at 10 Hz MBq (mCi)	LOA laser at 1 kHz MBq (mCi)
^{11}B	2.76	13.4 (0.36)	1340 (36.2)
^{18}O	2.44	2.9 (0.08)	290 (7.9)

[97] and the Bethe formula for the stopping power. The ^{11}B and ^{18}O targets modelled in the code were considered thick enough to slow down all incident protons below the respective reaction Q-values. This corresponds to an areal density of approximately 0.24 g/cm^2 for both targets.

With this proton spectrum the calculated activities in ^{11}C and ^{18}F samples would be 12 and 2 Bq per shot. Accumulating laser shots at 10 Hz for 30 minutes with the same activation target, while taking into account the simultaneous isotope decay discussed in Chapter 7.3.4.1, would result in activities of 134 and 29 kBq respectively. Since for a given activation rate the decay matches production after a certain time, these integrated activities would saturate at 209 kBq for ^{11}C and 170 kBq for ^{18}F. However, a typical patient dose for PET is 200 MBq and it is necessary to go up to 800 MBq so that fast chemistry can be performed to separate the tracer from the inactive carrier [130]. It is thus impossible to get a medical dose with the current LOA set-up.

To obtain nevertheless the requested activities for PET, either the flux of accelerated protons or the repetition rate of the laser needs to be increased. Performing the same calculation with the experimentally observed proton yield for aluminum targets instead of plastic, and increasing the repetition rate of the laser to 1 kHz, extends the 30-minute activities to the GBq order. As can be seen in Table 13.1.3, this approach to use laser plasma interactions hence appears comparable to the one using contemporary accelerators.

Additionally, there is evidence that the efficiency of this scheme can be improved by operating at higher peak laser intensity. Calculations with CALDER and CALDER MC indicate that a modest increase in intensity to 8×10^{19} W/cm^2, results in more protons at higher energies, which leads to a 7-fold increase in ^{18}F activity. This favorable intensity scaling is supported by recent experimental observations at 5×10^{20} W/cm^2, which yielded 3 MBq of ^{11}C [131], more than one order of magnitude greater than what was obtained at 5×10^{19} W/cm^2 with the same experimental set-up [129].

In conclusions, the experimental observations and numerical calculations support the prospect of producing GBq sources of PET isotopes in the near future with "table top" laser systems. It is thus conservatively estimated that this goal could be met by a system delivering 1 J pulses focused to 10^{20} W/cm^2, and operating at 1 kHz.

13.2 Proton Beams as Radiographic Source

Another possibility would be to use such proton beams as a radiographic source. This idea has circulated for many years [132], whereas applications have been proposed in the biomedical area [133] or in testing of thick systems [134]. Here, a particularly interesting application of laser produced proton beams is the detection of electric and magnetic fields generated during the interaction of intense laser pulses with plasmas [135], like it is indicated in Fig. 13.2. Since the incident proton parameters are known and their absorption or deflection after an interaction can be experimentally determined, this permits to draw conclusions on the evoked electric and magnetic fields during the interaction.

13.2.1 Interest in Probing Laser Plasma Interactions

In this context, one can benefit from the unique properties of laser produced proton beams : *(i)* They origin from a small source size. This can be estimated to be of the order of the laser focal waist, which, hence, increases the attainable resolution; *(ii)* These beams have a high degree of collimation, thus, they deliver a high spatial proton flux; *(iii)* They have a short pulse duration, which is likely to be in the ps order, which obviously enhances the attainable time resolution; *(iv)* They are synchronized with a laser beam, which permits to carry out pump-probe experiments; *(v)* Due to their broad spectrum, protons with different energies have different TOF's to reach the interaction region. Hence, implementing an adequate proton detector a time resolved study of the laser plasma interaction can be obtained with a single proton burst. These benefits can indeed help to get insight into a laser plasma interaction as it will be shown in the following by the brief presentation of a recent experiment.

13.2.2 Experiment and Results

This experiment was performed on the aforementioned "salle jaune" laser and is the scope of the work in [136]. Here, the probe laser beam with an intensity of up to 3×10^{19} W/cm^2 was focused onto the edge of 6 μm thick plastic foils, which resulted in the generation of a proton beam with a maximum energy of 3 MeV. This beam was characterized in exactly the same way as described in Chapter 11.2.2.

Figure 13.2: Experimental set-up for proton imaging. The probe laser beam was focused with an off-axis parabolic mirror *(a)* onto a 6 μm thick plastic foil *(b)*, which resulted in the generation of an energetic proton beam. The envelope of this beam covered a secondary, 10 μm thick aluminum foil *(c)*. Onto this foil, the pump laser beam was focused with an additional off-axis parabolic mirror *(d)*. By changing the delay between the two laser beams, a spatial and time resolved image of the interaction was recorded on a CR-39 detector *(e)*.

The pump laser beam, again synchronized with shadowgraphy of a gas jet with a 30 fs accuracy, had a FWHM duration of 30 fs and was focused onto a 10 μm thick aluminium foil with an irradiance of 1×10^{19} W/cm^2. The layout of this experiment is indicated in Fig. 13.2.

Figure 13.3 shows the image of this proton beam, which was taken 20 ps after the interaction of the pump laser beam with the aluminum target. This time delay was determined by the known synchronization of the two laser beams and the proton TOF from their origin to the aluminum foil. In case the pump laser beam did not heat the aluminum foil, this proton image was, as expected, undisturbed. Hence, this diagnostic is sensitive to electric and, eventually, magnetic fields evoked during the pump laser plasma interaction.

Here, a "bubble" close to the initial target surface, filamentory structures outside this "bubble" and periodical modulations on the laser beam axis can be seen. The latter is likely to be due to modulations in the ion density that persists after the wake. The other two phenomena are still under consideration in [136].

NB, since such structures like the periodical modulation outside of the "bubble" were observed, the existence of a plasma in this region is suggested. This could either be the preplasma expanding from the target or a significance of poor vacuum conditions inside the target chamber.

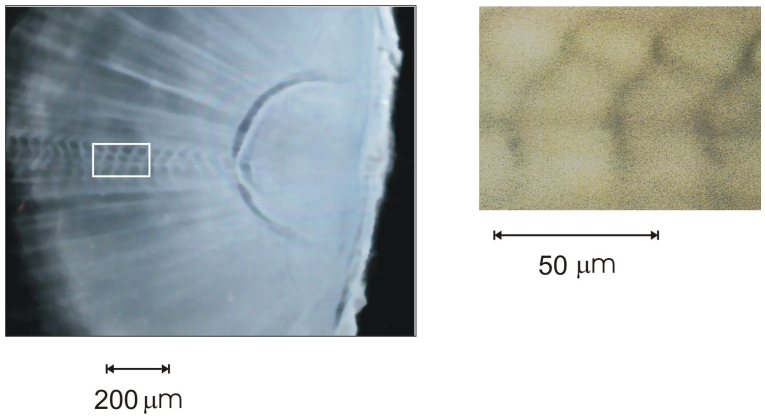

Figure 13.3: Proton image (left) taken 20 ps after the interaction of a 30 fs, 10^{19} W/cm^2 laser with the front surface of a 10 μm thick aluminium foil. The scan was done with a normal scanner, thus dark regions corresponds to a lack of protons. The enlargement (right) of the periodical modulations on the laser incidence axis was obtained with an optical microscope. Here, dark regions correspond to a higher proton density.

Spatial Resolution

The spatial resolution attainable for radiography with such proton beams is mainly influenced by the proton source size. At experiments on VULCAN this source size was estimated to be of the order of 10 μm [137]. Even though the laser irradiance for this measurement was comparable to the conditions at the "salle jaune" laser, VULCAN delivers much more energetic pulses, which are focused down to larger focal spots. Hence, it is likely that the proton source presented here is smaller. NB, it is not the size of the physical proton source which determines the resolution. Since this source is highly laminar it corresponds to a much smaller, virtual source located in front of the target.

Temporal Resolution

As it was shown in Chapter 12.1.2.2, protons generated with a 30 fs FWHM laser pulse appear to be emitted in less than 1 ps. Even though this value is so far not experimentally determined the duration of the proton burst is not the main contribution for the attainable temporal resolution.

As such a laser produced proton beam has a broad energy spectrum, the TOF for any proton from its point of origin to the probed interaction and from the probed interaction to the detector has to be taken into consideration. Assuming two independent protons at 3 and 0.5 MeV being emitted from the same point and at the same time, their TOF difference for a distance of 1 m is about 60 ns. Thus, the geometrical dimensions of the performed experiment limit the temporal resolution.

Measuring the width of the periodical modulation shown in Fig. 13.3, assuming cylindrical symmetry and taken into consideration the dimensions of the experimental set-up, the time resolution for this example can be estimated to be (3.75 ± 1.25) ps for 3 MeV protons.

Nevertheless, such a broad proton energy spectrum has the advantage that due to TOF considerations a laser plasma interaction can be probed at several time intervals with one proton burst only. Using, e.g., a stack out of several thin CR-39 detectors, each of these detectors would carry information of protons within a certain energy, i.e., time interval [**?**]. Self-explanatory, the attainable temporal resolution is then determined by the proton energy spectrum and the thickness of the used CR-39 detectors.

Chapter 14

Conclusions and Perspectives

In this dissertation numerous experimental as well as numerical results were presented and discussed on neutron, electron and proton generation with high-intensity lasers. Additionally, several applications of these unique particle sources have been proposed and partially realized. For lucidity these aspects will be summarized, discussed and concluded separately in the following.

14.1 Conclusions

14.1.1 Neutrons as a Diagnostic for Plasma Ion Temperature

The generation of $(1.0\pm0.2)\times10^6$ thermonuclear fusion neutrons from the interaction of an intense laser pulse with an underdense plasma was observed. These neutrons were generated by $D(d,n)^3He$ reactions in the plasma which is heated to thermonuclear ion fusion temperatures of about (1 ± 0.2) keV.

No special attention was given to maximizing the neutron yield for the gas jet interaction in this experiment. The present neutron yield corresponds to a neutron flux of approximately 1 neutron per mm^2 at 1 m distance. However, it is expected that using a pulse guided over a longer distance can increase the efficiency of energy transfer to deuterons [138]. Moreover it has been demonstrated that a small CD_2 target can increase the neutron yield by over an order of magnitude. Hence, it is thought that a longer interaction length coupled to a solid CD_2 target, that stops all radially ejected deuterons, can significantly enhance the neutron production.

Implication of Experiment in Scientific Context and Outlook

This experiment clearly demonstrated the potential as well as the importance to determine ion kinetics during the interaction of high-intensity lasers with underdense plasmas. Hence, it is proposed to extend these preliminary studies with improved equipment, like :

- Implementation of NE213 scintillators, which are specially designed as neutron detectors. This would improve the neutron detection efficiency for low yields, possibly occurring at the wavebreaking limit;
- Installation of more neutron detectors around the gas jet nozzle to smoothen the angular emission profile measurement;
- Utilization of faster oscilloscopes to enhance the temporal resolution of the TOF signals;
- Precise measurement of generated electrons during this interaction as a correlation between electron and neutron generation was experimentally observed;
- Extend these studies to higher laser intensities at the PW level since it is believed that this will increase the energy transfer to plasma deuterons and, hence, the number of fusion neutrons.

It is clear that the main interest will be to elucidate this non-collisional ion heating mechanism with numerical models, which was up to now not pursued for the relevant experimental parameters. Following the approach that filamentation and propagation instabilities of high current electron beams in a plasma can result in collisionless ion heating should help to understand this mechanism. So far, this was only numerically observed for intensities way beyond those currently accessible in experiments.

14.1.2 Electron Beam Generation in the FLWF Regime

It has been shown that focusing a 30 fs, 30 TW laser beam onto a gas jet generates bright, energetic, collimated and ultra-short electron bunches in a new regime termed "Forced Laser Wakefield." Here, the resonance conditions for classical wakefield generation are not met, since the laser pulse length was about the plasma wave wavelength. However, this interaction resulted in wavebreaking, a maximum electron energy beyond 200 MeV and an enhanced electron beam quality.

Since the high energy electrons are well collimated, specific energies can conceivably be select from the broad spectrum for use as an injector, since the normalized beam emittance was proven to be comparable to accelerators'. Doing so it was shown that channelling radiation might be an interesting alternative to generate secondary X-ray flashes, which can be significantly shorter in duration than those generated by electron beams from contemporary LINAC's. Due to the broad energy spectrum, this source shows additionally much more flexibility than accelerators. Also, focusing a second TW laser on the electron beam by a pump-probe technique can generate a short and bright X-ray pulse, which is of interest for the study of fast phenomena in biology and crystallography. Additional experiments demonstrated that this electron source can be used to observe ultra fast chemical events in radiolysis with a temporal resolution

better than 100 fs. Here advantage was taken that these electron bunches are perfectly synchronized with a laser beam, thus being free of jitter.

Implication of Experiment in Scientific Context and Outlook

This experiment clearly demonstrated that apart from the known SMLWF scheme electron generation can also be possible in the FLWF scheme. Since this resulted in higher maximum electron energies and improved beam parameters, it was shown that laser produced electrons are more than a diagnostic for laser plasma interactions.

However, it appeared that the high energy electron yield is currently too low to be competitive with LINAC's. However, numerical simulations have already shown for an improved mode of the FLWF regime that beam charges of about 5 nC can be obtained at (300 ± 25) MeV. In order to investigate this "broken wave" regime, higher laser energies of about 12 J in 25 fs laser pulses are required. It is noted that such a facility is currently under investigation at LOA [139].

In order to successfully explore this regime, the current experimental set-up should be improved as follows :

- A stronger magnet will be required to reasonably disperse several hundred MeV electrons;
- More electron detectors will be required to obtain a finer energy spectrum;
- The rapidly measurable visualization of the electron beam with monitors out of sand-blasted aluminum plates with a few hundred μg of terbium activated gadolinium oxysulfate (Gd_2O_2S:Tb) bound with barium silicate would deliver online information on the beam quality [140];
- The permanent installation of a single-shot autocorrelator at the experimental site would permit to experimentally obtain laser shortening phenomena like assumed in the FLWF regime.

14.1.3 Proton Beam Generation with Foil Targets

It was shown that the interaction of a 10 Hz laser focused under normal incidence onto thin plastic foils can result in a proton beam with an energy of up to 10 MeV. Using an aluminium target with the same thickness can increase the proton flux by at least a factor of 100. Turning the target at 45° towards the laser beam axis resulted in two distinct proton beams, one along the laser direction and the other directed off the target normal, both with a maximum energy of up to 10 MeV.

Implication of Experiment in Scientific Context and Outlook

It is clear that this experiment enables prosperous applications, since it was the very first experimental observation of energetic proton beams at a high repetition rate laser facility.

Evidentally, the experimental set-up for this preliminary experiment has to be improved by :

- Using better proton diagnostics like the aforementioned Thomson parabola or scintillating detectors like PILOT U in combination with aluminum filters;
- Monitoring preplasma conditions with interferometry;
- Enhance laser contrast ratio since this appeared to be the limiting factor in these experimental studies.

It is clear that the main investigation is to decipher the observed difference in proton yield for conducting and isolator materials. Furthermore, numerical approaches are needed to explain the simultaneous generation of two proton beams for the target orientation at 45°.

As the calculations for medical isotope production have shown, this proton source with an enhanced high energy proton yield is potentially valuable for medical applications. Also, proton-radiography studies have shown their great potential to elucidate ultra rapid processes. In this context it will be definitely interesting to determine the source size, possibly by the implementation of imaging meshes, as well as the proton burst duration by using streak cameras.

14.2 Perspectives

In conclusion, it was shown in this manuscript that the amplification of laser light to pulse powers greater than the electrical power generated by all the world's power plants combined has the potential to deliver accelerating gradients more than 1000 times greater than those produced by conventional accelerator technology. This can generate electron beams beyond 200 MeV and protons of up to 10 MeV – on a table top scale. These charged particle beams might still be seen as a diagnostic for relativistic laser plasma interactions, just like the secondary fusion neutron generation, however, they have undoubtedly the potential to be applied in many traditional areas of science in the near future.

The generation of fusion neutrons by $D(d,n)^3He$ reactions was demonstrated to deliver quasi-monochromatic neutrons with an energy spread of 10 % or less, which is determined primarily by the thermal velocity of the colliding ions. Such neutrons, in

conjunction with laser pulses may be used as a pump or probe in time resolved studies, whose capability is far beyond anything currently available. This promises to open up a new field of ultra fast neutron spectroscopy for structure studies in material and biological sciences. Even though the present neutron flux appears to be comparatively low, calculations in [141] have shown that a neutron flux from 10^{14} to 10^{15} per cm^2 and s may be achieved with 100 J lasers operating at 100 Hz. Those neutrons may indeed be used in studies on material damages at sub-ns time scales.

The generation of energetic and high quality electron beams with 10 Hz lasers was already shown within the scope of this work. Since additionally theoretical studies have shown, that the present lack of high energy electrons can be overcome at higher laser intensities, this approach to simultaneously generate and accelerate ultra short electron bunches to high energies will indeed be competitive or complementary with today's accelerators, e.g., by its implementation as a booster. But even in its present state it already demonstrated its suitability to explore ultra rapid chemical events, which may have applications in medicine, microdosimetry and radiology. Since the tunable electron beam temperature mets already today the requirements for cancer treatment, its direct utilization as well as its conversion into γ-rays are under consideration for radiotherapy.

Apart from the academical interest in proton generation with compact high intensity lasers, this small and bright source is perceived to be commercially viable by means of PET generation and, more ambiguous, proton therapy. Since the energy carried by the protons may be deposited in the human tissue at a desired depth, this unique proton source is potentially important for cancer therapy. Here, the simulated production of highly directional proton beams of up to 200 MeV [142] has tremendous promise in an enhanced cancer treatment in the near future. Clearly, due to its economical benefits this might permit to install laser induced proton sources in numerous hospitals – most likely more than accelerators could ever be.

It is noted that such an approach is currently under consideration within the scope of an European Program, Bioat / Propulse, where the tasks are to enhance the maximum proton energy, improve its angular divergence and control its generation, in terms of the strict requirements obliged for this delicate cancer treatment.

Considering additionally the rapid evolution of such "table top" lasers, which cost today about 1 million euros it is expected that their repetition rate will be increased in the very near future to the kHz regime while their cost will be reduced. Consequently, the availability of such laser plasma accelerators for universities and small, low-budget laboratories promises to open up a broad, deep and particularly prosperous spectrum of research.

Clearly, the future is, of course, full of challenges and uncertainties, but it is also full of exciting chances to make a difference ... [143].

Appendix A

List of Publications

A.1 Articles in Refereed Journals

1. *Large amplitude plasma wave generation using a high intensity short-pulse beat-wave*,
   B.R. Walton, Z. Najmudin, M.S. Wei, C. Marle, R.J. Kingham, K. Krushelnick, A.E. Dangor, R.J. Clarke, M.J. Poulter, C. Hernandez-Gomez, S. Hawkes, D. Neely, J.L. Collier, C.N. Danson, S. Fritzler, V. Malka, Opt. Lett. **27**, 24 (2002).

2. *Production of ultra-collimated bunches of multi-MeV electrons by 35 fs laser pulses propagating in exploding-foil plasmas*,
   D. Guilietti, M. Galimberti, A. Guilietti, L.A. Gizzi, R. Numico, P. Tomassini, M. Borghesi, V. Malka, S. Fritzler, M. Pittman, K. Taphuoc, A. Pukhov, Phys. Plasmas **9**, 3655 (2002).

3. *Relativistic electron generation in interactions of a 30 TW laser pulse with a thin foil target*,
   G. Malka, M.M. Aleonard, J.F. Chemin, G. Claverie, M.R. Harston, J.N. Scheurer, V. Tikhonchuk, S. Fritzler, V. Malka, P. Balcou, G. Grillon, S. Moustaizis, L. Notebaert, E. Lefebvre, N. Cochet, Phys. Rev. E **66**, 66402-664 (2002).

4. *Ion Heating and Thermonuclear Neutron Production from High-Intensity Subpicosend Laser Pulses Interacting with Underdense Plasmas*,
   S. Fritzler, Z. Najmudin, V. Malka, K. Krushelnick, C. Marle, B. Walton, M.S. Wei, R.J. Clarke, A.E. Dangor, Phys. Rev. Lett. **89**, 165004-1 (2002).

5. *Electron Acceleration by a Wakefield forced by an Intense Ultra-Short Laser Pulse*,
   V. Malka, S. Fritzler, E. Lefebvre, M.M. Aleonard, F. Burgy, J.P. Chambaret, J.F. Chemin, K. Krushelnick, G. Malka, S.P.D. Mangles, Z. Najmudin, M. Pittman, J.P. Rousseau, J.N. Scheurer, B. Walton, A.E. Dangor, Science **298**, 1596 (2002).

6. *Polychromatic X-ray production in helium from a femtosecond high-intensity laser system*,
   K. TaPhuoc, A. Rouse, L. Notebaert, M. Pittman, J.P. Rousseau, V. Malka,

S. Fritzler, S. Sebban, P. Balcou, D. Hulin, J.R. Marques, P.G. David, J. Opt. Soc. Am. B **20**, 221 (2003).

7. *Proton beams generated with high-intensity lasers : Applications to medical isotope production*,
S. Fritzler, V. Malka, G. Grillon, J. Rousseau, F. Burgy, E. Lefebvre, P. McKenna, E. d'Humières, K. Ledingham, Appl. Phys. Lett., in press.

8. *Self-modulated wakefield and forced laser wakefield acceleration of electrons*,
Z. Najmudin, K. Krushelnick, E.L. Clark, S.P.D. Mangles, B. Walton, A.E. Dangor, S. Fritzler, V. Malka, E. Lefebvre, D. Gordon, F.S. Tsung, C. Joshi, Phys. Plasmas **10**, 2071 (2003).

9. *The effect of high intensity laser propagation instabilities on channel formation in underdense plasmas*,
Z. Najmudin, K. Krushelnick, M. Tatarakis, E.L. Clark, C.N. Danson, V. Malka, D. Neely, M.I.K. Santala, A.E. Dangor, S. Fritzler, Phys. Plasmas **10**, 2 (2003).

10. *Practicability of protontherapy induced by table-top laser systems*,
V. Malka, S. Fritzler, R. Ferrand, G. Grillon, C. Albaret, S. Meyroneinc, J.P. Chambaret, A. Antonetti, D. Hulin, submitted to Med. Phys. (2003).

11. *Ultra-short electron bunches generated with high-intensity lasers for injectors and X-ray sources*,
S. Fritzler, K. TaPhuoc, V. Malka, A. Rousse, E. Lefebvre, submitted to Appl. Phys. Lett. (2003).

12. *Real-time observation of relativistic electron-induced ionizing events in water*,
Y. Gauduel, A. Hallou, S. Fritzler, G. Grillon, J.P. Chambaret, J.P. Rousseau, F. Burgy, D. Hulin, V. Malka, submitted to Nature (2003).

13. *Electron and photon production from relativistic laser-plasma interactions*,
E. Lefebvre, N. Cochet, S. Fritzler, V. Malka, M.M. Aleonard, J.F. Chemin, S. Darbon, L. Disdier, J. Faure, A. Fedotoff, O. Landoas, G. Malka, V. Meot, P. Morel, M. Rabec Le Gloahec, A. Rouyer, Ch. Rubbelynck, V. Tikhonchuk, R. Wrobel, P. Audebert, C. Rousseaux, submitted to Nucl. Fusion (2002).

14. *Investigation of Channelling Radiation at High Bunch Charge Densities*,
R.A. Carrigan Jr., J. Freudenberger, S. Fritzler, H. Genz, A. Ushakov, A. Richter, A. Zilges, J.P.F. Sellschop, submitted to Phys. Rev. E (2003).

15. *Beam quality studies for the laser-plasma accelerator concept*,
S. Fritzler, E. Lefebvre, V. Malka, M.M. Aleonard, F. Burgy, J.P. Chambaret, J.F. Chemin, K. Krushelnick, G. Malka, S. Mangles, Z. Najmudin, M. Pittman, J.P. Rousseau, J.N. Scheurer, B. Walton, A.E. Dangor, in preparation for Phys. Rev. Lett..

16. *Observation of late-time ionic remnants of wakefield oscillations following ultra-intense laser plasma interaction*,
L. Romagnani, S. Kar, M. Borghesi, A. Schiavi, S. Fritzler, V. Malka, M.G. Haines, in preparation for Phys. Rev. Lett..

A.2 Articles in Non-Refereed Journals

1. *Beam dynamics studies in a high brightness photoinjector*,
J.P. Carneiro, N. Barov, R.A. Carrigan, P. Colestock, H. Edwards, M. Fitch, S. Fritzler, W. Hartung, K. Koepke, FERMILAB-CONF-99-271 (1999).

2. *Probing towards the Solid State Plasma Accelerator Frontier using Channeling Radiation Measurements at the Fermilab A0 Photo-Injector*,
R.A. Carrigan Jr., J. Freudenberger, S. Fritzler, H. Genz, A. Richter, A. Ushakov, A. Zilges, J.P.F. Sellshop, FERMILAB-CONF-01/029-E (2001).

3. *Nuclear physics with powerful laser pulses*,
G. Malka, M.M. Aleonard, J.F. Chemin, G. Calverie, M.R. Harston, J.N. Scheurer, V. Tickonchuck, S. Fritzler, V. Malka, P. Balcou, G. Grillon, S. Moustaizis, E. Lefebvre, V. Meot, IFSA Kyoto (2001).

4. *Optimizing photo-nuclear reactions with the 2 J, 30 fs LOA laser*,
G. Malka, M.M. Aleonard, J.F. Chemin, G. Calverie, J.N. Scheurer, V. Tickonchuck, S. Fritzler, V. Malka, P. Balcou, G. Grillon, S. Moustaizis, E. Lefebvre, SPI San Diego (2001).

5. *Electron Acceleration beyond 200 MeV in Underdense Plasmas using Table Top Laser Systems*,
S. Fritzler, V. Malka, E. Lefebvre, M.M. Aleonard, F. Burgy, J.P. Chambaret, J.F. Chemin, K. Krushelnick, G. Malka, S. Mangles, Z. Najmudin, J.P. Rousseau, J.N. Scheurer, B. Walton, A.E. Dangor, CP 647 Advanced Accelerator Conference Proceedings, Tenth Workshop (2002).

6. *Electron and photon production from relativistic laser-plasma interactions*,
E. Lefebvre, M.M. Aleonard, J.F. Chemin, N. Cochet, S. Darbon, L. Disdier, J. Faure, A. Fedotoff, S. Fritzler, O. Landoas, G. Malka, V. Malka, V. Meot, P. Morel, M. Rabec Le Gloahec, A. Rouyer, C. Rousseaux, Ch. Rubbelynck, V. Tikhonchuk, R. Wrobel, P. Audebert, Proc. Lyon's Fusion Energy Conf. (2002).

7. *Excitation of relativistic electron plasma waves by the short-pulse beatwave process*,
B.R. Walton, Z. Najmudin, M.S. Wei, C. Marle, K. Krushlenick, A.E. Dangor,

R.J. Clarke, M.J. Poulter, C. Hernandez-Gomez, S. Hawkes, D. Neely, C.N. Danson, J.L. Collier, S. Fritzler, V. Malka, Central Laser Facility, RAL-TR-2001-030 (2001).

8. *Relativistic electron generation in interaction of a 30 TW laser pulse with thin foil target*,
G. Malka, M.M. Aleaonard, J.F. Chemin, G. Calverie, M.R. Harston, J.N. Scheurer, V. Tickonchuck, S. Fritzler, V. Malka, P. Balcou, G. Grillon, E. Lefebvre, XXVII European Conference on Laser Interaction with Matter, Moscou ECLIM (2002).

Bibliography

[1] F. Abe, *Observation of top quark production in $\bar{p}p$ collisions with the collider detector at Fermilab*, Phys. Rev. Lett. **74**, 2626 (1995).

[2] S.L. Wu, *Discovery of the gluon*, AIP Conf. Proc. **300**, 598 (1994).

[3] F. Keffer, *Spin waves*, Encyclo. of Physics **18/2** (1966).

[4] D.A. Edwards, *TESLA Test Facility Linac – Design Report*, TESLA 95-01, DESY (1995).

[5] D. Strickland, G. Mourou, *Compression of amplified chirped optical pulses*, Opt. Comm. **56**, 219 (1985).

[6] T. Tajima, J. Dawson, *Laser electron accelerator*, Phys. Rev. Lett. **43**, 267 (1979).

[7] A. Modena, A.E. Dangor, Z. Najmudin, C. Clayton, K. Marsh, C. Joshi, V. Malka, C. Darrow, D. Neely, F. Walsh, *Electron acceleration from the breaking of electron plasma waves*, Nature **377**, 606 (1995).

[8] E.L. Clark, K. Krushelnick, J.R. Davies, M. Zepf, M. Tatarakis, F.N. Beg, A. Machacek, P.A. Norreys, M.I.K. Santala, I. Watts, A.E. Dangor, *Measurement of energetic proton transport through magnetized plasma from intense laser interactions with solids*, Phys. Rev. Lett. **84** 670 (2000).

[9] V. Malka, S. Fritzler, E. Lefebvre, M.M. Aleonard, F. Burgy, J.P. Chambaret, J.F. Chemin, K. Krushelnick, G. Malka, S.P.D. Mangles, Z. Najmudin, M. Pittman, J.P. Rousseau, J.N. Scheurer, B. Walton, A.E. Dangor, *Electron Acceleration by a Wakefield forced by an Intense Ultra-Short Laser Pulse*, Science **298**, 1596 (2002).

[10] M. Tatarakis, I. Watts, F.N. Beg, E.L. Clark, A.E. Dangor, A. Gopal, M.G. Haines, P.A. Norreys, U. Wagner, M.-S. Wei, M. Zepf, K. Krushelnick, *Measuring huge magnetic fields*, Nature **415**, 280 (2002).

[11] F.K. Kneubühl, *Oscillation and Waves*, Springer-Verlag, Berlin (1997).

[12] K. Thyagarajan, A.K. Ghatak, *Lasers, Theory and Applications*, Plenum Press, New York (1981).

[13] W.L. Kruer, *The Physics of Laser Plasma Interactions*, Addison-Wesley Publishing Company, New York (1988).

[14] B. Quesnel, P. Mora, *Theory and simulation of the interaction of ultra-intense laser pulses with electrons in vacuum*, Phys. Rev. E **58**, 3718 (1998).

[15] L.V. Keldysh, *Ionisation in the field of a strong electromagnetic wave*, Sov. Phys. JETP **20**, 1307 (1965).

[16] M.V. Ammosov, N.B. Delone, V.P. Krainov, *Tunnel ionization of complex atoms and atomic ions by an alternating electromagnetic field*, Sov. Phys. JETP **64**, 1191 (1986).

[17] S. Augst, D.D. Meyerhofer, D. Strickland, S.L. Chin, *Laser ionization of noble gas by coulomb barrier suppression*, J. Opt. Soc. Am. B **8**, 858 (1991).

[18] J. Faure, *Étude expérimentale de l'interaction d'un laser Terawatt avec un plasma sous-dense : production d'une source brillante et courte d'électrons relativiste*, Ph.D Thesis, École Polytechnique (2001).

[19] D. Bauer, P. Mulser, *Relativistic ponderomotive force, uphill acceleration, and transistion to chaos*, Phys. Rev. Lett. **75**, 4622 (1995).

[20] M.V. Ammosov, N.B. Delone, V.P. Krainov, *Tunnel ionisation of complex atoms and atomic ions in an alternating electromagnetic field*, Sov. Phys. JETP **64**, 1191 (1987).

[21] F. Vidal, T.W. Johnston, S. Laville, O. Barthélemy, M. Chaker, B. Le Drogoff, J. Margot, M. Sabsabi, *Critical-Point Phase Separation in Laser Ablation of Conductors*, Phys. Rev. Lett. **86**, 2573 (2001).

[22] National Nuclear Data Center, http://www.nndc.bnl.gov.

[23] C. Joshi, T. Tajima, J.M. Dawson, H.A. Baldis, N.A. Ebrahim, *Forward Raman instability and electron acceleration*, Phys. Rev. Lett. **47**, 1285 (1981).

[24] W.B. Mori, C. Joshi, J.M. Dawson, D.W. Forslund, J.M. Kindel, *Evolution of self-focusing of intense electromagnetic waves in plasma*, Phys. Rev. Lett. **60**, 1298 (1988).

[25] C.J. McKinstrie, R. Bingham, *Stimulated Raman forward scattering and the relativistic modulational instability of light waves in rarefied plasma*, Phys. Fluids B **4**, 2626 (1992).

[26] J.F. Drake, P.K. Kaw, Y.C. Lee, G. Schmidt, C.S. Liu, M.N. Rosenbluth, *Parametric instabilities of electromagnetic waves in plasmas*, Phys. Fluids **17**, 778 (1974).

[27] C.D. Decker, W.B. Mori, T. Katsouleas, *Particle-in-cell Simulations of Raman Forward Scattering from Short-Pulse High-Intensity lasers*, Phys. Rev. E **50**, R3338 (1994).

[28] W.B. Mori, *The Physics of the Nonlinear Optics of Plasmas at Relativistic Intensities for Short-Pulse Lasers*, IEEE Journal of Quantum Electronics **33**, 1 (1997).

[29] C.D. Decker, W.B. Mori, *Group velocity of large-amplitude electromagnetic waves in a plasma*, Phys. Rev. Lett. **72**, 490 (1994).

[30] C.E. Max, J. Arons, A.B. Langdon, *Self-Modulation and Sel-Focusing of Electromagnetic Waves in Plasmas*, Phys. Rev. Lett. **33**, 526 (1974).

[31] S.C. Wilks, J.M. Dawson, W.B. Mori, T. Katsouleas, M.E. Jones, *Photon accelerator*, Phys. Rev. Lett. **62**, 2600 (1989).

[32] P. Monot, T. Auguste, P. Gibbon, F. Jakober, G. Mainfray, A. Dulieu, M. Louis-Jacquet, G. Malka, J.L. Miquel, *Experimental demonstration of relativistic self-channeling of a multiterawatt laser pulse in an underdense plasma*, Phys. Rev. Lett. **74**, 2953 (1995).

[33] K. Krushelnick, A. Ting, C.I. Moore, H.R. Burris, E. Eseray, P. Sprangle, M. Baine, *Plasma channel formation and guiding during high intensity short pulse laser plasma experiment*, Phys. Rev. Lett. **78**, 4047 (1997).

[34] A. Pukhov, J. Meyer-ter-Vehn, *Relativistic magnetic self-channeling of light in near-critical plasmas. Three-simensional PIC simulation*, Phys. Rev. Lett. **76**, 3975 (1996).

[35] J.M. Dawson, *Nonlinear electron oscillation in a cold plasma*, Phys. Rev. **133**, 383 (1959).

[36] E. Esarey, M. Pilloff, *Trapping and acceleration in nonlinear plasma waves*, Phys. Plasmas **2**, 1432 (1995).

[37] A.I. Akhiezer, R.V. Polovin, *Theory of wave motion of an electron plasma*, Sov. Phys. JETP **3**, 696 (1956).

[38] T. Katsouleas, W.B. Mori, *Wave-breaking amplitude of relativistic oscillations in a thermal plasma*, Phys. Rev. Lett. **61**, 90 (1988).

[39] P. Mora, F. Amiranoff, *Electron acceleration in a relativistic electron plasma wave*, J. Appl. Phys. **66**, 3476 (1989).

[40] T. Katsouleas, *Plasma accelerator*, AIP Conf. Proc. **130**, 63 (1985).

[41] C.J. McKinstrie, D.F. DuBois, *A covariant formalism for wave propagation applied to stimulated Raman scattering*, Phys. Fluids **31**, 278 (1988).

[42] G.S. Sarkisov, V.Yu. Bychenkov, V.N. Novikov, V.T. Tikhonchuk, A. Maksimchuk, S.Y. Chen, R. Wagner, G. Mourou, D. Umstadter, *Self-focusing, channel formation, and high-energy ion generation in interaction of an intense short laser pulse with a He jet*, Phys. Rev. E **59**, 7042 (1999).

[43] V.Yu. Bychenkov, V.T. Tikhonchuk, S.V. Tolokonnikov, *Nuclear reactions triggered by laser-accelerated high-energy ions*, J. Exp. Theo. Phys. **88**, 1137 (1999).

[44] K. Krushelnick, E.L. Clark, Z. Najmudin, M. Salvati, M.I.K. Santala, M. Tatarakis, A.E. Dangor, V. Malka, D. Neely, R. Allot, C. Danson, *Multi-MeV Ion Production from High-Intensity Laser Interactions with Underdense Plasmas*, Phys. Rev. Lett. **83**, 737 (1999).

[45] S.C. Wilks, W.L. Kruer, M. Tabak, A.B. Langdon, *Absorption of ultra-intense laser pulses*, Phys. Rev. Lett. **69**, 1383 (1992).

[46] A. Pukhov, J. Meyer-ter-Vehn, *Laser hole boring into overdense plasma and relativistic electron currents for fas ignition of ICF targets*, Phys. Rev. Lett. **79**, 2686 (1997).

[47] G. Malka, J.L. Miquel, *Experimental Confirmation of Ponderomotive-Force Electrons Produced by an Ultrarelativistic Laser Pulse on a Solid Target*, Phys. Rev. Lett **77**, 75 (1996).

[48] G. Malka, M.M. Aleonard, J.F. Chemin, G. Claverie, M.R. Harston, J.N. Scheurer, V. Tikhonchuk, S. Fritzler, V. Malka, P. Balcou, G. Grillon, S. Moustaizis, L. Notebaert, E. Lefebvre, N. Cochet, *Relativistic electron generation in interactions of a 30 TW laser pulse with a thin foil target*, Phys. Rev. E **66**, 66402-664 (2002).

[49] A. Pukhov, *Three-Dimensional Simulations of Ion Acceleration from a Foil Irradiated by a Short-Pulse Laser*, Phys. Rev. Lett. **86**, 3562 (2001).

[50] P. Mora, *Plasma expansion into a vacuum*, Phys. Rev. Lett. **90**, 185002 (2003).

[51] E. Lefebvre, G. Bonnaud, *Transparency / opacity of a solid target illuminated by an ultrahigh-intensity laser pulse*, Phys. Rev. Lett. **74**, 2002 (1995).

[52] J. Denavit, *Absorption of high-intensity subpicosecond lasers on solid density targets*, Phys. Rev. Lett. **69**, 3052 (1992).

[53] R.A. Snavely, M.H. Key, S.P. Hatchett, T.E. Cowan, M. Roth, T.W. Philips, M.A. Stoyer, E.A. Henry, T.C. Sangster, M.S. Singh, S.C. Wilks, A. MacKinnon, A. Offenberger, D.M. Pennington, K. Yasuike, A.B. Langdon, B.F. Lasinski, J. Johnson, M.D. Perry, E.M. Campbell, *Intense high-energy proton beams from Petawatt-laser irradiation of solids*, Phys. Rev. Lett. **85**, 2945 (2000).

[54] J.E. Crow, P.L. Auer, J.E. Allen, *The expansion of a plasma into a vacuum*, J. Plasma Phys. **14**, 65 (1975).

[55] J.S. Pearlman, R.L. Morse, *Maximum expansion velocities of laser-produced plasmas*, Phys. Rev. Lett. **40**, 1652 (1978).

[56] S.C. Wilks, A.B. Langdon, T.E. Cowan, M. Roth, M. Singh, S. Hatchett, M.H. Key, D. Pennington, A. MacKinnin, R. Snavely, *Energetic proton generation in ultra-intense laser-solid interactions*, Phys. Plasmas **8**, 542 (2001).

[57] K. Krushelnick, E.L. Clark, M. Zepf, J.R. Davies, F.N. Beg, A. Machacek, M.I.K. Santala, M. Tatarakis, I. Watts, P.A. Norreys, A.E. Dangot, *Energetic proton production from relativistic laser interaction with high density plasmas*, Phys. Plasmas **7**, 2055 (2000).

[58] S.P. Hatchett, C.G. Brown, T.E. Cowan, E.A. Henry, J.S. Johnson, M.H. Key, J.A. Koch, A.B. Langdon, B.F. Lasinski, R.W. Lee, A.J. Mackinnon, D.M. Pennington, M.D. Perry, T.W. Philips, M. Roth, T.C. Sangster, M.S. Singh, R.A. Snavely, M.A. Stoyer, S.C. Wilks, K. Yasuike, *Electron, photon, and ion beams from the relativistic interaction of Petawatt laser pulses with solid targets*, Phys. Plasmas **7**, 2076 (2000).

[59] L. Gremillet, F. Amiranoff, S.D. Baton, J.C. Gauthier, M. Koenig, E. Martinolli, F. Pisani, G. Bonnaud, C. Lebourg, C. Rousseaux, C. Toupin, A. Antonicci, D. Batani, A. Bernardinello, T. Hall, D. Scott, P.N. Norreys, H. Bandulet, H. Pépin, *Time-resolved observation of ultrahigh intensity laser-produced electron jets propagating through transparent solid targets*, Phys. Rev. Lett. **83**, 5015 (1999).

[60] Z. Jiang, J.C. Kieffer, J.P. Matte, M. Chaker, O. Peyrusse, D. Gilles, G. Korn, A. Maksimchuk, S. Coe, G. Mourou, *X-ray spectroscopy of hot solid density plasmas produced by subpicosecond high contrast laser pulses at* $10^{18} - 10^{19}$ W/cm^2, Phys. Plasmas **2**, 1702 (1995).

[61] K. Wirtz and K.H. Beckurts, *Elementare Neutronenphysik*, Springer-Verlag, Berlin (1958).

[62] G. Pretzler, A. Saemann, A. Pukhov, D. Rudolph, T. Schätz, U. Schramm, P. Thirolf, D.Habs, K. Eidmann, G.D. Tsakiris, J. Meyer-ter-Vehn, K.J. Witte, *Neutron production by 200 mJ ultrashort laser pulses*, Phys. Rev. E **58**, 1165 (1998).

[63] P.A. Norreys, A.P. Fews, F.N. Beg, A.R. Bell, A.E. Dangor, P. Lee, M.B. Nelson, H. Schmidt, M. Tatarakis, M.D. Cable, *Neutron production from picosecond laser irradiation of deuterated targets at intensities of* 10^{19} W/cm^{-2}, Plasma Phys. Control. Fusion **40**, 175 (1998).

[64] L. Disdier, J.P. Garçonnet, G. Malka, J.L. Miquel, *Fast Neutron Emission from High-Energy Ion Beam Prodeced by a High-Intensity Subpicosecond Laser Pulse*, Phys. Rev. Lett. **82**, 1454 (1999).

[65] T. Ditmire, J. Zweiback, V.P. Yanovsky, T.E. Cowan, G. Hays, K.B. Wharton, *Nuclear fusion from explosions of femtosecond laser-heated deuterium clusters*, Nature **398**, 489 (1999).

[66] G. Grillon, Ph. Balcou, J.P. Chambaret, D. Hulin, J. Martino, S. Moustaizis, L. Notebaert, M. Pittman, Th. Pussieux, A. Rousse, J.P. Rousseau, S. Sebban, O. Sublemontier, M. Schmidt, *Deuterium-Deuterium Fusion Dynamics in Low-Density Molecular-Cluster Jets Irradiated by Intense Ultrafast Laser Pulses*, Phys. Rev. Lett. **89**, 065005-1 (2002).

[67] J.B. Marion and R. Fowler, Edt., *Fast Neutron Physics, Part I*, Interscience Publishers, Inc., New York (1960).

[68] H. Brysk, *Fusion Neutron Energies and Spectra*, Plasma Phys. **15**, 611 (1973).

[69] I.H. Hutchinson, *Principles of Plasma Diagnostics*, Cambridge University Press, Cambridge (1987).

[70] D. Strickland, G. Mourou, *Compression of Amplified Chirped Optical Pulses*, Opt. Comm. **56**, 291 (1985).

[71] C.N. Danson, J. Collier, D. Neely , L.J. Barzanti, A. Damerell, C.B. Edwards, M.H.R. Hutchinson, M.H. Key, P.A. Norreys, D.A. Pepler, I.N. Ross, P.F. Taday, W.T. Toner, M. Trentelman, F.N. Walsh, T.B. Winstone, R.W.W. Wyatt, *Well characterized* 10^{19} *W/cm*^{2} *operation of VULCAN – An ultra-high power Nd:glass laser*, J. Mod. Opt. **45**, 1653 (1998).

[72] V. Malka, C. Coulaud, J.P. Geindre, V. Lopez, Z. Najmudin, D. Neely, F. Amiranoff, *Characterization of neutral density profile in a wide range of pressure of cylindrical pulsed gas jets*, Rev. Sci. Instr. **71**, 6 (2000).

[73] W.B. Mori, C.D. Decker, D.E. Hinkel, T. Katsouleas, *Raman forward scattering of short-pulse high-intensity lasers*, Phys. Rev. Lett. **72**, 1482 (1994).

[74] C.D. Decker, W.B. Mori, T. Katsouleas, D.E. Hinkel, *Spatial temporal theory of Raman forward scattering*, Phys. Plasmas **3**, 1360 (1996).

[75] A. Modena, *Electron Acceleration by the creation of high amplitude plasma waves*, Ph.D Thesis, University of London (1996).

[76] Z. Najmudin, *Parametric Instabilities in the Interaction of High-Intensity Short-Pulse Lasers with Under-Dense Plasmas*, Ph.D Thesis, University of London (1995).

[77] B.G. Cartwright, E.K. Shirk, P.B. Price, *A nuclear-track-recording polymer of unique sensitivity and resolution*, Nucl. Instr. Meth. **153**, 457 (1978).

[78] W.L. McLaughlin, C. Yun-Dong, C.G. Soares, A. Miller, G. Van Dyk, D.F. Lewis, *Sensitometry of the response of a new radiochromic film dosimeter to gamma radiation and electron beams*, Nucl. Instr. Meth. **A302**, 165 (1991).

[79] Gafchromic film, http://www.ispcorp.com.

[80] E.L. Clark, *Measurements of Energetic Particles from Ultra Intense Laser Plasma Interactions*, Ph.D Thesis, University of London (2001).

[81] Philips Photomultipliers, http://www.philips.com.

[82] W.R. Leo, *Techniques for Nuclear and Particle Physics Experiments*, Springer-Verlag, Berlin (1994).

[83] Tektronix Oscilloscopes, http://www.tektronix.com.

[84] A. Hughes, A. Schwartz, *Neutron Cross Sections*, BNL325 (1958).

[85] S. Glasstone, M.C. Edlund, *Kernreaktortheorie*, Springer-Verlag, Wien (1961).

[86] J.F. Briesmeister, Edt., *MCNP Code*, Los Alamos Report No. LA-12625-M (1993).

[87] V.V. Goloviznin, T.J. Schep, *Production of direct fusion neutrons during ultra-intense laser-plasma interaction*, J. Phys. D: Appl. Phys. **31**, 3243 (1998).

[88] K.-C. Tzeng, W. B. Mori, *Suppression of Electron Ponderomotive Blowout and Relativistic Self-Focusing by the Occurrence of Raman Scattering and Plasma Heating*, Phys. Rev. Lett. **81**, 104 (1998).

[89] M.I.K. Santala, Z. Najmudin, E.L. Clark, M. Tatarakis, K. Krushelnick, A.E. Dangor, V. Malka, J. Faure, R. Allott, R.J. Clarke, *Observation of a Hot High-Current Electron Beam from a Self-Modulated Laser Wakefield Accelerator*, Phys. Rev. Lett. **86**, 1227 (2001).

[90] M. Honda, J. Meyer-ter-Vehn, A. Pukhov, *Collective Stopping and Ion Heating in Relativistic-Electron-Beam Transport for Fast Ignition*, Phys. Rev. Lett. **85**, 2128 (2000).

[91] D. Gordon, K.C. Tzeng, C.E. Clayton, A.E. Dangor, V. Malka, K.A. Marsh, A. Modena, W.B. Mori, P. Muggli, Z. Najmudin, D. Neely, C. Danson, C. Joshi, *Observation of electron energies beyond the linear dephasing limit from a laser-excited relativistic plasma wave*, Phys. Rev. Lett. **80**, 2133 (1998).

[92] C.E. Clayton, K.C. Tzeng, D. Gordon, P. Muggli, W.B. Mori, C. Joshi, V. Malka, Z. Najmudin, A. Modena, D. Neely, A.E. Dangor, *Plasma wave generation in a self-focused channel of a relativistically intense laser pulse*, Phys. Rev. Lett. **81**, 100 (1998).

[93] C. Gahn, G.D. Tsakiris, A. Pukhov, J. Meyer-ter-Vehn, G. Pretzler, P. Thirolf, D. Habs, K.J. Witte, *Multi-MeV electron beam generation by direct laser acceleration in high-density plasma channels*, Phys. Rev. Lett. **83**, 4772 (1999).

[94] V. Malka, J. Faure, J.R. Marques, F. Amiranoff, J.P. Rousseau, S. Ranc, J.P. Chambaret, Z. Najmudin, B. Walton, P. Mora, A. Solodov, *Characterization of electron beams produced by ultra-short (30 fs) laser pulses*, Phys. Plasmas **8**, 2605 (2001).

[95] K. Nakajima, D. Fisher, T. Kawakubo, H. Nakanishi, A. Ogata, Y. Kato, Y. Kitagawa, R. Kodema, K. Mima, H. Shiraga, K. Suzuki, K. Yamakawa, T. Zhang, Y. Sakawa, T. Shoji, Y. Nishida, N. Yugami, M. Downer, T. Tajima, *Observation of ultrahigh gradient electron acceleration by a self-modulated intense short pulse laser*, Phys. Rev. Lett. **74**, 4428 (1995).

[96] M. Pittman, S. Ferré, J.P. Rousseau, L. Notebaert, J.P. Chambaret, G. Chériaux, *Design and characterization of a near-diffraction-limited femtosecond 100-TW 10-Hz high-intensity laser system*, Appl. Phys. B **74**, 529 (2002).

[97] Electron and proton stopping powers, http://physics.nist.gov.

[98] Bergoz Instrumentation, http://www.bergoz.com.

[99] C. Caso, *Review of Particle Physics, The Euopean Physical Journal* **C3** (1998).

[100] GEANT 4, LCB Status Report/RD, CERN/LHCC-98-44 (1998).

[101] K. Wille, *Physik der Teilchenbeschleuniger und Synchrotronstrahlungsquellen*, Teubner Studienbücher, Stuttgart (1996).

[102] Y. Yamazaki, T. Kurihara, H. Kobayashi, I. Sato, A. Asami, *High-precision pepper-pot technique for low-emittance electron beam*, Nucl. Instr. Meth. A **322**, 139 (1992).

[103] A. Pukhov, J. Meyer-ter-Vehn, *Laser wake field acceleration : the highly non-linear broken-wave regime*, Appl. Phys. B **74**, 355 (2002).

[104] W.P. Leemans, C.W. Siders, E. Esarey, N.E. Andreev, G. Shvets, W.B. Mori, *Plasma Guiding and Wakefield Generation for Second-Generation Experiments*, IEEE Trans. Plasma Sci. **24**, 331 (1996).

[105] E. Lefebvre, private communication.

[106] Z. Najmudin, A.E. Dangor, A. Modena, M.R. Salvati, C.E. Clayton, C.N. Danson, D.F. Gordon, C. Joshi, K.A. Marsh, V. Malka, P. Muggli, D. Neely, F.N. Walsh, *Investigation of a channeling high-intensity laser beam in underdense plasmas*, IEEE Trans. Plasma Sci. **28**, 1057 (2000).

[107] Z. Najmudin, K. Krushelnick, E.L. Clark, S.P.D. Mangles, B. Walton, A.E. Dangor, S. Fritzler, V. Malka, E. Lefebvre, D. Gordon, C. Joshi, *Self-modulated wakefield and forced laser wakefield acceleration of electrons*, submitted to Phys. Plasmas (2003).

[108] C.D. Jonah, B.S.M. Medhava Rao, Edt. *Radiation chemistry : present status and future trends*, Elsevier Science B.V., New York (2001).

[109] Y. Gauduel, private communication.

[110] Y. Gauduel, S. Pommeret, A. Migus, A. Antonetti, *Some evidence of ultrafast H_2O^+-water molecule reaction in femtosecond photoionization of pure liquid water*, Chem. Phys. **149**, 1 (1990).

[111] Y. Gauduel, A. Hallou, B. Charles, *Short-time water caging and elementary prehydration redox reactions in ionic environments*, J. Phys. Chem. A **107**, 2011 (2003).

[112] C.Y. Yang, K.F. Wong, M.S. Skaf, P.J. Rossky, *Instantaneous normal mode analysis of hydrated electron solvation dynamics*, J. Chem. Phys. **114**, 3598 (2001).

[113] D.M. Bartels, A.R. Cook, M. Mudaliar, C.D. Jonah, *Spur decay of the solvated electron in picosecond radiolysis measured with time-correlated absorption spectroscopy*, J. Phys. Chem. A **104**, 1686 (2000).

[114] Y. Gauduel, A. Hallou, S. Fritzler, G. Grillon, J.P. Chambaret, J.P. Rousseau, F. Burgy, D. Hulin, V. Malka, *Real-time observation of relativistic electron-induced ionizing events in water*, submitted to Nature (2003).

[115] A. Richter, *Electron channelling radiation : first steps towards a bright and tunable X-ray source*, Mat. Sci. Eng. **B11**, 139 (1992) and references herein.

[116] M.A. Kumakhov, R. Wedell, *Radiation of Relativistic Light Particles during Interaction with Single Crystals*, Spektrum Akademischer Verlag, Heidelberg (1991).

[117] U. Nething, M. Galemann, H. Genz, M. Höfer, P. Hoffmann-Stascheck, J. Hormes, A. Richter, J.P.F. Sellschop, *Intensity of electron channelling radiation and occupation lengths in diamond crystals*, Phys. Rev. Lett. **72**, 2411 (1994).

[118] P. Catravas, E. Esarey, W.P. Leemans, *Femtosecond X-rays from Thomson scattering using laser wakefield accelerators*, Meas. Sci. Technol. **12**, 1828 (2001).

[119] W.P. Leemans, S. Chattopadhyay, E. Esarey, A. Zholents, M. Zolotorev, A. Chin, R. Schoenlein, C.V. Shank, *Femtosecond X-ray generation through relativistic electron beam - laser interaction*, C.R. Acad. Sci. Paris **1**, 279 (2000).

[120] J.T. Mendonça, J.R. Davies, M. Eloy, *Proton and neutron sources using terawatt lasers*, Meas. Sci. Technol. **12**, 1801 (2001).

[121] K. Nemoto, A. Maksimchuk, S. Banerjee, K. Flippo, G. Mourou, D. Umstadter, V.Yu. Bychenkov, *Laser-triggered ion acceleration and table top isotope production*, Appl. Phys. Lett. **78**, 595 (2001).

[122] A.J. Mackinnon, J. Sentoku, P.K. Patel, D.W. Price, M.H. Key, C. Andersen, R. Snavely, R.R. Freeman, *Enhancement of proton acceleration by hot-electron recirculation in thin foils irradiated by ultraintense laser pulses*, Phys. Rev. Lett **88**, 215006 (2002).

[123] I. Spencer, K.W.D. Ledingham, P. McKenna, T. McCanny, R.P.S. Singhal, P.S. Foster, D. Neely, A.J. Langley, E.J. Divall, C.J. Hooker, R.J. Clark, P.A. Norreys, E.L. Clark, K. Krushelnick, J.R. Davies, *Experimental study of proton emission from 60-fs, 200-mJ high-repetition-rate tabletop-laser pulses interacting with solid targets*, Phys. Rev. E **67**, 046402 (2003).

[124] R. Fabbro, *Etude de l'influence de la longueur d'onde laser sur les processus de conduction thermique et d'ablation dans les plasmas créés par laser*, Ph.D Thesis, University of Orsay (1982).

[125] V.T. Tikhonchuk, *Interaction of a beam of fast electrons with solids*, Phys. Plasmas **9**, 1416 (2002).

[126] M. Manclossi, Ph.D Thesis, École Polytechnique, in preparation.

[127] E. d'Humières, Ph.D Thesis, École Polytechnique, in preparation.

[128] M.I.K. Santala, M. Zepf, I. Watts, F.N. Beg, E. Clark, M. Tatarakis, A.E. Dangor, T. McCanny, I. Spencer, R.P. Singhal, K.W.D. Ledingham, S.C. Wilks, A.C. Machacek, J.S. Wark, R. Allott, R.J. Clark, P.A. Norreys, *Effect of the plasma density scale length on the direction of fast electrons in relativistic laser-solid interaction*, Phys. Rev. Lett. **84**, 7 (2000).

[129] I. Spencer, K.W.D. Ledingham, R.P. Singhal, T. McCanny, P. Mckenna, E.L. Clark, K. Krushelnick, M. Zepf, F.N. Beg, M. Tatarakis, A.E. Dangor, P.A. Norreys, R.J. Clarke, R.M. Allott, I.N. Ross, *Laser generation of proton beams for the production of short-lived positron emitting radioisotopes*, Nucl. Instr. Meth. B **183**, 449 (2001).

[130] M.I.K. Santala, M. Zepf, F.N. Beg, E.L. Clark, A.E. Dangor, K. Krushelnick, M. Tatarakis, I. Watts, K.W.D. Ledingham, T. McCanny, I. Spencer, A.C. Machacek, R. Allot, R.J. Clarke, P.A. Norreys, *Production of radioactive nuclides by energetic protons generated from intense laser-plasma interactions*, Appl. Phys. Lett. **78**, 19 (2001).

[131] P. McKenna, K.W.D. Ledingham, private communication.

[132] J.A. Cooksen, *Radiography with Protons*, Naturwissenschaften **61**, 184 (1974).

[133] U. Schneider, E. Pedroni, *Proton radiography as a tool for quality control in proton therapy*, Med. Phys. **22**, 353 (1995).

[134] N.S.P. King, E. Ables, K. Adams, K.R. Alrick, J.F. Amann, S. Balzar, P.D. Barnes Jr., M.L. Crow, S.B. Cushing, J.C. Eddleman , *An 800-MeV proton radiography facility for dynamic experiments*, Nucl. Instr. Meth. A **424**, 84 (1999).

[135] M. Borghesi, A. Schiavi, D.H. Campbell, M.G. Haines, O. Willi, A.J. MacKinnon, L.A. Gizzi, M. Galimberti, R.J. Clarke, H. Ruhl, *Proton imaging : a diagnostic for inertial confinement fusion / fast ignitor studies*, Plasma Phys. Control. Fusion **43**, A267 (2001).

[136] L. Romagnani, Ph.D Thesis, Queen's University of Belfast, in preparation.

[137] M. Borghesi, private communication.

[138] V. V. Goloviznin, T.J. Schep, *Production of direct fusion neutrons during ultra-intense laser-plasma interaction*, J. Appl. Phys. D **31**, 3243 (1998).

[139] J.P. Chambaret, private communication.

[140] Osram Sylvania Inc., http://www.sylvania.com.

[141] L.J. Perkins, B.G. Logan, M.D. Rosen, M.D. Perry, T. Diaz de la Rubia, N.M. Ghoniem, T. Ditmire, P.T. Springer, S.C. Wilks, *The investigation of high intensity laser driven micro neutron sources for fusion materials research at high fluence*, Nucl. Fusion **40**, 1 (2000).

[142] E. Fourkal, B. Shahine, M. Ding, J.S. Li, T. Tajima, C.M. Ma, *Particle in cell simulation of laser-accelerated proton beam for radiation therapy*, Med. Phys. **29**, 2788 (2002).

[143] C. Joshi, T. Katsouleas, *Plasma Accelerators at the Energy Frontier and on Tabletops*, Phys. Today, June (2003).